The Dissertation Committee for Zachary Adam Wilson
certifies that this is the approved version of the following dissertation:

Phase-field Modeling of Fracture for Multiphysics Problems

Committee:

Chad M. Landis, Supervisor

Thomas J.R. Hughes

Mark E. Mear

Krishnaswa Ravi-Chandar

John T. Foster

Phase-field Modeling of Fracture for Multiphysics Problems

by

Zachary Adam Wilson, B.S.E.S.

DISSERTATION

Presented to the Faculty of the Graduate School of

The University of Texas at Austin

in Partial Fulfillment

of the Requirements

for the Degree of

DOCTOR OF PHILOSOPHY

THE UNIVERSITY OF TEXAS AT AUSTIN

December 2016

Dedicated to Dad.

Acknowledgments

I wish to express my sincerest of gratitude to my advisor, Professor Chad Landis, for his devotion to my research and his mentorship of me as a young researcher. I consider myself exceedingly fortunate to have had the opportunity to be under the tutelage of such a fine person. Not only have I, under his guidance, evolved into a capable scientist, but I believe we have established a friendship that I will cherish for the rest of my life. I would argue that the single most important factor in defining a graduate student's experience is his advisor, and I could not ask for someone better.

The work that is presented in the following was conducted with the financial support of a grant from the Army Research Office (W911NF-10-1-0216) and the Statoil Fellows program at The University of Texas at Austin. I would also like to acknowledge the support of several scholarships and fellowships which were awarded to me during my studies: Eugene A. Ripperger Scholarship Fund in Engineering Mechanics, Alfred and Nellie King Graduate Fellowship, George J. Heuer, Jr. Ph.D. Endowed Graduate Fellowship Fund, University Preemptive Fellowship, Max L. Williams Endowed Graduate Fellowship in Mechanics of Solids, Structures, and Materials, and John and Mary Wheeler Endowed Graduate Fellowship in Engineering.

I would like to thank all of the members of my Ph.D. committee for

sacrificing their time and energy, and providing me with insightful comments which lead to the betterment of this document. I would also like to thank the remaining faculty of the Aerospace Engineering and Engineering Mechanics department for their consistent encouragement. Additionally, I'd like to thank the departmental staff for all of their help over the years, in particular, Tina Woods, Scott Messec, Lydia Tostado, Lorraine Sanchez, Therese Larson, and Caitlyn Collins.

I especially would like to recognize all of the fellow graduate students whose comradery I have cherished the last 6 years. These colleagues and friends have inspired me to be a better researcher, have encouraged me when times were tough, and have taught me how to truly appreciate a morning cup of coffee. I won't say every name, but a few of note are Scott Haltom, Dr. Nathan Bechle, Dr. Nikolaos Bouklas, Dr. Jerome Sicard, Dr. Micahel Borden, Dr. Dorinamaria Carka, Dr. Colin Heye, John Mersch, and Martin Scales. I am proud to say that many of the people I have met here will be life-long friends.

In many ways I am most grateful for my wife and family. Kelly's unwavering confidence and consistent support was foundational to my success. I thank her dearly for her patience and encouragement throughout this process. I have also received unconditional support from my parents and brothers. I am a product of wonderfully caring parents who installed in me the importance and power of education from a very young age.

Phase-field Modeling of Fracture for Multiphysics Problems

Publication No. _____

Zachary Adam Wilson, Ph.D.
The University of Texas at Austin, 2016

Supervisor: Chad M. Landis

Several recent works have demonstrated that phase-field methods for modeling fracture are capable of yielding complex crack evolution patterns in materials. This includes the nucleation, turning, branching, and merging of cracks subject to a variety of quasi-static and dynamic loadings. What follows will demonstrate how phase-field methods for fracture can be applied to problems involving materials subject to electromechanical coupling and the problem of hydraulic fracture. Brittle fracture is a major concern in piezoelectric ceramics. Fracture propagation in these materials is heavily influenced by the mechanical and electrical fields within the material as well as the boundary conditions on the crack surfaces. These conditions can lead to complex multimodal crack growth. We develop a continuum thermodynamics framework for a damaging medium with electromechanical coupling subject to four different

crack-face boundary conditions. A theory is presented to reproduce impermeable, permeable, conducting, and energetically consistent crack-face boundary conditions, the latter of which requires a finite deformation formulation. A primary application of hydraulic fracturing involves the injection of fluid into a perforated wellbore with the intention of fracturing the surrounding reservoir and stimulating its overall production. This process involves the coupling of fluid flow with material failure, which must account for the interactions of several cracks, both natural and man-made. Many of the questions on the effects these interactions have on the performance of the frac treatments are unanswered. We develop a continuum thermodynamics framework for fluid flow through a damaging porous medium in order to represent some of the processes and interactions that occur during hydraulic fracturing. The model will be capable of simulating both Stokes flow through cracks and Darcy flow through the porous medium. The flow is coupled to the deformation of the bulk solid medium and the evolution of cracks within the material. We utilize a finite deformation framework in order to capture the opening of the fractures, which can have substantial effects on fluid pressure response. For both models, a fully coupled non-linear finite element formulation is constructed. Several benchmark solutions are investigated to validate the expected behavior and accuracy of the method. In addition, a number of interesting problems are investigated in order to demonstrate the ability of the method to respond to various complexities like material anisotropy and the interaction of multiple cracks.

Table of Contents

List of Figures

Chapter 1

Introduction

The phase-field methodology has emerged as a powerful tool for modeling the evolution of microstructures and the interactions of defects in a wide range of materials and physical processes[1–5]. Phase-field methods can be implemented to simulate large-scale evolution of material microstructure and defect motion without the need to explicitly track interfaces or defects. In particular, phase-field methods for modeling fracture have been shown to be capable of yielding very complex crack patterns in three-dimensional solids[6–8]. The approach utilizes a continuous order parameter to characterize material degradation and crack propagation. Discrete crack surfaces are replaced by a smeared zone of damaged material and the evolution of the cracks is captured naturally by the solution of a system of differential equations. One strength of this modeling approach lies in the fact that there are no additional constitutive rules required within the theory that dictate when a crack should nucleate, grow, change direction, or split into multiple cracks. Cracks and their growth simply emerge as solutions to the governing partial differential equations of the model. A particularly unique and striking feature of the approach is that all calculations are performed entirely on the initial, undeformed configuration. There is no need to disconnect, eliminate, move elements, or

introduce additional discontinuous basis functions, as is commonly done in the discrete crack computational fracture mechanics approaches. This results in a significant simplification of the numerical implementation, and a simple and direct pathway from two-dimensional to three-dimensional applications. The primary objective of what follows is to extend the phase-field model of fracture to two problems that involve additional physics, specifically, the brittle fracture of piezoelectric ceramics and the hydraulically driven fracture of porous solids.

1.1 Fracture of Piezoelectric Ceramics

Over the past few decades there have been extensive investigations on fracture mechanics concepts for piezoelectric ceramics. There exists numerous works on the linear electroelastic fields near crack tips[9–24], the effects of crack face boundary conditions on crack tip fields and energy release rates[25–33], and on the effects of ferroelastic and ferroelectric switching on fracture toughness[34–37]. Modeling approaches that explicitly account for crack propagation have been developed to a lesser extent. Some notable contributions in this area have come from Arias et al.[38], Verhoosel et al.[39], and Linder et al.[40] on cohesive zone type approaches, and Abdollahi and Arias[41], Miehe et al.[42], and Xu et al.[43] on phase-field approaches to fracture.

In order for the phase-field model to properly represent brittle fracture in the purely mechanical case, assuming the absence of contact, the formulation must, and does, lead to traction-free crack surfaces. However, electrical

boundary conditions on the crack surfaces can vary depending on the medium inside the crack as well as on idealizations based upon model assumptions. The most common electrical boundary conditions, which are the ones discussed in this work, are permeable, impermeable, conducting, and energetically consistent. The main goal of Chapter 3 is to describe how these different electrical boundary conditions are implemented through the phase-field framework, and to describe how they affect fracture behaviors, in particular, crack propagation.

1.2 Hydraulic Fracture

The method of propagating fractures with hydraulically pressurized fluids is common in many engineering applications, particularly in the field of geology. Certainly the most notable of these is the stimulation of oil and gas wells, but other applications include waste disposal[44], in situ stress measurement[45], the stimulation of ground water wells[46,47], and geothermal reservoir development[48]. The advent of massive hydraulic fracturing and horizontal drilling in recent decades has made the extraction of oil and gas from unconventional reservoirs, particularly shale, economically viable. Additionally, heat extraction from subsurface geothermal systems has the potential to be a significant source of renewable carbon-free energy both world-wide and in the U.S.[49,50]. As such, the optimization of the many applications related to fluid driven fracturing is becoming increasingly important.

Conventional modeling approaches to hydraulically fractured systems have assumed symmetric, planar, bi-wing crack geometries. Analytical 2D

models were developed that made use of simplifying geometrical assumptions for fracture height and width in order to arrive at solutions in closed form. One such model, the Perkins-Kern-Nordgren (PKN) model, was formulated for fractures where the crack height is much smaller than crack length. The crack cross-section was assumed to be elliptical and to maintain a constant height along the length of the crack[51,52]. Another popular model, named after the work by Kristianovic, Geertsma, and de Klerk (KGD), was formulated for fractures where the crack height is much larger than crack length. In this case the crack cross section was assumed to have constant width[53,54]. The coupling of these simplifying geometrical assumptions with fluid mass conservation and the Poiseuille law for the fluid flow in the cracks yielded closed form solutions for the crack growth history. Both models have also been modified to include leak-off of the pressurized fluid into the surrounding porous rock. Later, planar three-dimensional and pseudo-three-dimensional computational models were developed that incorporate anisotropic fracture properties of the rock layers to predict more complex fracture height, length, and width growth profiles[55,56]. Several commercial production codes are based on these ideas and are in use today[56]. Additional studies, most notably by Detournay and co-workers[57–59], have revisited planar crack geometries, plane strain and penny shape cracks, and carefully investigated the crack tip behavior and propagation regimes of hydraulic fractures. These asymptotic analyses and analytical solutions provide valuable insights into some of the fundamental behaviors of fluid driven fractures and supply test cases for comparison with

numerical methods developed for more complex crack surface evolutions.

Recently research efforts have largely shifted towards the modeling of more complex fracture geometries. Microseismic mappings performed on hydraulically fractured wells have revealed that complex fracture growth is more prevalent than had been initially estimated and that such phenomena occur with increased frequency in unconventional reservoirs[60,61]. In particular, induced hydraulic fractures interact with pre-existing propped and natural fractures as well as other anisotropic features and inhomogeneities in the material[62,63]. Due to the low permeability of unconventional reservoirs, a proper understanding of fracture evolution is paramount to evaluating and ensuring the desired production of the well. Many of the same issues exist for enhanced geothermal reservoir development along with the additional complications associated with thermal effects and the generation of thermal cracks. Ultimately, the production of energy resources from these types of reservoirs can be improved with the development and utilization of high fidelity numerical tools that model the coupled fluid, thermal, and mechanical behaviors properly while allowing for complex crack growth topologies and interactions.

There exists several works on the numerical modeling of the fluid driven fracture process. Many of these approaches assume that the network of potential crack paths is known, e.g. a rectangular lattice of potential crack surfaces exists a priori, and the fluid loading then acts to open parts of said network as the fluid injection process proceeds[64–70]. The method developed in this work seeks to address cases where the crack path is not known a priori. Other

approaches for generic crack path evolution also exist, and each is thought to have certain strengths and weaknesses. Overall, the methods can be grouped into two types of approaches: (i) sharp interface methods where the cracks are represented explicitly and thus require constitutive rules for crack propagation and (ii) diffuse crack models where a significant challenge resides in representing physical behaviors within the cracks like the pressure and flow of fluids.

Of note for sharp interface methods are boundary element methods[71] and discrete crack representations within finite element methods[72–77]. Boundary element methods for determining the evolution of complex crack patterns have the advantage of being highly computationally efficient. Meshes are only needed on the boundaries of the domain and on the crack surfaces. Growth laws for the crack front are postulated relating the front velocity and direction to the local stress intensity factors. The disadvantages of the method are associated with difficulties for the incorporation of nonlinear or time dependent material responses in the bulk elastic material, and also in the handling of topological changes in the crack growth evolution like crack merging or branching. The discrete crack finite element methods usually implement numerical enrichment functions to allow cracks to grow through elements[75,78] or they relocate nodal positions such that cracks grow along element boundaries[76]. Both approaches also implement special element types at the crack front in order to capture the linear elastic near-tip K-fields for elastic problems. Such finite element methods will of course allow for nonlinear and time-dependent

behavior in the bulk material, although any nonlinear behavior affecting the crack tip fields may negate the utility of using the special crack tip elements and any crack growth laws based upon the stress intensities. While the topological changes associated with crack merging and branching can be addressed using level set methods and re-meshing, the necessity of additional constitutive rules for crack branching, direction selection, and nucleation remain.

Examples of diffuse crack approaches include peridynamics[79,80], gradient damage mechanics[81,82], and the phase-field methods presented herein and by other recent studies[6–8,83–92]. Peridynamics is a nonlocal theory in which material points interact with all other material points that reside within a nearby "horizon". As with the phase-field method, cracks are not tracked explicitly but rather emerge naturally from the model equations. Gradient damage mechanics approaches and phase-field fracture approaches are very similar with minor differences in the details of how localization occurs and the length scale over which damage is able to spread. All of these diffuse crack methods alleviate many of the issues related to the topological changes in crack path evolutions associated with branching, turning, merging, and nucleation. However, there are challenges associated with modeling the fluid flow through cracks and the interaction of pressurized fluids with crack faces.

1.3 Scope of Study

The dissertation is organized as follows. In Chapter 2 the phase-field approach to quasi-static brittle fracture is reviewed. A framework which uti-

lizes a micro-force balance law is developed, which acts as the foundation upon which the more complicated theories in the proceeding chapters are developed. Additionally, an analysis of the crack-tip behavior for various choices of the so-called degradation function of the strain energy is presented. Chapter 3 focuses on the implementation of the phase-field method of fracture for piezoelectric ceramics. The formulation developed is implemented within the context of linear piezoelectric constitutive relationships, where the material polarization is assumed to be frozen in the material. However, the general framework described herein may be extended to a wider variety of nonlinear constitutive behaviors. For example, the work of Abdollahi and Arias[41] describes a very similar implementation of several of the boundary conditions listed above. They also couple the phase-field fracture model with a phase-field model that captures structure evolution growth in ferroelectric solids. This work presents an alternative approach for the implementation of the electromechanical boundary conditions and adds a finite deformation theory for the energetically consistent conditions into the framework. Also, the problem of "anti-healing" with respect to the order parameter far from the crack surface is addressed by introducing a new degradation function. How this new function affects material response is discussed and compared to the standard formulation. The purpose of Chapter 4 is to enhance the phase-field/variational approach to fracture by coupling the physics of flow through porous media and cracks with the mechanics of fracture. The main modeling challenge addressed herein, which is a challenge for all diffuse crack representations, is on how to allow for the flow

of fluid and the action of fluid pressure on the aggregate within the diffuse damage zone of the cracks. There have been a few very recent studies which address the implementation of the phase-field method for fracture in poroelastic media[93–95]. The primary distinction in this work is in the presentation of the governing balance laws, and then the development of constitutive relationships through Coleman and Noll-type analysis procedures and, in particular, the handling of the fluid flow equations, which recover the Stokes equations for the fluid flow within cracks. Finally, in Chapter 5 the overall contributions of the work are summarized and new directions associated with the work are suggested. With each introduction of a new model and new physics there will be some overlapping of the discussion and development of the governing equations, in particular the phase-field equations. The motivation behind the repetition is that there is often switching of variables and the quantities they represent due to the multitude of physics introduced and the desire to use conventional variable representations where ever possible. Thus, Chapters 2, 3, and 4 are complete in terms of model development and the contents may be individually understood without thorough reading of the others. Throughout the presentation Einstein notation will be used and the usual convention of summation over repeated indices is implied.

Chapter 2

The Phase-field Model for Brittle Fracture

2.1 Introduction

In the following we review how Griffith's foundational theory for brittle fracture[14] is utilized in the variational approach to fracture. In particular, utilizing the approach developed by Gurtin et al.[96], it is shown that the phase-field approach to fracture can reproduce Griffith's theory with the simultaneous solution of micro-force and momentum balance laws. Next, various forms of the strain-energy degradation function are presented and analysed. A study of the resulting "crack tip" fields draws comparisons to cohesive zone models.

2.2 General Theory

2.2.1 Griffith's Theory of Brittle Fracture and the Variational Approach to Fracture

Consider an arbitrary volume of material V bounded by surface S containing a set of discrete cracks defined by the possibly discontinuous surface S_c. For a completely elastic material, Griffith's theory states that the total energy Φ of the volume would be the sum of the stored strain energy in V and the fracture surface energy of S_c minus the work done by the applied loads t_i

and b_i,

$$\Phi = \int_V \Omega(\varepsilon_{ij}) dV + \int_{S_c} G_c dS - \int_V b_i u_i dV - \int_S t_i u_i dS \quad , \tag{2.1}$$

where Ω is the elastic strain energy density in the material ε_{ij} is the small-strain tensor such that $\varepsilon_{ij} = \frac{1}{2}(u_{i,j}+u_{j,i})$ and , j represents differentiation with respect to the x_j direction. Small deformation assumptions will be used throughout the discussion. G_c represents the critical energy release rate or twice the fracture surface energy in Griffith's theory of brittle fracture. Note that here we are claiming that all fracture surfaces are traction free. To simplify the discussion, cracks will be allowed to heal. Then, Griffith's theory reduces to finding a kinematically admissible u_i and the configuration of crack surfaces S_c given V, S, t_i, b_i, and G_c such that Φ is minimized, or in the language of variational calculus,

$$\delta\Phi = 0 \quad . \tag{2.2}$$

If the configuration of resulting crack surfaces S_c is known a priori, then (2.2) may be solved and a growth criterion may be established, making up the foundation of much of the fracture mechanics literature that has developed over the last century. On the contrary, if S_c is unknown, then clearly, as the set of possible configurations of S_c will always be infinite, a solution to the above variational statement in its current form is cumbersome, if not hopeless. Following the formulation initially proposed by Francfort and Marigo[6] the fracture surface energy $\int_{S_c} G_c dS$ is approximated by a volume integration of

the phase-field parameter μ such that,

$$\int_{S_c} G_c dS \approx \int_V G_c \left[\frac{(1-\mu)^2}{4\ell_0} + \ell_0 \mu_{,i} \mu_{,i} \right] dV \equiv \int_V \psi^\mu dV \quad , \tag{2.3}$$

where ℓ_0 is a length-scale that governs the size of the region over which the phase-field transitions from 0 to 1 (which can be thought of as completely failed to entirely intact). This region will be referred to as the process zone. This approach is based on the variational approximation by elliptic functionals [97,98]. Now that the discrete traction free surfaces S_c have been removed, the strain energy must be modified such that regions contained in V where μ is near 0 cannot carry strain energy. Hence ψ^d is defined,

$$\psi^d(\varepsilon_{ij}, \mu) = f_d(\mu) \Omega(\varepsilon_{ij}) \quad , \tag{2.4}$$

where $f_d(\mu)$ is referred to as the degradation function and must, at a minimum, satisfy the following conditions [94,99],

$$f_d(0) = 0, \quad f_d(1) = 1, \quad f_d{}'(0) = 0 \quad . \tag{2.5}$$

The interpretation of the first two conditions is obvious, i.e. cracked material ($\mu = 0$) should have no stiffness and intact material ($\mu = 1$) should behave in the normal elastic fashion. The implication of the third condition will be discussed shortly. Making use of the divergence theorem, the variational

equation (2.2) now reduces to,

$$\begin{aligned} 0 \quad &= \int_V \left[\left(f_d(\mu) \frac{\partial \Omega}{\partial \varepsilon_{ij}} \right)_{,j} + b_i \right] \delta u_i dV \\ &+ \int_V \left[f_d{}'(\mu)\Omega - G_c \left(\frac{1}{2\ell_0}(1-\mu) + 2\ell_0 \mu_{,ii} \right) \right] \delta\mu dV \\ &+ \int_S \left(\left[f_d(\mu) \frac{\partial \Omega}{\partial \varepsilon_{ij}} n_j - t_i \right] \delta u_i + \left[2G_c \ell_0 \mu_{,i} n_i \right] \delta\mu \right) dS \end{aligned} \quad , \tag{2.6}$$

where n_i is the unit vector normal to the surface S. Noting that (2.6) holds for arbitrary combinations of δu_i and $\delta\mu$ we conclude the following,

$$\begin{aligned} \left(f_d(\mu) \frac{\partial \Omega}{\partial \varepsilon_{ij}} \right)_{,j} + b_i = 0 \quad &\text{in} \quad V \\ f_d{}'(\mu)\Omega - G_c \left(\frac{1}{2\ell_0}(1-\mu) + 2\ell_0 \mu_{,ii} \right) = 0 \quad &\text{in} \quad V \\ t_i = f_d(\mu) \frac{\partial \Omega}{\partial \varepsilon_{ij}} n_j \quad &\text{on} \quad S \\ \mu_{,i} n_i = 0 \quad &\text{on} \quad S \end{aligned} \quad . \tag{2.7}$$

Here the rationale behind the third requirement in (2.5) can be realized as the first derivative of f_d appears in the $\delta\mu$ volume equation. In fact, an additional requirement should be included, $f_d{}'(\mu) \geq 0$, such that an increase in strain energy, Ω, should only induce a decrease in μ. A decomposition of the strain energy Ω is often used to ensure that degradation only occurs as a result of tensile deformations. Such a decomposition will be utilized in Chapter 4 that is based on the work of Miehe et al.[89]. Requiring $f_d{}'(0) = 0$ ensures that $\mu > 0$ for any deformation and converges to $\mu = 0$ for a fully broken state, as negative values of μ would have no physical interpretation.

The defining feature of the phase-field approach to fracture, as elaborated in much detail by the work of Bourdin and others[7,100], is that in the

limit as the length scale ℓ_0 goes to zero, the solution of the variational equation (2.6) converges to that for the discrete fracture surface representation (2.1).

2.2.2 Casting the Phase-field Approach to Fracture as a Balance of Micro-forces

In contrast to defining a total energy and developing the governing equation through the use of variational principles, here we describe how the same equations can be derived through the analysis of fundamental continuum balance laws. Credit for the development of the approach that will be employed herein is owed to the work of Fried and Gurtin [101,102]. Again, a phase-field quantity μ is introduced to describe material degradation and represent crack surface energy. We need also to introduce a set of conjugate forces associated with changes in this quantity. To this end, we define λ as an external surface micro-force such that $\lambda\dot{\mu}$ is the power expended per unit area of surface by sources external to the volume under consideration, γ is an external body micro-force such that $\gamma\dot{\mu}$ is the power expended per unit volume by external sources, and π is an internal micro-force per unit volume such that $\pi\dot{\mu}$ is the power expended internally on the material per unit volume [96]. We also assume that on the surface there is a balance between the applied surface micro-force λ and an internal material micro-force vector ξ_i such that,

$$\lambda = \xi_j n_j \quad \text{on} \quad S \quad . \tag{2.8}$$

It is then also assumed that there exists a net balance of this set of micro-forces such that,

$$\int_S \lambda \, dS + \int_V \gamma \, dV + \int_V \pi \, dV = 0 \quad . \tag{2.9}$$

Application of the divergence theorem, (2.8), and the argument that the micro-force balance must hold for any arbitrary volume V yields the pointwise micro-force balance equation,

$$\xi_{i,i} + \gamma + \pi = 0 \quad . \tag{2.10}$$

Likewise, in the quasi-static setting, mechanical equilibrium can be stated as,

$$\int_S t_i dS + \int_V b_i dV = 0 \quad , \tag{2.11}$$

where b_i is the body force per unit volume and t_i is the traction vector. Equilibrium of a surface element yields a relationship between the traction and the Cauchy stress tensor,

$$t_i = \sigma_{ji} n_j \quad \text{on } S \quad , \tag{2.12}$$

where σ_{ij} is the symmetric Cauchy stress tensor. The Cauchy stress can be shown to be symmetric by an analysis of the balance of angular momentum. Using the divergence theorem and recognizing that the integral balance must hold for any arbitrary volume, we arrive at the differential form for the equation of equilibrium as,

$$\sigma_{ji,j} + b_i = 0 \quad \text{in } V \quad . \tag{2.13}$$

Next, the balance of energy under quasi-static conditions dictates that the total change to the internal energy of a closed the system is equivalent

to the external work and heat introduced to the system. Written in integral form,

$$\frac{d}{dt}\int_V e dV = \int_V \left(b_i \dot{u}_i + \gamma\dot{\mu} + r\right) dV + \int_S \left(t_i \dot{u}_i + \lambda\dot{\mu} - q_i n_i\right) dS \quad . \tag{2.14}$$

We have introduced r as the heat input per unit volume per unit time and q_i as the components of the heat flux vector. Invoking small strain and rotation assumptions and applying the above balance laws with the divergence theorem, the change in internal energy density is,

$$\dot{e} = \sigma_{ji}\dot{\varepsilon}_{ij} - \pi\dot{\mu} + \xi_i\dot{\mu}_{,i} + r - q_{i,i} \quad . \tag{2.15}$$

The Second Law of thermodynamics dictates that the internal entropy of the system must at least increase in the same amount as the entropy input to the system. The entropy input is defined as the heat input divided by the absolute temperature θ and the Second Law can be written as,

$$\frac{d}{dt}\int_V s dV \geq \int_V \frac{r}{\theta} dV - \int_S \frac{q_i n_i}{\theta} dS \quad , \tag{2.16}$$

which, subject to the previously mentioned assumptions, can be reduced to,

$$\theta\dot{s} \geq r - q_{i,i} + \frac{1}{\theta} q_i \theta_{,i} \quad . \tag{2.17}$$

The Hemholtz free-energy density is defined as $\psi = e - s\theta$. Under the principle of equi-presence the Hemholtz free energy density ψ, as well as σ_{ji}, π, ξ_i, s, and q_i are allowed to depend freely on ε_{ij}, μ, $\mu_{,i}$, $\dot{\mu}$, θ, and $\theta_{,i}$. Additional dependencies can be shown to vanish. Then, (2.17) becomes,

$$\frac{\partial\psi}{\partial\varepsilon_{ij}}\dot{\varepsilon}_{ij} + \frac{\partial\psi}{\partial\mu}\dot{\mu} + \frac{\partial\psi}{\partial\mu_{,i}}\dot{\mu}_{,i} + \frac{\partial\psi}{\partial\dot{\mu}}\ddot{\mu} + \frac{\partial\psi}{\partial\theta}\dot{\theta} + \frac{\partial\psi}{\partial\theta_{,i}}\dot{\theta}_{,i} \leq \sigma_{ji}\dot{\varepsilon}_{ij} - \pi\dot{\mu} + \xi_i\dot{\mu}_{,i} + s\dot{\theta} - \frac{1}{\theta} q_i \theta_{,i} \quad . \tag{2.18}$$

Following the procedures developed by Coleman and Noll[103], given that this expression is linear in $\dot{\varepsilon}_{ij}$, $\dot{\mu}_{,i}$, $\ddot{\mu}$, and $\dot{\theta}$, the inequality will hold for arbitrary time histories of the parameter set if,

$$\frac{\partial \psi}{\partial \varepsilon_{ij}} = \sigma_{ji}, \quad \frac{\partial \psi}{\partial \mu_{,i}} = \xi_i, \quad \frac{\partial \psi}{\partial \dot{\mu}} = 0, \quad \frac{\partial \psi}{\partial \theta_{,i}} = 0, \quad \text{and} \quad \frac{\partial \psi}{\partial \theta} = -s \quad . \tag{2.19}$$

The remaining terms result in the simplified dissipation inequality,

$$\left(\pi + \frac{\partial \psi}{\partial \mu}\right)\dot{\mu} + \frac{1}{\theta} q_i \theta_{,i} \leq 0 \quad . \tag{2.20}$$

Here we decide to be slightly over restrictive and recognize that (2.20) can be satisfied by setting the internal micro-force π and heat flux q_i to,

$$\begin{aligned} \pi &= -\frac{\partial \psi}{\partial \mu} - \beta \dot{\mu} \\ q_i &= -\kappa_{ij} \theta_{,j} \end{aligned} \quad , \tag{2.21}$$

with $\beta \geq 0$ and κ_{ij}, the material thermal conductivity, positive definite. Each are allowed to depend on all the relevant parameters discussed above. More generally we would include cross terms involving $\dot{\mu}$ and $\theta_{,i}$. The micro-force balance law of (2.10) becomes, in terms of μ,

$$\left(\frac{\partial \psi}{\partial \mu_{,i}}\right)_{,i} - \frac{\partial \psi}{\partial \mu} + \gamma = \beta \dot{\mu} \quad \text{in } V \quad . \tag{2.22}$$

We now complete the comparison by defining the Hemholtz free energy density explicitly as,

$$\psi = f_d(\mu)\Omega(\varepsilon_{ij}) + G_c \left[\frac{(1-\mu)^2}{4\ell_0} + \ell_0 \mu_{,i} \mu_{,i}\right] \quad . \tag{2.23}$$

Thus, if β and λ are taken to vanish then application of (2.23) with (2.8), (2.13), (2.12), and (2.13) yields identical equations to those described by (2.7).

However, a framework has been constructed upon which more complex theories can be developed.

2.3 Analysis and Discussion

2.3.1 Degradation Function

To this point, the degradation function f_d has been left to remain general beyond the satisfaction of (2.5). The majority of the literature has adopted the originally proposed quadratic form[6],

$$f_d^q(\mu) = \mu^2 \quad . \tag{2.24}$$

This form has the advantage that it is especially simple to implement in a so called "staggered" scheme, (i.e. when u_i is solved for fixed μ, then μ is solved for fixed u_i, and this is alternated until a certain degree of convergence is achieved) since both governing equations are rendered linear. An alternative form, originally proposed by Borden[99] and will be referred to as the cubic form, is,

$$f_d^c(\mu) = \mu^2 \left[s\left(\mu - 1\right) - 2\mu + 3 \right] \quad , \tag{2.25}$$

where s is the slope at $\mu = 1$. For $s \geq 0$, $s \ll 1$, this form has some very beneficial features for solving linear elastic brittle fracture problems ($\Omega = \frac{1}{2} c_{ijkl} \varepsilon_{ij} \varepsilon_{kl}$). These features can be most readily demonstrated by an analysis of homogeneous material response (i.e. $\mu_{,i} = 0$). If uniaxial loading conditions are adopted and external body forces and micro-forces are taken to be zero then the equations (2.13) and (2.22) can be solved to give evolutions of stress

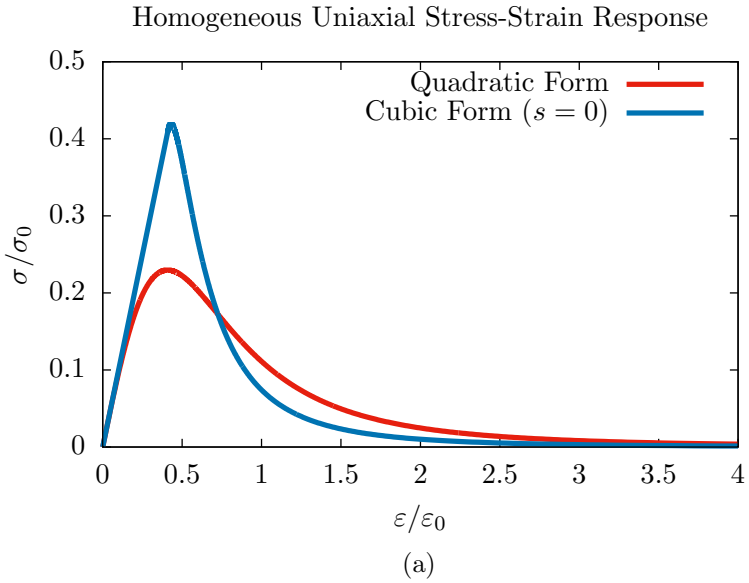

(a)

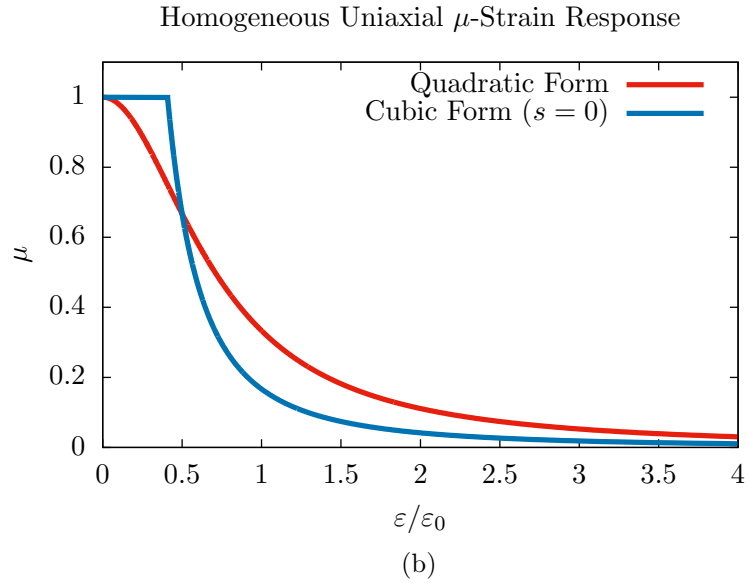

(b)

Figure 2.1: Homogeneous uniaxial material response. Strain is normalized by $\varepsilon_0 = \sqrt{G_c/E\ell_0}$ and stress is normalized by $\sigma_0 = \sqrt{G_c E/\ell_0}$. The cubic form of the degradation function f_d results in both a more linear initial stress-strain response and a higher rate of residual stress decay for large strain.

and μ as functions of applied strain. The results are summarized in Figure 2.1. The first positive feature is that the cubic degradation function results in a stress-strain response that is exactly linear nearly up until the strain value associated with the critical peak stress (there is a small region of increasing stress after the large region of initial linear response). This is a consequence of the fact that $f_d'(1) = 0$ when $s = 0$ and no degradation occurs (i.e. $\mu = 1$) up until a critical strain threshold that corresponds to $\varepsilon/\varepsilon_0 = \sqrt{1/6}$, where $\varepsilon_0 = \sqrt{G_c/E\ell_0}$. This is in contrast with the quadratic form which experiences non-linear stress-strain behavior at the very onset of straining. The second desirable feature of the cubic degradation function is that the stress decays at a slightly higher rate for large strain than that for the quadratic form. In fact, the cubic form decays like $\frac{1}{12}\left(\frac{\varepsilon_0}{\varepsilon}\right)^3$ as compared to $\frac{1}{4}\left(\frac{\varepsilon_0}{\varepsilon}\right)^3$ for the quadratic form. Another feature of the cubic form is that it results in a larger realized maximum stress value than that for the quadratic case. The peak stress value for the cubic case is $\sigma_c = \left(\frac{27}{50}\sqrt{\frac{3}{5}}\right)\sigma_0$ as opposed to $\sigma_c = \left(\frac{9}{16}\sqrt{\frac{1}{6}}\right)\sigma_0$ for the quadratic case, where $\sigma_0 = \sqrt{G_c E/\ell_0}$. These uniaxial peak stress values serve as good estimates for material tensile strength. Note that if the parameter s is chosen to be 0 then the model will not be capable of capturing crack nucleation and so, for practical purposes, s is chosen to be positive but very close to 0. Alternative forms of the degradation function are introduced in Chapter 3 which have characteristics that are similar to the cubic form but have additional features that are beneficial for modeling piezoelectricity.

2.3.2 Mesh Dependency of the Fracture Surface Energy

Another useful analytical solution of the phase-field equations is the resulting μ profile for a fully cracked one dimensional bar. If the length of the bar is chosen to be long compared to ℓ_0 then approximate boundary conditions can be chosen as $\mu_{,1} = 0$ at $x = \pm\infty$. Forcing also that $\mu = 0$ at $x = 0$ then (2.22) with $\beta, \gamma = 0$ leads to,

$$\mu(x) = 1 - e^{-\left|\frac{x}{2\ell_0}\right|} \quad . \tag{2.26}$$

Evaluation of (2.3) with (2.26) for an infinitely long bar and normalizing by bar cross-sectional area identically gives G_c[6,7]. In fact, evaluation of (2.3) with (2.26) from $x = -10\ell_0$ to $x = 10\ell_0$ gives $0.99996G_c$. This analytical result corresponds to a jump discontinuity in displacement u_x at $x = 0$. However, the phase-field method for fracture is typically implemented in the context of (at least) C^0 finite elements[8,84] and displacements are discretized by a continuous field. Thus, the jump in displacement occurs over some finite length scale h^e associated with the element size where the crack exists (or where μ is close to zero). For piece-wise linear finite element spaces h^e is precisely the element height. For large enough displacements (i.e. when the residual crack stresses have sufficiently decayed) the phase-field μ takes on the limit form of,

$$\mu(x) = \begin{cases} 1 - e^{\left(\frac{x+h^e/2}{2\ell_0}\right)} & , \quad x < -\dfrac{h^e}{2} \\ 0 & , \quad -\dfrac{h^e}{2} \leq x \leq \dfrac{h^e}{2} \\ 1 - e^{-\left(\frac{x-h^e/2}{2\ell_0}\right)} & , \quad x > \dfrac{h^e}{2} \end{cases} \quad . \tag{2.27}$$

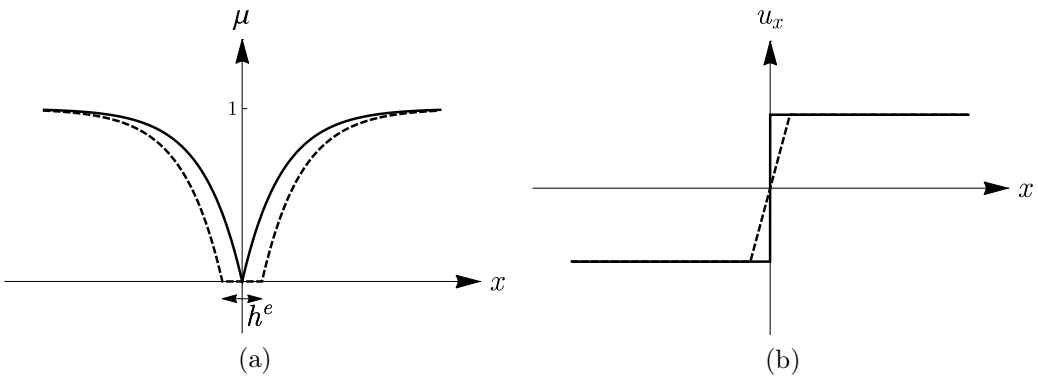

Figure 2.2: These plots illustrate the difference between the analytical and discretized representations of the phase-field crack "surface". (a) shows the phase-field profile for the analytical case (solid line) and discretized case (dotted line). (b) shows the crack opening displacement as a function of location in the for the analytical and discretized cases respectively. h^e is a characteristic length scale associated with the discretization (i.e. element size). These results are specific to a piece-wise linear discretization, however, similar features are present for any continuous representation of the displacement field.

The results are illustrated in Figure 2.2. Now, evaluation of (2.3) with (2.27) for an infinitely long bar and again normalizing by bar cross-sectional area gives $G_c\left(1+\frac{h^e}{4\ell_0}\right)$ which corresponds to the fracture toughness adjustment factor suggested by Bourdin[84]. In other words, the G_c implemented in the numerical model should obey,

$$G_c = \frac{G_c^{actual}}{\left(1+\frac{h^e}{4\ell_0}\right)} \quad , \tag{2.28}$$

in order to achieve optimal accuracy.

2.3.3 The Phase-Field Model Crack-tip Fields and Comparison to Cohesive Fracture Zone Models

For materials that meet certain geometric requirements there exists a region surrounding the crack tip where the asymptotic K-fields dominate the displacement and stress fields in the material. This is the small-scale yielding condition. This region is commonly referred to as the K-annulus and surrounds a zone at the crack tip where non-linear material responses are present and is itself surrounded by a region where higher-order terms are relevant as the effect of specimen boundaries becomes significant. This idea is illustrated in Figure 2.3. For quasi-static (or slow) mode-I loadings under small-scale yielding Irwin developed the relationship between energy release rate G and mode-I stress intensity factor K_I for isotropic plane-strain conditions such that,

$$K_I = \sqrt{\frac{G\,E}{(1-\nu^2)}} \quad , \tag{2.29}$$

and suggested that a crack will propagate when the stress intensity factor $K_I = K_{Ic}$, or equivalently $G = G_c$, regardless of the specifics of the non-linearity[104]. Similar relationship may be found for mode-II and mode-III.

In order to characterize the non-linear response of the phase-field model at the crack tip a finite-element mesh was constructed to be sufficiently large $(2000\ell_0 \times 2000\ell_0)$ such that it can be argued to be far away from the non-linear processes at the tip. The following symmetric weak form of the phase-field equations was implemented within the finite-element method:

Find $u_i \in \mathcal{S}_i^u$ and $\mu \in \mathcal{S}^\mu$ such that for all $\delta u_i \in \mathcal{V}_i^u$ and $\delta\mu \in \mathcal{V}^\mu$,

$$\int_V \left(\sigma_{ji}\delta\varepsilon_{ij} - \pi\delta\mu + \xi_i\delta\mu_{,i}\right) dV = \int_S t_i\delta u_i dS \quad . \tag{2.30}$$

The previously derived Hemholtz free energy (2.23) along with constitutive relations (2.19) and (2.21) are used where Ω is taken such that $\Omega = \frac{1}{2}c_{ijkl}\varepsilon_{ij}\varepsilon_{kl}$ and c_{ijkl} is the typical isotropic compliance tensor. Here the body force b_i, external micro-body force γ, external micro-surface force λ, and dissipation constant β are taken to be zero. Dirichlet displacement boundary conditions associated with the asymptotic mode-I K-field displacements are applied to the boundary of the finite-element mesh,

$$\begin{aligned} u_x(x,y) &= \frac{K_{Ic}}{2E}\sqrt{\frac{r(x,y)}{2\pi}}\,(1+\nu)\left[3-4\nu-\cos\left(\theta(x,y)\right)\right]\cos\left(\frac{\theta(x,y)}{2}\right) \\ u_y(x,y) &= \frac{K_{Ic}}{2E}\sqrt{\frac{r(x,y)}{2\pi}}\,(1+\nu)\left[3-4\nu-\cos\left(\theta(x,y)\right)\right]\sin\left(\frac{\theta(x,y)}{2}\right) \end{aligned} \quad . \tag{2.31}$$

The value used for K_{Ic} is,

$$K_{Ic} = \sqrt{\frac{G_c\left(1+\frac{h^e}{4\ell_0}\right)E}{(1-\nu^2)}} \quad , \tag{2.32}$$

which corresponds to the adjustment factor (2.28). The displacement and virtual displacement fields u_i and δu_i as well as the phase-field and virtual phase-field parameters μ and $\delta\mu$ are discretized using piece-wise bi-linear quadrilateral elements. A graded, structured mesh was generated such that an element size of $h^e = \ell_0/10$ existed in regions where degradation was expected. In fact, sufficient resolution of field gradients only requires a uniform mesh near the

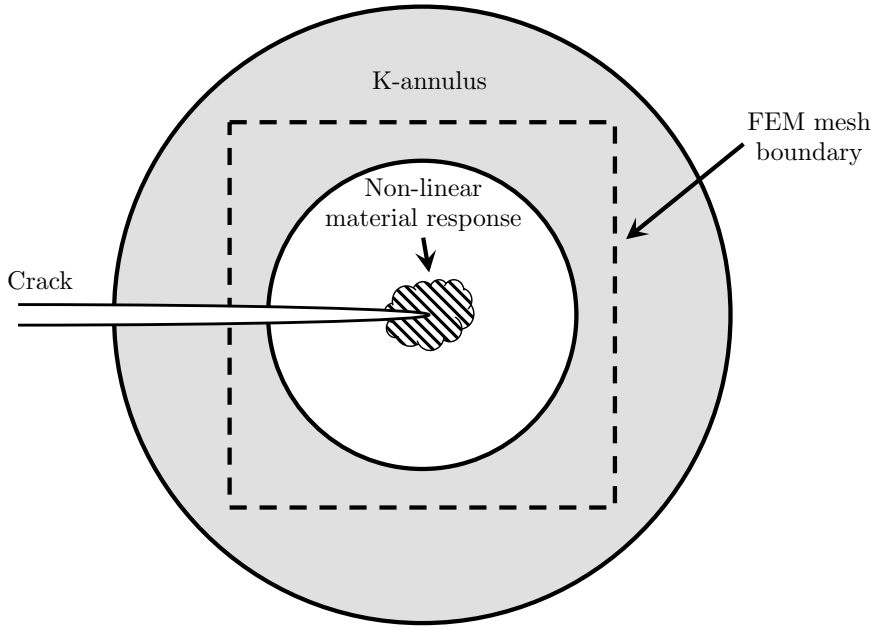

Figure 2.3: This picture illustrates the K-annulus idea. If the specimen dimensions and crack length is sufficiently large compared to the length scale associated with non-linear material than there exists a region surrounding the crack tip where the asymptotic K-fields for the displacements and stresses are dominant. Inside this region is the non-linear material response associated with the failure mechanism and outside terms influenced by specimen boundaries are significant. The finite-element boundary is contained within the K-annulus such that the crack tip behavior of the phase-field model can be analyzed.

tip of cracks, or at the origin of the specimen, and long slender elements can be used to resolve the phase-field behind the crack tip.

A hybrid coupled Newton-Raphson scheme was used to obtain converged numerical solutions. This scheme takes advantage of the stability of the staggered approach where each field (u_i and μ) is solved for individually while the other field is held fixed and the procedure is alternated. At the completion of a fixed number of staggered iterations, a Newton-Raphson method for the fully coupled problem is solved such that both fields are computed simultaneously using the full tangent stiffness matrix of the residual (2.30). In some sense, the staggered scheme provides a "good-enough" initial guess so that the fully coupled scheme is able to achieve convergence. The hybrid scheme is by no means infallible and application of the scheme requires a degree of trial and error in determining a balance between the fixed number of staggered iterations and magnitude of overall load increments. The number of staggered iterations can be alternatively based on the size of a norm of the residual or field updates or both. If successful, the hybrid scheme provides solutions where convergence of the residual is guaranteed. In the following analysis, both the quadratic and cubic forms of the degradation function were used for purposes of comparison.

Figure 2.4 shows the resulting phase-field fracture fields. The images are centered at the origin of the specimen. Note that no phase-field nodal degrees of freedom are specified a priori but, instead, evolve naturally in response to the applied K-field displacements at the boundary. The existence of the significant

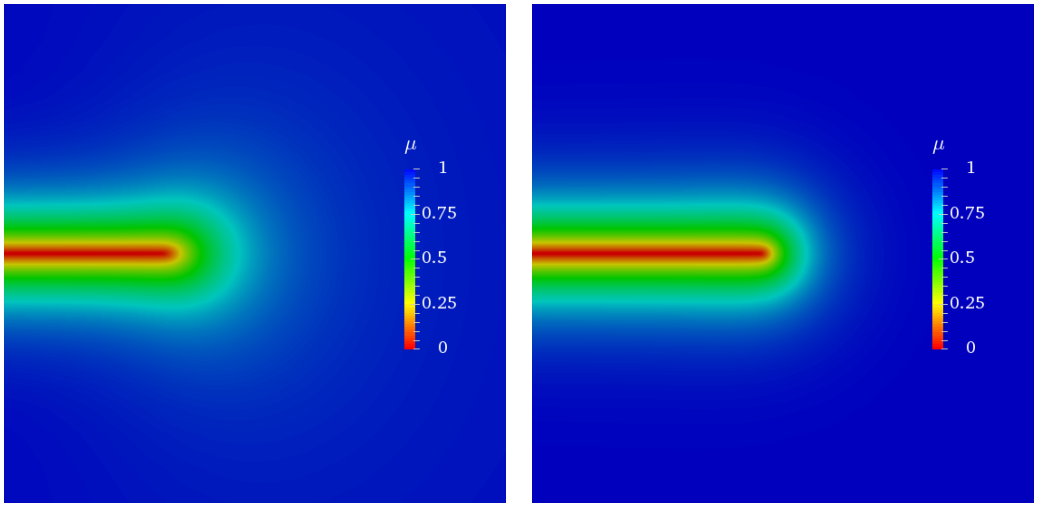

(a) (b)

Figure 2.4: The resulting phase-fields for the K-field problem near the origin. The actual domain size is $2000\ell_0 \times 2000\ell_0$ and the pictured size is $30\ell_0 \times 30\ell_0$. (a) Quadratic form of the degradation function f_d, (b) Cubic form of the degradation function f_d.

non-linear response for the quadratic form of the degradation function leads to a "bulbing" type behavior of the phase-field at the tip. This increases the total surface energy of the crack and, as expected, the "tip" falls short of the origin. The cubic form does not exhibit this behavior.

Figure 2.5 shows plots of the stresses and displacements and compares them to the asymptotic linear elastic K-field solution and the Dugdale-Barenblatt cohesive zone model[105,106], which assumes a constant traction separation relationship (shown in Figure 2.5a). The separation traction for the Dugdale-Barenblatt model is set to the maximum observed σ_{yy} ahead of the crack tip for the phase-field model for each degradation function. These values correspond closely to the uniaxial peak stress values derived in Section 2.3.1 where,

$$\begin{aligned} \sigma_{yy}^{\max} &= 1.105\sigma_c \quad \text{(quadratic)} \\ \sigma_{yy}^{\max} &= 1.002\sigma_c \quad \text{(cubic)} \end{aligned} \quad . \tag{2.33}$$

The size R_p of the cohesive zone is determined from the critical energy release rate G_c and the separation traction such that,

$$R_p = \frac{\pi}{8}\left(\frac{K_{Ic}}{\sigma_{yy}^{\max}}\right)^2 \Rightarrow \begin{aligned} R_p^q &= 6.67\ell_0 \quad \text{quadratic} \\ R_p^c &= 2.57\ell_0 \quad \text{cubic} \end{aligned} \quad . \tag{2.34}$$

There is some ambiguity in choosing the origin for the Dugdale-Barenblatt model. A simple equilibrium analysis developed by Irwin on the asymptotic K-field suggests that a reasonable approach is to place the origin at the center of the process zone, $R_p/2$. Figure 2.6 shows a comparison of the observed phase-field for the K-field problem with the analytical phase-field profile (2.26) shifted

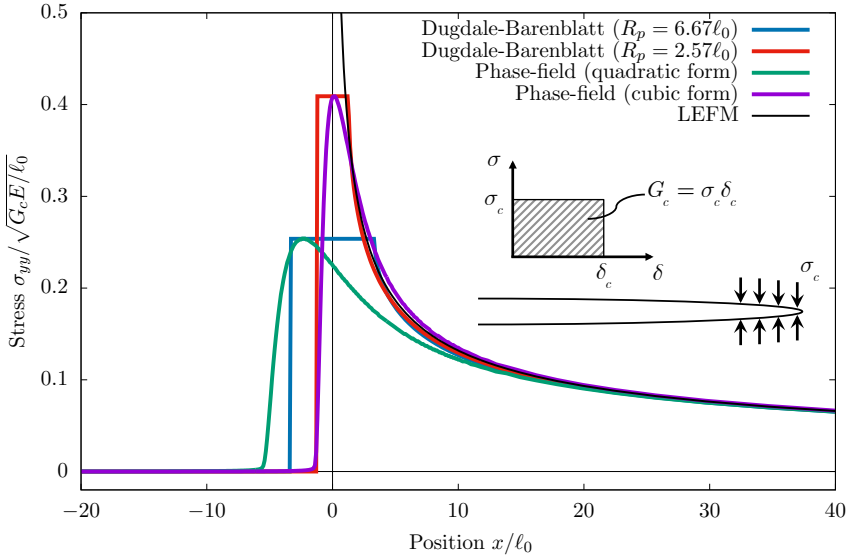

(a)

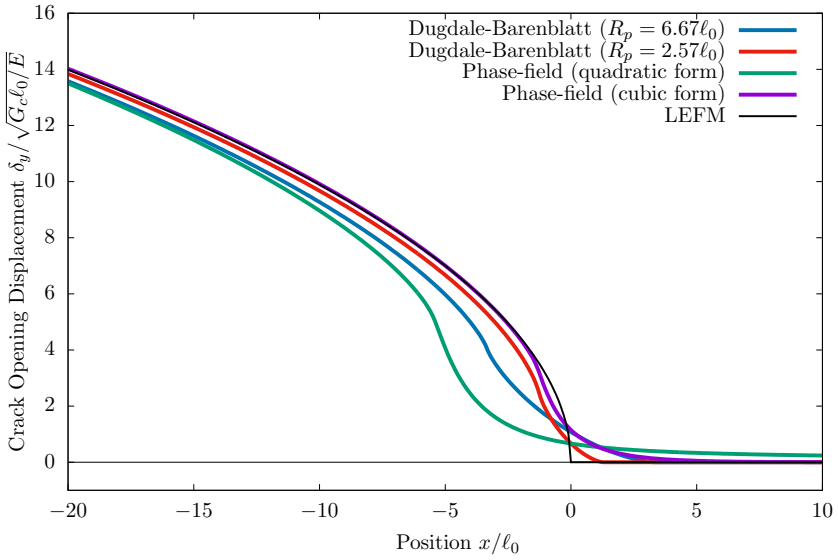

(b)

Figure 2.5: Plots of (a) stress and (b) crack opening displacement for the K-field boundary value problem for the quadratic and cubic degradation functions. Values associated with perfectly linear elastic fracture mechanics and the Dugdale-Barenblatt cohesive zone model are included for comparison purposes. The phase-field crack opening displacements are calculated using (2.35). Figures describing the Dugdale-Barenblatt model are included on the stress plot.

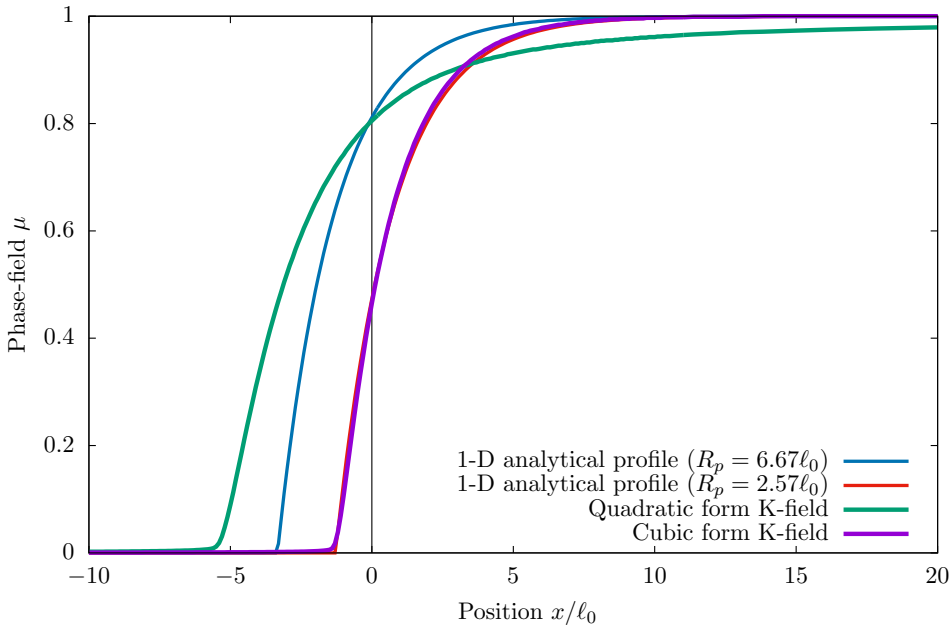

Figure 2.6: Plots comparing the observed phase-field values for the K-field asymptotic loading with the analytical result (2.26) along the x-axis. The analytical result is shifted to start from the middle of the estimated Dugdale-Barenblatt process zone size (2.34). The profile is significantly perturbed by the presence of straining around the crack tip for the quadratic degradation function.

to the centers of the estimated Dugdale-Barenblatt process zones according to (2.34). Here the early onset of degradation for the quadratic form of the degradation function can be clearly seen. In contrast, the analytical profile is nearly identical to the observed profile for the cubic degradation function.

Unlike the Dugdale-Barenblatt cohesive zone model, where the traction separation behavior is confined to a line directly in front of the crack tip, the non-linear process associated with crack opening for the phase-field occurs over

the length scale ℓ_0 in the direction orthogonal to the crack. The phase-field crack opening displacements shown in Figure 2.5b are generated using what is referred to by Bourdin and others[93] as a Γ-convergence construction such that,

$$\delta_y = \int_{-\infty}^{\infty} u_y(x,y)\mu_{,y}(x,y)dy \quad , \tag{2.35}$$

is evaluated for points along the crack. This integral can be thought of as the phase-field approximation of the displacement jump discontinuity,

$$u_y n_y|_{y=0^-}^{y=0^+} = u_y^+ - u_y^- = \delta_y \quad . \tag{2.36}$$

While the comparison to the Dugdale-Barenblatt model is imperfect for several reasons, the results shown in Figure 2.5 suggest that the phase-field approach to brittle fracture can be viewed as having similar features and functionality to that of cohesive zone fracture models. Due to the higher peak stress and larger degree of linearity in the stress response, the cubic degradation function performs significantly better in approximating brittle fracture and in reproducing the expected cohesive zone behaviors. The delayed onset of degradation for the cubic form has also been shown to improve results for cases where usage of the quadratic form has lead to nucleation of degradation at the application of load or in other regions of material where cracks are not expected to form.

The preceding analysis is not intended to be comprehensive, as the results shown are dependent not only on the specific form of the degradation function, but also on the choice of the surface energy functional (2.3). While

the form chosen in this analysis is certainly the most common form used in the literature, several alternative forms have been purposed and each have their own merits[107,108]. Instead, the intention of the analysis is to shed light on features of the variational approach to fracture that are often overlooked in much of the literature.

Chapter 3

A Phase-field Model for Fracture in Piezoelectric Ceramics[1]

3.1 Introduction

In the following, the governing equations are derived, including reintroducing those governing the phase-field, from integral balance laws. We then use thermodynamic arguments to develop general constitutive relationships between all system variables. Section 3.2.2 describes, in a general form, how the permeable, impermeable, and conducting boundary conditions are implemented. Section 3.2.3 then develops the finite deformation framework required for the implementation of energetically consistent boundary conditions. The degradation function and its affects on the model material behavior are examined here. Section 3.3 provides a short discussion as to how the formulation is implemented numerically with the finite element method and addresses a small nuance in implementation of the conducting boundary conditions. Section 3.4 details three specific numerical simulations, the first provides model verification, the second describes the affect of each boundary condition on

[1]Based on the journal publication: Wilson, Zachary A., Borden, Michael J., and Landis, Chad M., A phase-field model for fracture in piezoelectric ceramics, International Journal of Fracture, Volume 183(2), 2013, Pages 135-153, ISSN 1573-2673, http://dx.doi.org/10.1007/s10704-013-9881-9.

crack propagation, and the last illustrates a potential advantage of modeling fracture in piezoelectric ceramics using the phase-field approach. Finally, some concluding remarks are presented and the limitations and strengths of the phase-field approach are considered.

3.2 General Theory

In this section, the equations governing a small deformation, mechanically and electrically quasi-static, isothermal, electromechanical boundary value problem will be reviewed.

Consider a volume of material, V, bounded by the surface, S. The total force balance is written as

$$\int_S t_i dS + \int_V b_i dV = 0 \tag{3.1}$$

where b_i is the body force per unit volume and t_i is the traction vector. Equilibrium of a surface element yields a relationship between the traction and the Cauchy stress tensor,

$$t_i = \sigma_{ji} n_j \quad \text{on } S \tag{3.2}$$

where σ_{ij} is the symmetric Cauchy stress tensor and n_i is a unit vector normal to the surface S directed outward from the volume. The Cauchy stress is symmetric due to the balance of angular momentum. Using the divergence theorem and recognizing that the integral balance must hold for any arbitrary volume, we arrive at the differential form for the equation of equilibrium as,

$$\sigma_{ji,j} + b_i = 0 \quad \text{in } V. \tag{3.3}$$

Again, the infinitesimal strain-displacement compatibility conditions are

$$\varepsilon_{ij} = \frac{1}{2}\left(u_{i,j} + u_{j,i}\right) \tag{3.4}$$

where ε_{ij} is the infinitesimal strain tensor and u_i is the displacement vector.

A total charge balance can be written as

$$\int_S \omega dS + \int_V q dV = 0 \tag{3.5}$$

where q is the free charge per unit volume in V and ω is the free charge per unit area (note that when the domain is finite ω must also account for the effective charge due to material and free-space outside of V) residing on S. Applying Gauss's Law to a surface element, we arrive at a relationship between electric displacement, D_i, and the surface charge per unit area,

$$D_i n_i = -\omega \quad \text{on } S. \tag{3.6}$$

Then, using the divergence theorem, the differential form of Gauss's Law appears as

$$D_{i,i} = q \quad \text{in } V. \tag{3.7}$$

Finally, under quasi-static conditions Maxwell's laws dictate that the electric field, E_i, can be written as the gradient of a potential, ϕ, such that

$$E_i = -\phi_{,i}. \tag{3.8}$$

A phase-field or order parameter μ is introduced which describes material degradation such that when $\mu = 1$ the material can be considered entirely

intact and when $\mu = 0$ the material can be considered to be completely failed. Following the original work of[96], a set of external surface (λ) and volume (γ) micro-forces are then introduced that exert power during changes of the phase-field parameter. A set of internal micro-forces (π and ξ_i) are introduced to balance the external micro-forces such that they satisfy balance laws of the form

$$\int_S \lambda dS + \int_V (\gamma + \pi)\, dV = 0 \tag{3.9}$$

and

$$\xi_i n_i = \lambda. \tag{3.10}$$

By the divergence theorem and arbitrary volume arguments, we find

$$\int_V (\xi_{i,i} + \gamma + \pi)\, dV = 0 \quad \Rightarrow \quad \xi_{i,i} + \gamma + \pi = 0 \quad \text{in } V. \tag{3.11}$$

Next, the isothermal form of the Second Law of thermodynamics dictates that the total change to the Helmholtz free energy, ψ, of a closed system cannot exceed the work done on the system. Written in integral form,

$$\int_V \dot{\psi} dV \leq \int_V (b_i \dot{u}_i + \phi \dot{q} + \gamma \dot{\mu})\, dV + \int_S (t_i \dot{u}_i + \phi \dot{\omega} + \lambda \dot{\mu})\, dS \tag{3.12}$$

We allow the ψ, ξ_i, σ_{ij}, E_i, and π to depend on ε_{ij}, D_i, μ, $\mu_{,i}$, and $\dot{\mu}$ and the second law inequality becomes,

$$\begin{aligned} \frac{\partial \psi}{\partial \varepsilon_{ij}} \dot{\varepsilon}_{ij} + \frac{\partial \psi}{\partial D_i} \dot{D}_i + \frac{\partial \psi}{\partial \mu} \dot{\mu} + \frac{\partial \psi}{\partial \mu_{,i}} \dot{\mu}_{,i} + \frac{\partial \psi}{\partial \dot{\mu}} \ddot{\mu} \leq \\ \sigma_{ji} \dot{\varepsilon}_{ij} + E_i \dot{D}_i + \xi_i \dot{\mu}_{,i} - \pi \dot{\mu}. \end{aligned} \tag{3.13}$$

Given that this expression is linear in $\dot{\varepsilon}_{ij}$, $\dot{D}_i$, $\dot{\mu}_{,i}$, and $\ddot{\mu}$, the inequality will hold for arbitrary time histories of the parameter set if,

$$\frac{\partial \psi}{\partial \varepsilon_{ij}} = \sigma_{ji}, \quad \frac{\partial \psi}{\partial D_i} = E_i, \quad \frac{\partial \psi}{\partial \mu_{,i}} = \xi_i, \quad \text{and} \quad \frac{\partial \psi}{\partial \dot{\mu}} = 0. \tag{3.14}$$

The remaining terms result in the simplified dissipation inequality,

$$\left(\pi + \frac{\partial \psi}{\partial \mu}\right) \dot{\mu} \leq 0. \tag{3.15}$$

This inequality is satisfied by setting the internal micro-force π as,

$$\pi = -\frac{\partial \psi}{\partial \mu} - \beta \dot{\mu}, \tag{3.16}$$

with $\beta \geq 0$ allowing β to depend on all the relevant parameters discussed above. Thus, the micro-force balance law of (3.11) becomes, in terms of μ,

$$\left(\frac{\partial \psi}{\partial \mu_{,i}}\right)_{,i} - \frac{\partial \psi}{\partial \mu} + \gamma = \beta \dot{\mu} \quad \text{in } V. \tag{3.17}$$

A similar Second Law analysis can be preformed on the electrical enthalpy based on the Legendre transformation

$$h = \psi - E_i D_i \tag{3.18}$$

which results in

$$\begin{aligned} &\int_V \left(\dot{h} + E_i \dot{D}_i + \dot{E}_i D_i\right) dV \leq \\ &\int_V \left(b_i \dot{u}_i + \phi \dot{q} + \gamma \dot{\mu}\right) dV + \int_S \left(t_i u_i + \phi \dot{\omega} + \lambda \dot{\mu}\right) dS \end{aligned} \tag{3.19}$$

The chain-rule and divergence theorem lead to

$$\begin{aligned} \frac{\partial h}{\partial \varepsilon_{ij}} \dot{\varepsilon}_{ij} + \frac{\partial h}{\partial E_i} \dot{E}_i + \frac{\partial h}{\partial \mu} \dot{\mu} + \frac{\partial h}{\partial \mu_{,i}} \dot{\mu}_{,i} + \frac{\partial h}{\partial \dot{\mu}} \ddot{\mu} \leq \\ \sigma_{ji} \dot{\varepsilon}_{ij} - D_i \dot{E}_i + \xi_i \dot{\mu}_{,i} - \pi \dot{\mu} \end{aligned} \tag{3.20}$$

and again by the same arguments used above,

$$\frac{\partial h}{\partial E_i} = -D_i \tag{3.21}$$

with all other equations of (3.14) and (3.15) remaining the same and noting that ψ should be replaced by h and partial derivatives with respect to the other independent variables hold E instead of D fixed. In summary, the preceding Second Law analysis reveals constitutive relationships between stress, deformation, electric displacement, electric field, and the phase-field parameter that are derived from a single Helmholtz free energy density or electrical enthalpy density function.

3.2.1 Phase-Field Fracture Formulation

Again, we introduce the phase-field approach to fracture. For a brittle piezoelectric material, the total stored energy Ω_{SE} of the volume would be the sum of the free energy and the fracture surface energy,

$$\Omega_{SE} = \int_V \bar{\psi}\left(\varepsilon_{ij}, D_i\right) dV + \int_{S_c} G_c dS \tag{3.22}$$

where G_c represents the critical energy release rate or twice the fracture surface energy in Griffith's theory of brittle fracture. In order to avoid the difficulty inherent in numerically tracking the fracture surface S_c the surface is approximated by the phase-field parameter μ. The formulation initially proposed by[6] and discussed in Chapter 2 is used to approximate the fracture energy, namely,

$$\int_{S_c} G_c dS \approx \int_V G_c \left[\frac{\left(1-\mu\right)^2}{4\ell_0} + \ell_0 \mu_{,i}\mu_{,i}\right] dV \equiv \int_V \psi^{\mu} dV \tag{3.23}$$

where ℓ_0 is a length-scale that governs the size of the region over which the phase-field transitions from 0 to 1 (completely failed to entirely intact). ψ^μ will be added to the partial Hemholtz free energy density $\bar{\psi}$ or partial electrical enthalpy $\bar{h}$ such that the total Hemholtz free energy density or electrical enthalpy will effectively be $\psi = \bar{\psi} + \psi^\mu$ or $h = \bar{h} + \psi^\mu$. Appendix A describes the transformation between energy functions in greater detail.

3.2.2 Boundary Conditions

In addition to approximating the fracture surface energy, the formulation must ensure that the boundary conditions of the discrete crack surfaces are properly represented by the phase-field parameter. Mechanically, the problems investigated by this work primarily employ traction-free crack surfaces. Electrically, several possible boundary conditions are discussed. The permeable boundary condition model, first proposed by[11], recognizes that under the assumptions of linear piezoelectricity, there is no distinction between the undeformed and deformed configurations. Thus, the crack faces are closed and the electrical fields distribute themselves as if the crack does not exist. The impermeable boundary conditions were introduced by[13] and acknowledge that fracture generally occurs when cracks are open. Since the permittivity of the crack gap is usually much lower than that of the solid, its permittivity is idealized to be zero. In contrast, conducting boundary conditions assume that the crack is filled with a conducting fluid such that the electric potential within the crack is homogeneous. Lastly, energetically consistent boundary

conditions, account for the fact that cracks are often open and, in addition, electrical fields can permeate the crack gap. The crack faces are effectively treated as parallel plate capacitors, which also gives rise to closing tractions. These last boundary conditions will be developed using a finite deformation framework and will be presented in Section 3.2.3.

Generally, the Helmholtz free energy for a reversible but nonlinear electromechanical material is written in terms of the strain and electric displacement components, and the electrical enthalpy is given in terms of the strain and electric field. Our prescription for the construction of the associated degraded or damaged energies is simply to pre-multiply the appropriate independent variable by a degradation function $f(\mu)$ that satisfies the following criteria

$$f(1) = 1 \quad \text{and} \quad f(0) = 0. \tag{3.24}$$

Thereafter, the energy retains exactly the same form, but is in terms of the degraded variables. The variables that are degraded and the energy function that is implemented depend upon the type of crack face boundary conditions that are being reproduced. Specifically, each of the first three boundary conditions are implemented in the following way:

$$\varepsilon_{ij}^{P} \equiv f(\mu)\varepsilon_{ij}, \quad E_i^{P} \equiv E_i \quad \text{(Permeable)} \tag{3.25a}$$

$$\varepsilon_{ij}^{I} \equiv f(\mu)\varepsilon_{ij}, \quad E_i^{I} \equiv f(\mu)\, E_i \quad \text{(Impermeable)} \tag{3.25b}$$

$$\varepsilon_{ij}^{C} \equiv f(\mu)\varepsilon_{ij}, \quad D_i^{C} \equiv f(\mu) D_i \quad \text{(Conducting)} \tag{3.25c}$$

Using the results of (3.14) and (3.21) respectively, the chain rule leads to

$$\sigma_{ij} = \frac{\partial h_P}{\partial \varepsilon_{ij}^P} \cdot \frac{\partial \varepsilon_{ij}^P}{\partial \varepsilon_{ij}} = f(\mu)\frac{\partial h_P}{\partial \varepsilon_{ij}^P} \quad \text{and} \quad D_i = -\frac{\partial h_P}{\partial E_i^P} \tag{3.26a}$$

$$\sigma_{ij} = f(\mu)\frac{\partial h_I}{\partial \varepsilon_{ij}^I} \quad \text{and} \quad D_i = -f(\mu)\frac{\partial h_I}{\partial E_i^I} \tag{3.26b}$$

$$\sigma_{ij} = f(\mu)\frac{\partial \psi_C}{\partial \varepsilon_{ij}^C} \quad \text{and} \quad E_i = f(\mu)\frac{\partial \psi_C}{\partial D_i^C} \tag{3.26c}$$

where $h_I = h\left(\varepsilon_{ij}^I, E_i^I, \mu, \mu_{,i}\right)$, $h_P = h\left(\varepsilon_{ij}^P, E_i^P, \mu, \mu_{,i}\right)$, and $\psi_C = \psi\left(\varepsilon_{ij}^C, D_i^C, \mu, \mu_{,i}\right)$. Therefore, by (3.24), when $\mu = 0$ the material is completely degraded and,

$$\sigma_{ij} = 0 \quad \text{for Permeable} \tag{3.27a}$$

$$\sigma_{ij} = 0 \text{ and } D_i = 0 \quad \text{for Impermeable} \tag{3.27b}$$

$$\sigma_{ij} = 0 \text{ and } E_i = 0 \quad \text{for Conducting} \tag{3.27c}$$

The results listed in (3.27) only govern the material behavior within the completely degraded region. However, if we are to consider the resulting boundary conditions, we must analyze the fields in the surrounding material just outside of the degraded boundary layer region. For all three cases, continuity of traction implies that all stresses normal to the boundary layer must be zero, i.e. traction-free. However, as is expected, the stresses that are tangential to the crack faces do not necessarily vanish. In the permeable case, the crack surface does not perturb the electrical fields aside from any coupling to the mechanical fields that are affected by the traction-free conditions. An additional one-dimensional analysis of the permeable case is given in Appendix B, which demonstrates that degrading entire terms in the energy

functional instead of the independent variables is not always appropriate. In the impermeable case, the degraded region acts as a region of zero permittivity resulting in vanishing electric displacements. Then, continuity of electric displacements requires that the normal component of electric displacement adjacent to the boundary layer must be zero; however, like the traction-free conditions, normal continuity of electric displacement imposes no restrictions on the tangential components outside of the boundary layer. Finally, for the conducting case where the electric field vanishes within the crack, continuity of the electric potential requires that tangential components of electric field adjacent to the boundary layer are zero but places no restriction on normal components of the electric field.

Explicitly, the parts of the free energy density or electrical enthalpy density associated with the degraded linear piezoelectric response of the material for each of the crack-face boundary conditions listed above is as follows

$$\bar{h}_P = \frac{1}{2} f(\mu)^2 c^E_{ijkl} \varepsilon_{ij} \varepsilon_{kl} - f(\mu) e_{ijk} E_i \varepsilon_{jk} - \frac{1}{2} \kappa^\varepsilon_{ij} E_i E_j \tag{3.28a}$$

$$\bar{h}_I = f(\mu)^2 \left(\frac{1}{2} c^E_{ijkl} \varepsilon_{ij} \varepsilon_{kl} - e_{ijk} E_i \varepsilon_{jk} - \frac{1}{2} \kappa^\varepsilon_{ij} E_i E_j \right) \tag{3.28b}$$

$$\bar{\psi}_C = f(\mu)^2 \left(\frac{1}{2} c^D_{ijkl} \varepsilon_{ij} \varepsilon_{kl} - h_{ijk} D_i \varepsilon_{jk} + \frac{1}{2} \beta^\varepsilon_{ij} D_i D_j \right) \tag{3.28c}$$

Here c^E_{ijkl} and c^D_{ijkl} are fourth rank tensors of elasticity, e_{ijk} and h_{ijk} are third rank tensors of piezoelectricity, and κ^ε_{ij} and β^ε_{ij} are second rank dielectric tensors. Note that in the absence of degradation ($\mu = 1$) all three forms represent classical linear piezoelectricity. Also, for the problems studied in this work, all material response is assumed to be reversible.

3.2.3 Finite Deformation Formulation

The formulation for the energetically consistent boundary conditions is not as straightforward as outlined above. The complication arises because these boundary conditions are dependent on the crack opening displacement, which is part of the solution of the problem itself. The strategy of the original formulation for the energetically consistent boundary conditions is to capture the effects of the electrical fields carried by the medium filling the crack by using the linear kinematics solution to approximate the new volume of the space created by the open crack[28]. For piezoelectric materials, this allows for the use of linear solutions in the bulk material that are coupled to nonlinear crack-face boundary conditions. Hence, even while the overall linearity of the problem is lost, the nonlinearity is confined to the crack faces, which allows for some analytical solutions, and efficient numerical solution techniques[29]. As noted by[28], even though energetic consistency can be obtained within a linear kinematics setting, the only fully consistent approach to the inclusion of free space within a crack gap and the associated electrical tractions is to resort to a finite deformation framework. For the implementation of these boundary conditions within the phase-field approach there are two issues to consider. First, the introduction of the phase-field degradation function to the free energy now makes the problem nonlinear everywhere, and so the ability to obtain analytical solutions is hopeless for crack problems of interest. Furthermore, since the crack is now a diffuse region of material the identification of the crack opening displacement is not a trivial task, although it can be

approximated. In order to avoid the crack opening identification and to introduce a fully consistent theory, the approach used in this work is to resort to a finite deformation formulation of the problem. Hence, volume and geometry changes due to the existence of open cracks are accounted for explicitly within the theory. In this section, upper-case indices and the " ˜ " symbol will be used to denote quantities in the reference or Lagrangian configuration, and lower-case indices will denote quantities in the deformed or Eulerian configuration. We let V_0 refer to the reference volume bounded by the surface S_0, and let V be the deformed volume bounded by the surface S. A point in the reference configuration is labeled with the position vector $\boldsymbol{X}$. After some process of deformation, this particle moves to a new location labeled with the position vector $\boldsymbol{x}$. The deformation gradient is defined as

$$F_{iJ} \equiv \frac{\partial x_i}{\partial X_J} \tag{3.29}$$

This work employs the Green-Lagrange strain tensor as the measure of deformation defined by

$$\tilde{\varepsilon}_{IJ} \equiv \frac{1}{2}\left(F_{kI}F_{kJ} - \delta_{IJ}\right) \tag{3.30}$$

where δ_{IJ} is the Kronecker delta. The reference electric field vector is calculated as

$$\tilde{E}_I = -\frac{\partial \phi}{\partial x_k}\frac{\partial x_k}{\partial X_I} = E_k F_{kI} = -\phi_{,I} \tag{3.31}$$

and the reference gradient of the phase-field parameter is

$$\mu_{,I} = \mu_{,i} F_{iI} \tag{3.32}$$

Note that the Green-Lagrange strain tensor, the reference electric field, and the reference phase-field gradient are objective measures of strain, electric field and phase-field gradients, respectively, which can be used to characterize these quantities acting within the material in free energy functions and constitutive relations. From (3.1)

$$0 = \int_S t_i dS + \int_V b_i dV = \int_{S_0} P_{Ki} N_K dS_0 + \int_{V_0} b_i J dV_0 \tag{3.33}$$

where J is the determinant of $\boldsymbol{F}$ and P_{Ki} are the components of the first Piola-Kirchhoff stress tensor defined as

$$P_{Ki} \equiv J \sigma_{ji} F^{-1}_{Kj} \tag{3.34}$$

and is linked to the reference traction (force per unit of reference area) as follows

$$P_{Ji} N_J = \tilde{t}_i \quad \text{on } S_0 \tag{3.35}$$

The divergence theorem and arbitrary volume arguments lead to the differential form of the equation of equilibrium

$$P_{Ji,J} + b_i J = P_{Ji,J} + \tilde{b}_i = 0 \quad \text{in } V_0 \tag{3.36}$$

Similarly, from (3.5) we derive the differential form of Gauss's Law for large deformation

$$\tilde{D}_{I,I} = qJ = \tilde{q} \quad \text{in } V_0 \tag{3.37}$$

where the nominal electric displacement $\tilde{D}_J$ is defined such that

$$\int_S D_i n_i dS = \int_{S_0} \tilde{D}_I N_I dS_0 \tag{3.38}$$

as

$$\tilde{D}_J \equiv J D_i F_{Ji}^{-1} \tag{3.39}$$

and is linked to the reference surface charge as follows

$$\tilde{D}_I N_I = -\tilde{\omega} \quad \text{on } S_0 \tag{3.40}$$

Lastly, from (3.9)

$$\begin{aligned} 0 &= \int_S \lambda dS + \int_V (\gamma + \pi)\, dV = \int_S \xi_i n_i dS + \int_V (\gamma + \pi)\, dV \\ &= \int_{S_0} \xi_i F_{Ji}^{-1} N_J J dS_0 + \int_{V_0} (\gamma + \pi)\, J dV_0 \end{aligned}$$

We define $\tilde{\xi}_J$ as

$$\tilde{\xi}_J = J \xi_i F_{Ji}^{-1} \tag{3.41}$$

which leads to

$$\int_{V_0} \left(\tilde{\xi}_{I,I} + \gamma J + \pi J \right) dV \Rightarrow \quad \tilde{\xi}_{I,I} + \tilde{\gamma} + \tilde{\pi} = 0 \quad \text{in } V_0 \tag{3.42}$$

and

$$\tilde{\xi}_I N_I = \tilde{\lambda} \quad \text{on } S_0 \tag{3.43}$$

At this point the electrical enthalpy can take on a multitude of forms designed to capture all of the finite deformation effects of interest. In this work we are still interested in piezoelectric ceramics and as such the deformations will remain small. Hence, we adopt a "quasi-linear" form for the electrical enthalpy analogous to the Saint Venant-Kirchoff model for nonlinear elasticity written as

$$\begin{aligned} \bar{h}_{EC} = f(\mu)^2 \Bigg(& \frac{1}{2} c_{IJKL} \tilde{\varepsilon}_{IJ} \tilde{\varepsilon}_{KL} - e_{KIJ} \tilde{E}_K \tilde{\varepsilon}_{IJ} \\ & - \frac{1}{2} (\kappa_{IJ} - \kappa_0 \delta_{IJ}) \tilde{E}_I \tilde{E}_J \Bigg) - \frac{J \kappa_0}{2} F_{Ik}^{-1} F_{Jk}^{-1} \tilde{E}_I \tilde{E}_J \end{aligned} \tag{3.44}$$

where κ_0 is the linear dielectric permittivity of free-space 8.854×10^{-12} C/Vm. The terms multiplied by the degradation function represents the quasi-linear finite deformation extension of the electrical enthalpy density (3.28b) for impermeable boundary conditions for the material in the absence of the free space that it occupies. Then, the last term represents the electrical enthalpy of the free-space throughout the entire domain of interest, including any new volume that is generated by the opening of cracks. The constitutive relationships are then derived as follows

$$\begin{aligned} &\frac{\partial h_{EC}}{\partial F_{iJ}} = P_{Ji}, \quad \frac{\partial h_{EC}}{\partial \tilde{E}_I} = -\tilde{D}_I, \quad \frac{\partial h_{EC}}{\partial \mu_{,I}} = \tilde{\xi}_I, \\ &\text{and} \quad \frac{\partial h_{EC}}{\partial \mu} = -\tilde{\pi} - \tilde{\beta}\dot{\mu}. \end{aligned} \tag{3.45}$$

Note, for the problems investigated by this work we seek solutions for $\beta = \tilde{\beta} = 0$.

3.2.4 Degradation Function

In the preceding discussion, we have allowed the degradation function f to remain general with the lone requirement being the satisfaction of (3.24). Most previous works, in many cases dedicated solely to mechanical fracture, have utilized a linear form, which results in a quadratic coefficient on stress, i.e.

$$f(\mu) = \mu \tag{3.46}$$

We refer to (3.46) as the standard degradation function. Unfortunately, in the piezoelectric framework, this functional form leads to at least one physically

undesirable behavior as it allows for "anti-damaging" for the cases where impermeable or energetically consistent cracks are occurring. Recall that under quasi-static conditions, the weak form utilized by the finite element method amounts to the minimization of potential energy. We then consider the impermeable crack boundary condition formulation. Ignoring the contributions due to external work, we find that potential energy is minimized as the Hemholtz free energy is minimized, or, equivalently, through a partial Lengendre transformation, as the electrical enthalpy density is minimized with respect to μ for a given strain and electric field state. If we allow strain, electric field, and gradients of the phase-field to be constant, we can preform a term-by-term analysis of how the potential energy is minimized as a function of μ. We list each term below for which a conclusion may be drawn,

$$\frac{1}{2}\mu^2 c^E_{ijkl}\varepsilon_{ij}\varepsilon_{kl} \quad \text{is minimized as } \mu \to 0 \tag{3.47a}$$

$$-\frac{1}{2}\mu^2 \kappa^\varepsilon_{ij} E_i E_j \quad \text{is minimized as } \mu \to \pm\infty \tag{3.47b}$$

$$G_c \frac{(1-\mu)^2}{4\ell_0} \quad \text{is minimized as } \mu \to 1 \tag{3.47c}$$

where the first two statements result from the positive-definiteness of c^E_{ijkl} and κ^ε_{ij} respectively. The piezoelectric term, which depends upon strain and electric field, has no definiteness, but is usually overwhelmed by the elastic and dielectric terms.

Clearly, (3.47b) poses a potential issue. In regions of the body where there exists little to no strain and large electric field, the phase-field parameter can grow to values much larger than 1. This "anti-damaging" effect has no

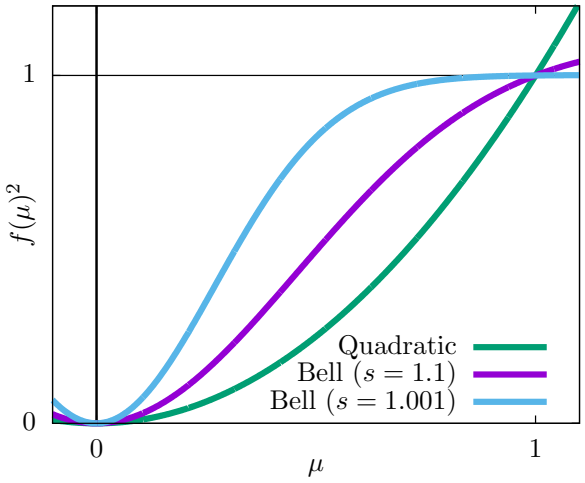

Figure 3.1: The squares of the standard and modified degradation functions plotted for phase-field values slightly outside the desired range of 0 to 1

physical basis and is problematic in the model. Therefore, we consider the new degradation function

$$f(\mu) = \sqrt{s\left[1 - \left(\frac{s-1}{s}\right)^{\mu^2}\right]} \tag{3.48}$$

where $s > 1$ determines the limit of f^2 as $\mu \to \infty$. Notice that the square of this function is a bell curve. We will refer to this as the modified degradation function. For a choice of s slightly larger than 1, the influence of (3.47b) driving large values of μ is sufficiently reduced for reasonable electric fields. More importantly, even in the event that values of μ exceed the desired range of 0 to 1, the influence of the phase-field on the physics is limited by the degradation function which is, in turn, limited by the chosen value of s. Note also that for $s \gg 1$ the modified degradation function converges, in the region

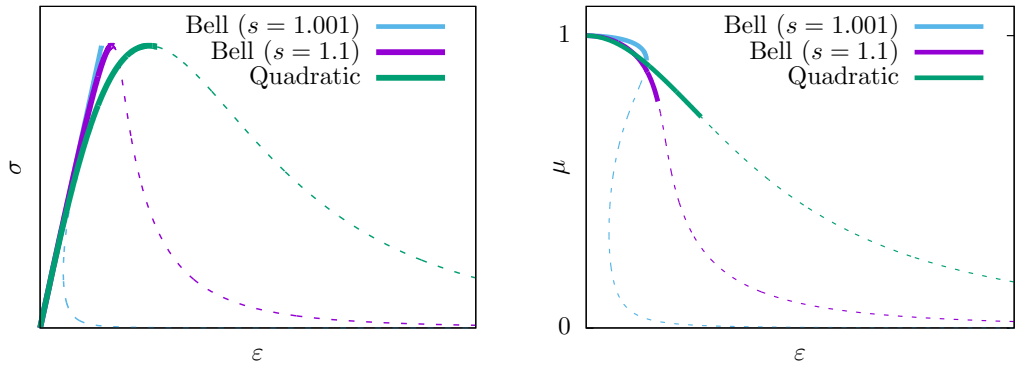

(a) 1-D stress-strain response

(b) 1-D $\mu - \varepsilon$ response

Figure 3.2: 1-D Homogeneous behavior. Solid lines depict the behavior when homogeneity is expected. Dashed lines represent the behavior not likely to occur due to the onset of localization.

of interest, to the standard degradation function. The square of the standard and modified degradation functions for $s = 1.1$ and $s = 1.001$ are plotted in Figure 3.1 for clarity.

Like the cubic degradation function discussed in Chapter 2, the modified degradation function provides a second improvement to the model that is best illustrated when considering homogeneous, uniaxial mechanical response. For this analysis, we set $\phi = 0$ in the entire domain V. Figure 3.2 illustrates the results. As seen in the Figure 3.2a, as s approaches 1, the material response remains nearly perfectly linear up to a critical stress value much like the cubic degradation form. Note that the material response after reaching the peak stress is not indicative of actual material behavior. In reality, once the critical stress is realized, the damage will localize and the homogeneous

solution depicted by the equations above will no longer be valid. This is represented by dashed lines in the figure. For the results presented in Section 3.4 the value $s = 1.1$ is chosen as it sufficiently reduces the "anti-damaging" effect.

3.3 Computational Formulation

We employ the principal of virtual work to represent the governing equations of section 3.2 concisely in the following weak forms:

- Quasi-linear piezoelectricity with permeable and impermeable crack conditions:

$$\begin{aligned} &\int_V \left(\sigma_{ji}\delta\varepsilon_{ij} - D_i\delta E_i - \pi\delta\mu + \xi_i\delta\mu_{,i}\right) dV = \\ &\quad \int_V \left(b_i\delta u_i - q\delta\phi + \gamma\delta\mu\right) dV \\ &+ \int_S \left(t_i\delta u_i - \omega\delta\phi + \lambda\delta\mu\right) dS \end{aligned} \tag{3.49}$$

- Quasi-linear piezoelectricity with conducting crack conditions:

$$\begin{aligned} &\int_V \left(\sigma_{ji}\delta\varepsilon_{ij} + E_i\delta D_i - \pi\delta\mu + \xi_i\delta\mu_{,i}\right) dV = \\ &\quad \int_V \left(b_i\delta u_i + \phi\delta q + \gamma\delta\mu\right) dV \\ &+ \int_S \left(t_i\delta u_i + \phi\delta\omega + \lambda\delta\mu\right) dS \end{aligned} \tag{3.50}$$

- Finite deformation theory with energetically consistent crack conditions:

$$\begin{aligned} &\int_{V_0} \left(P_{Ji}\delta F_{iJ} - \tilde{D}_I\delta\tilde{E}_I - \tilde{\pi}\delta\mu + \tilde{\xi}_I\delta\mu_{,I}\right) dV_0 = \\ &\quad \int_{V_0} \left(\tilde{b}_i\delta u_i - \tilde{q}\delta\phi + \tilde{\gamma}\delta\mu\right) dV_0 \\ &+ \int_{S_0} \left(\tilde{t}_i\delta u_i - \tilde{\omega}\delta\phi + \tilde{\lambda}\delta\mu\right) dS_0 \end{aligned} \tag{3.51}$$

The finite element equations are derived by discretizing the above equations by the Galerkin approximation method and applying the constitutive relations described in the previous section. For (3.49) and (3.51), we discretize u_i, ϕ, and μ in the usual way as the sum of the product of global shape functions and nodal constants, which we refer to as degrees of freedom. For (3.50), we introduce a new quantity φ_i. As described by[109] and[110] it can be shown that in the absence of free charge q, the electrical displacements D_i can be derived from a vector potential φ_j such that

$$D_i = \in_{ijk} \varphi_{j,k} \tag{3.52}$$

where $\in_{ijk}$ is the 3^{rd}-rank permutation tensor. For this formulation we discretize the vector potential φ_i instead of the scalar electric potential ϕ. It is worth noting that in a general 3-dimensional setting, the vector potential formulation introduces two more degrees of freedom per node than what is required for the scalar potential formulation. However, in two dimensions, only one component of the vector potential is required and thus, the number of nodal degrees of freedom for either formulation is equivalent. The primary motivation for introducing the vector potential is to make possible the usage of the relations derived in section 3.2.2 for conducting crack-face boundary conditions. This utilizes the Helmholtz free energy density. If, instead, one choses to use an electrical enthalpy density, terms involving negative powers of the degradation function $f(\mu)$ appear in the weak formulation. These terms are poorly behaved as $\mu \to 0$ (i.e. in or near cracks) and led to highly unstable computational behavior.

3.3.1 Solution Method

Due to the coupled nature of the constitutive relations, the Galerkin method gives rise to a system of nonlinear equations. Two strategies were developed to solve the system. The first is a fully coupled Newton-Raphson method. The second amounts to a Newton-Raphson staggered scheme. For this second scheme, the phase-field degrees of freedom are held constant while, for all cases except the finite deformation, a linear system is solved for the displacements and electric potential. In the finite deformation case, the electromechanical equations at fixed μ are nonlinear and the Newton-Raphson method must be used for their solution. Once the displacement and potential degrees of freedom are calculated they are held constant as a Newton-Raphson scheme is used to solve the micro-force balance equations and calculate the phase-field degrees of freedom. This process is repeated until convergence is achieved. As might be expected, the fully coupled scheme exhibits fast convergence rates (on the order of 4-5 iterations for a reasonable load step), but is highly unstable with respect to the load increment, especially at loads where significant crack propagation occurs. The staggered scheme, to the contrary, routinely requires 300-500 iterations to satisfy similar convergence criteria, but is far less sensitive to the load increment size. The results presented in the following discussion were all calculated using the staggered scheme.

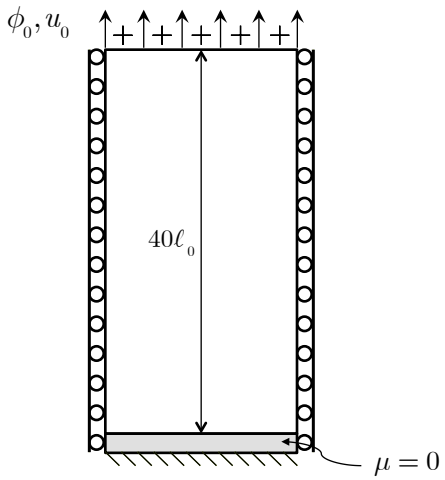

Figure 3.3: 1-D BVP for crack closing tractions. Displacements and electric potential are prescribed on the top surface to induced electric field and corresponding crack closer tractions. The phase-field parameter μ is set to zero for a row of elements on the lower boundary.

3.4 Results and Discussion

In this section we present three calculations to demonstrate the capabilities of the model. First, a 1-D boundary value problem is constructed to demonstrate the presence of crack closing tractions in the energetically consistent formulation and is verified with analytical results. Second, effects on crack lengths for each crack face boundary condition are modeled for a thick double cantilever beam boundary value problem. Lastly, a boundary value problem involving three point bending with an off-set notch is modeled to demonstrate the effects of electric field on fracture trajectories.

3.4.1 1-D Model of Crack Closing Tractions

As detailed in section 3.2.2, energetically consistent crack face boundary conditions give rise to crack closing tractions. For a simple one-dimensional boundary value problem, it is possible to obtain an analytical solution. Specifically, we considered the boundary value problem detailed in Figure 3.3. An initial displacement, u_0, and electric displacement, ϕ_0, is applied at the top of a long piece of piezoelectric material of length L_0 which initially rests on the ground ($\phi = 0$). We denote the resulting separation displacement and electric potential as Δu and $\Delta\phi$ respectively. Using the infinitesimal strain displacement relations (3.4)

$$\varepsilon = \frac{u_0 - \Delta u}{L_0} \tag{3.53}$$

in the solid. The system stored energy is

$$\Omega_{SE} = A_0 L_0 h_{\text{solid}} + A_0 \Delta u h_{\text{gap}} \tag{3.54}$$

where A_0 is the product of the material width and thickness, and the electrical enthalpy density of the gap between the solid and the ground is

$$h_{\text{gap}} = \frac{1}{2}\kappa_0 E_{\text{gap}}^2 \tag{3.55}$$

Energetically consistent boundary conditions dictate that the stored energy of the system remains constant with respect to variations in the gap size. Hence,

$$\begin{aligned} \frac{\partial \Omega_{SE}}{\partial \Delta u} = 0 &= \frac{\partial}{\partial \varepsilon}\frac{d\varepsilon}{d\Delta u}\left(A_0 L_0 h_{\text{solid}}\right) + \frac{\partial}{\partial \Delta u}\left(A_0 \Delta u h_{\text{gap}}\right) \\ &= -A_0 \frac{\partial h_{\text{solid}}}{\partial \varepsilon} + A_0 h_{\text{gap}} \end{aligned} \tag{3.56}$$

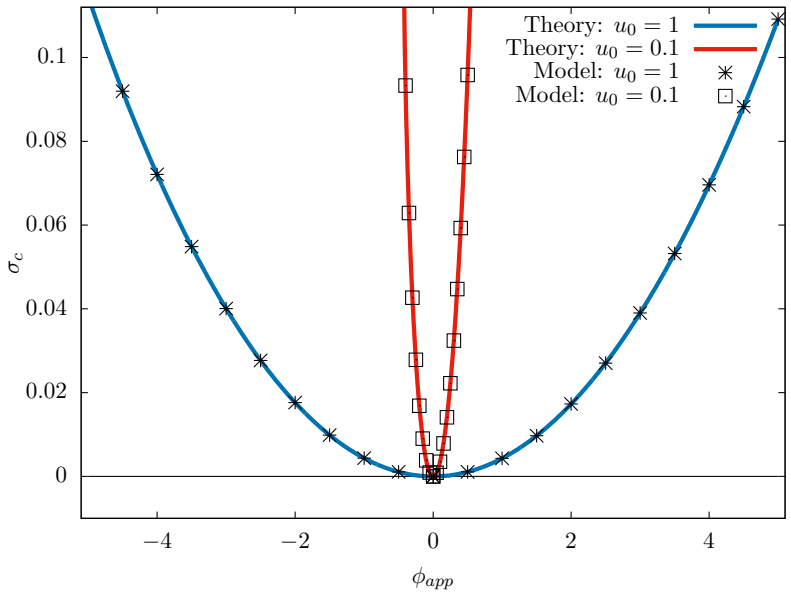

Figure 3.4: Crack closing tractions for the BVP presented in Figure 3.3

and upon application of (3.8) the uniform stress in the piezoelectric strip is

$$\sigma = h_{\text{gap}} = \frac{1}{2}\kappa_0 \left(\frac{\Delta\phi}{\Delta u}\right)^2 \tag{3.57}$$

In order to verify the computational formulation, we discretize the above boundary value problem using 8-noded quadrilateral finite elements, where the resulting mesh is fine near the crack and gradually coarsened as one approaches the top edge. The bottom-most element is completely degraded (i.e. $\mu = 0$) and the displacements of the top nodes of that element are recorded and used to calculate the analytical result. The stress in the upper elements of the mesh represents the uniform stress in the material, which must be the same as the crack closing traction. The corresponding results are illustrated

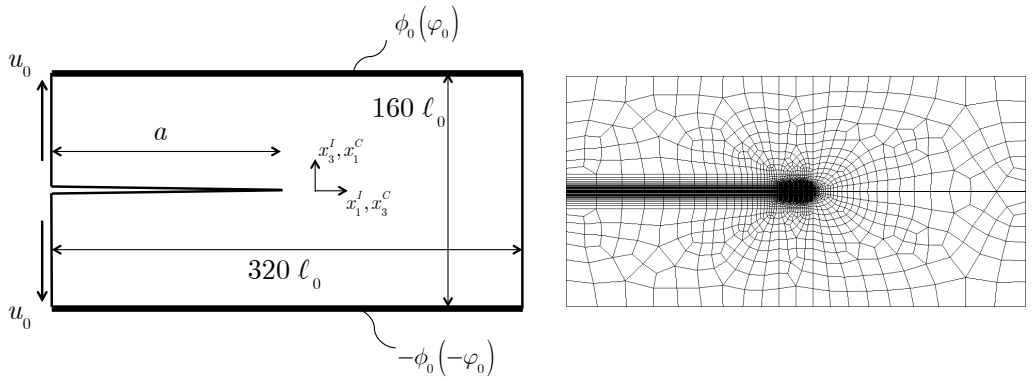

(a) Boundary value problem

(b) Finite element mesh (3780 8-noded quadrilateral elements)

Figure 3.5: The double cantilever beam specimen. An overall electric field is applied in the vertical direction and changes of the phase-field crack length are observed for the various crack-face boundary conditions. The material is poled in the x_3-directions as shown where $\boldsymbol{x}^I$ represents coordinates in problems involving insulating-type crack-face boundary conditions and $\boldsymbol{x}^C$ represents coordinates in problems involving conducting crack-face boundary conditions.

by Figure 3.4. The resulting tractions are determined for two different applied displacements. As is evident by the figure, the finite deformation formulation for handling energetically consistent crack-face tractions is able to accurately capture the crack closing tractions that appear for the simple one-dimensional strip model.

3.4.2 Double Cantilever Beam

In this section we focus on a thick double cantilever beam boundary value problem detailed by Figure 3.5a. 3780 8-noded quadrilateral elements were used as shown in Figure 3.5b. This example illustrates the resulting crack length dependencies on applied electric field for the various crack face boundary conditions that were discussed earlier in the text. In order to study the equilibrium behavior, we have allowed for complete reversibility (i.e. the cracks are allowed to "heal"). The specimen is initially deformed with an applied displacement u_0 until an appropriate crack length is attained. Then, the displacement is held constant as an electric potential ϕ_0 (or scalar potential φ_0) is applied and the resulting crack length is recorded.

As discussed in section 3.3, the conducting boundary conditions lead to a formulation that does not include ϕ as a degree of freedom. The electric potential ϕ is thus not explicitly determined (or utilized as an essential boundary condition) in the current formulation and is not trivial to compute. However, for the current boundary value problem, it can be shown that ϕ is constant on the right and left boundaries and the difference between the two constants is equal to the sum of the electrical forces caused by the application of φ on the top and bottom surfaces. A derivation of this result goes as follows. Let the unit vector $\mathbf{s}$ be chosen such that $\mathbf{n} \times \mathbf{s} = \mathbf{e}_z$, where $\mathbf{e}_z$ is the unit vector normal to the two-dimensional plane containing the structure. The electrical

virtual work statement can be written as,

$$\begin{aligned}
\sum_I \delta\varphi^I F^I &= \int_s \delta\omega\phi \, ds \\
&= \int_{s_\omega} \frac{\partial \delta\varphi}{\partial s}\phi \, ds + \int_{s_\phi} \frac{\partial \delta\varphi}{\partial s}\phi \, ds \\
&= \int_{s_\omega} \frac{\partial}{\partial s}(\delta\varphi\phi) - \delta\varphi\frac{\partial \phi}{\partial s} \, ds + \int_{s_\phi} \frac{\partial \delta\varphi}{\partial s}\phi \, ds \\
&= \delta\varphi^A\phi^{AB} - \delta\varphi^C\phi^{CD} - \int_C^A \delta\varphi\frac{\partial \phi}{\partial s} \, ds \\
&\quad + (\delta\varphi^B - \delta\varphi^A)\phi^{AB} + \delta\varphi^D\phi^{CD} - \delta\varphi^B\phi^{AB} \\
&\quad - \int_B^D \delta\varphi\frac{\partial \phi}{\partial s} \, ds + (\delta\varphi^C - \delta\varphi^D)\phi^{CD} \\
&= -\int_C^A \delta\varphi\frac{\partial \phi}{\partial s} \, ds - \int_B^D \delta\varphi\frac{\partial \phi}{\partial s} \, ds
\end{aligned}$$

Here, $\delta\varphi^I$ represent arbitrary variations of the nodal vector potential at the I^{th} node, and F^I is the associated work-conjugate nodal electrical "force" quantity. This formula reveals two features of the nodal electrical forces for the vector potential formulation. First, if we consider any node I on an electrode that is not on any termination point of that electrode, and taking $\delta\varphi^I = 1$ and all other $\delta\varphi^{J\neq I} = 0$, the formula indicates that $F^I = 0$. So, on a bounding surface, the force-free condition corresponds to a constant electric potential, i.e. an electroded surface. Then, if we take $\delta\varphi = 1$ on the surface between points A and C and zero elsewhere, the formula shows that $\phi^{CD} - \phi^{AB} = \sum_{A\to C} F^I$, where the summation is on the nodes that lie between points A and C on the surface. The same formula can be obtained by taking $\delta\varphi = 1$ on the surface between points B and D and zero elsewhere, in which case the right-hand-side

changes to summing the forces between nodes B and D. In either case, this formula demonstrates that the potential drop between two electrodes can be computed by summing the forces along the boundary connecting two adjacent termination points. Finally the total charge residing between any two points, A and B, on an electrode can also be computed in a straightforward manner using,

$$\int_s \omega \, ds = -\int_s D_i n_i \, ds = \int_A^B \frac{\partial \varphi}{\partial s} \, ds = \varphi^B - \varphi^A. \tag{3.58}$$

Thus, the applied electric field may be obtained through a post processing routine. In the following simulations, electric fields are applied parallel to the poling direction of the piezoelectric material. Hence, the material is poled in the x_3-directions as shown in Figure 3.5a where $\boldsymbol{x}^I$ represents coordinates in problems involving insulating-type crack-face boundary conditions and $\boldsymbol{x}^C$ represents coordinates in problems involving conducting crack-face boundary conditions.

The results for the permeable and conducting boundary conditions are plotted in Figures 3.6a and 3.6b where a_0, the pre-electric field crack length, is approximately 160 ℓ_0. Prior to the application of electrical loading, this crack length is achieved by a suitable choice of the cantilever arm displacement u_0. We observe that resultant crack lengths differ distinctly as a result of the various applied crack face boundary conditions during electrical loading. In the permeable case, the crack is relatively unaffected by the application of field. It should be noted that in the permeable case the electric field is applied prior to

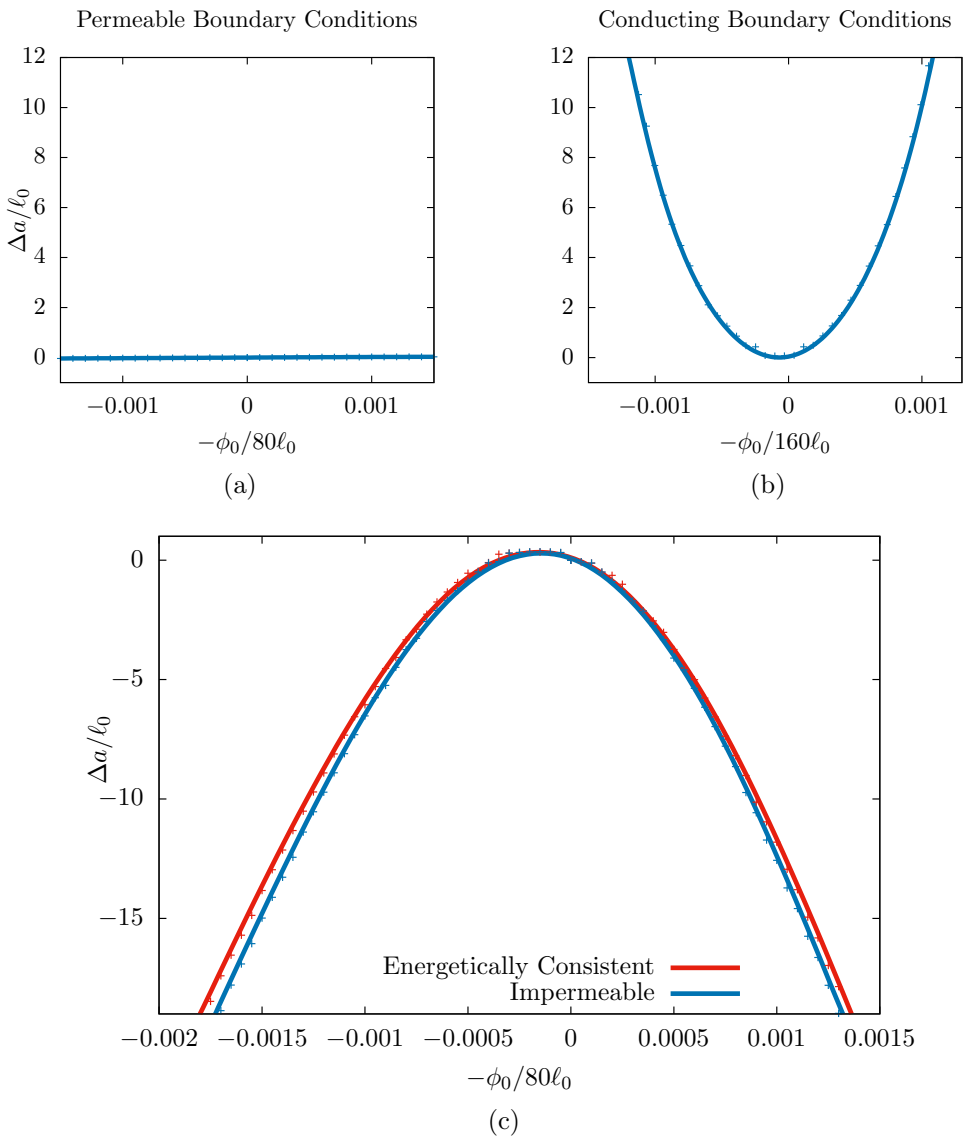

Figure 3.6: Change in crack length under electrical loading for the double cantilever beam. (a) Permeable boundary conditions. (b) Conducting boundary conditions (c) Impermeable and energetically consistent boundary conditions.

the fixed displacement because the piezoelectric effect creates strain throughout the specimen, and an initial displacement of the loaded end. After the electric field is applied, each node on the mechanically loaded end is given an additional fixed displacement u_0. This procedure is not required for the other cases because, at least nominally, the electric field in the cantilever arms is zero, and the extra piezoelectric strain is negligible. Figure 3.6c illustrates the difference between the impermeable (insulating) and the energetically consistent boundary conditions. These sets of results indicate that crack growth can be either impeded or encouraged depending upon applied electric field and the boundary conditions on the crack. Specifically, an applied electric field tends to grow electrically conducting cracks, and heal insulating cracks. For the permeable case, the electrical field has no effect on the crack growth as is expected. In addition, these behaviors are naturally captured by the phase field formulation.

3.4.3 Off-Set Three Point Bending

Lastly, we acknowledge that the true value of the phase-field approximation to fracture is the facility to capture complex, multi-mode, curving crack path trajectories. In this section, a non-symmetric three-point bending boundary value problem[42] is presented to demonstrate this capability and its particular importance in applications involving piezoelectric ceramics. The offset notch, three-point bending, boundary value problem is chosen based on the manifestation of both large normal and shear stresses in the vicinity of the

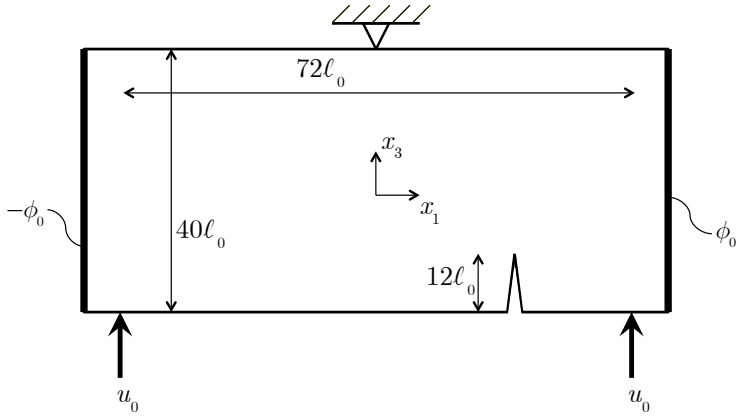

Figure 3.7: The offset notch, three point bending boundary value problem. An overall electric field is applied in the horizontal direction and the material is poled in the vertical direction. An initial phase-field crack of length $12\ell_0$ is set at an offset of $16\ell_0$ from the specimen center.

crack tip resulting in mixed mode fracture. In addition, unlike many boundary value problems where mode II loading is present, large compressive stresses only appear near the application of load and not in the vicinity of the crack tip. This is important, as a shortcoming of the current model is that degradation can emerge in compression in the same manner as it does in tension. Modifications of the phase-field approach to address this issue are available for the mechanical case[8]. Further developments are required for a consistent treatment of the piezoelectric case, which must recognize that tensile stresses can arise even when the strains are contractile due to the piezoelectric effect. The boundary value problem studied here is shown in Figure 3.7.

Specifically, we consider the contrast between an electrically unloaded specimen and one with a horizontally applied electric field. The "notch" de-

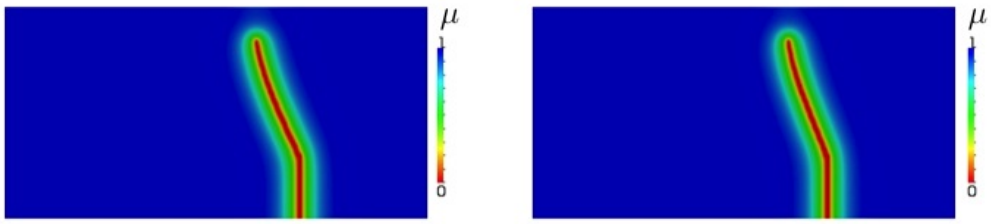

(a)

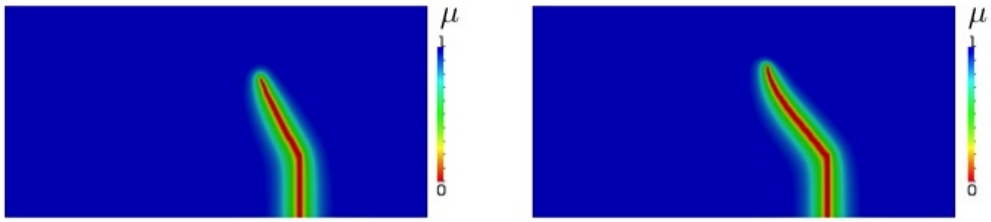

(b)

Figure 3.8: (a) Phase-field values after crack propagation when electrical loading is not present. (b) Phase-field values after crack propagation in the presence of electrical loading and impermeable crack-face boundary conditions. (Left) x_1 poling. (Right) x_3 poling.

picted by Figure 3.7 is modeled by a pre-imposed degradation field. The material is poled in the x_1 and x_3 directions and the crack is modeled as both permeable and impermeable for purposes of comparison. The resulting phase-field values for both poling directions, x_1 on the left and x_3 on the right, with impermeable crack-face boundary conditions are plotted in Figure 3.8. A plot of the electrically unloaded crack paths are contained in Figure 3.8a and loaded in Figure 3.8b. The experimental observations on this geometry are performed on ferroelectric materials (see[111]) making the physical veracity of the resulting crack trajectories in the figure difficult to ascertain. However, it is clear that the model is capable of capturing such non-trivial crack paths. In addition, such behaviors appear to be substantially affected by electrical loadings. In this particular simulation, the difference between the angles at which the crack initially propagates from the notch is very small for for the x_1 poled case, but is estimated to be approximately 18° for the x_3 poled case.

Figure 3.9 depicts the contrasts in crack trajectories when the permeable and impermeable crack face boundary conditions are implemented for the x_3 poling case. In each Figure 3.9(a-d) the left specimen is modeled with a permeable crack and the right one is modeled with an impermeable crack. Figure 3.9a depicts the resulting crack trajectories when there is no electrical loading present. As expected, there is no visible difference in the resulting crack propagation. However, when electrical loading is present, Figure 3.9b, we observe that crack trajectories are unaffected in the permeable case and, as discussed above, are substantially affected in the impermeable case. By

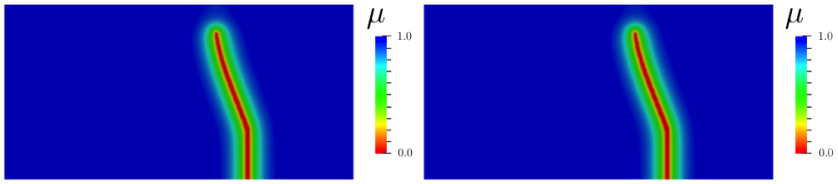

(a)

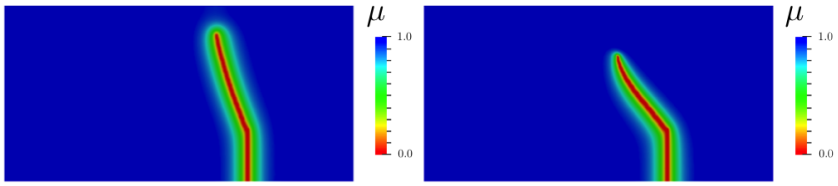

(b)

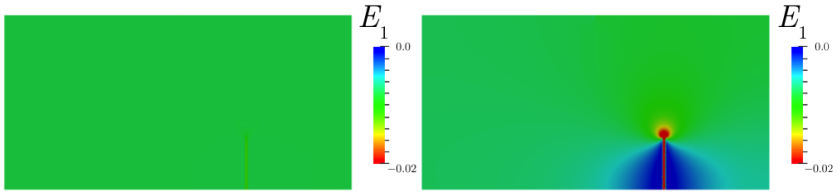

(c)

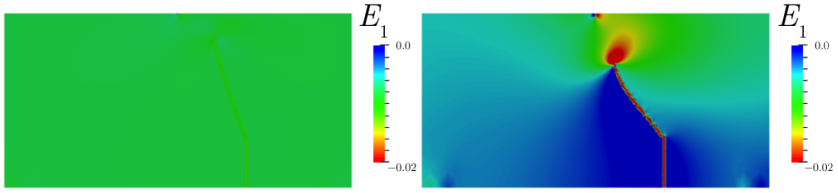

(d)

Figure 3.9: (a) Phase-field values after crack propagation when electrical loading is not present. (b) Phase-field values after crack propagation in the presence of electrical loading. (c) Horizontal component of electric field prior to crack propagation. (d) Horizontal component of electric field following crack propagation. (Left) Permeable conditions. (Right) Impermeable conditions.

looking at the electric fields in the x_1 direction prior to crack propagation (Figure 3.9c) and following crack propagation (Figure 3.9d), we gain some insight into what drives these results. It is well known that an applied electric field perpendicular to the poling direction of a linear piezoelectric material will lead to shear straining. In the permeable case, as expected, we observe that the electric field is unperturbed by the presence of the crack and is thus uniform throughout the body. This leads to a uniform shear strain and the fields near the crack tip remain relatively unchanged. However, due to the impermeable boundary conditions, the electric field behind the crack tip vanishes, but the electric potential in regions of the body where the material is intact must be continuous. The transition zone between these two states, near the crack tip, results in a concentration of electric field. Thus, the increased shearing effect in this area of localized electric field affects the direction in which the crack propagates.

The corresponding structural responses for each impermeable simulation are plotted in Figure 3.10. We introduce the dimensionless quantity m, which is proportional to the resultant moment $M = Fd/2$, as

$$m = \frac{\frac{Fdh}{th^3}}{\sqrt{\frac{c^E_{iiii}G_C}{\ell_0}}} = \frac{Fd\sqrt{\ell_0}}{th^2\sqrt{c^E_{iiii}G_C}} \tag{3.59}$$

where i is the poling direction of the material, $d = 36\ell_0$, and $h = 40\ell_0$. This data demonstrates a distinct variance in load versus displacement response of the specimen. In fact, the specimen with the applied electric field sustains about twice the force of the electrically unloaded one, whereas the overall

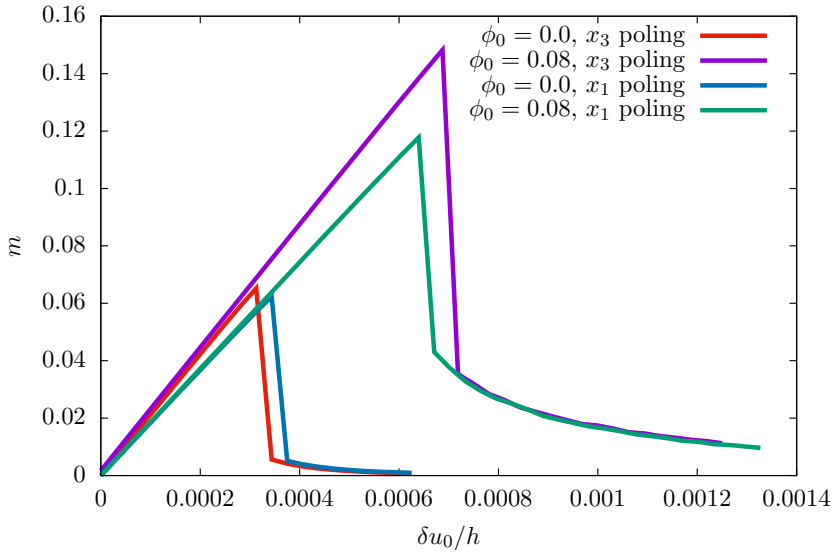

Figure 3.10: Structural response describing the relationship between applied displacements and dimensionless moment for the offset three-point bending BVP with impermeable crack-face boundary conditions.

structural stiffness behavior is essentially identical up to a critical value. For the material poled in the x_1 direction, the application of electric field causes piezoelectric strains that are restrained by the boundary conditions. For this reason, the change in applied displacement is plotted along the x-axis of the figure. It should be noted that the phase-field plots of Figure 3.8 represent the solution immediately after the peak force has been realized for each specimen respectively and, like the crack trajectories, the permeable solutions mimic the structural response of the electrically unloaded specimen. Overall, this simulation indicates that electrical loadings can not only impact the structural response of a material (as alluded to in section 3.4.2), but can also redirect the propagation of a crack.

Chapter 4

Phase-field Modeling of Hydraulic Fracture[1]

4.1 Introduction

We begin by developing the general balance laws and conducting a thorough thermodynamic analysis. We then propose constitutive equations that reproduce the desired responses at the various limits of the phase-field variable. In Section 4.3, we summarize our model equations and outline the numerical methods used to solve the equations. Finally, in Section 4.4, the approach developed is shown to compare favorably to several important analytical solutions. More complex and interesting calculations are also presented to illustrate some of the advantageous features of the approach.

4.2 General Theory

The coupled nature of the problem, with different fluid flow regimes occurring through the intact porous solid and through cracks, and the evolution of a phase-field parameter to identify cracks, will be developed and out-

[1]Based on the journal publication: Zachary A. Wilson and Chad M. Landis, Phase-field modeling of hydraulic fracture, Journal of the Mechanics and Physics of Solids, Volume 96, November 2016, Pages 264-290, ISSN 0022-5096, http://dx.doi.org/10.1016/j.jmps.2016.07.019.

lined here. Throughout the presentation of the general theory the governing equations will be presented in the reference configuration. The relationships between the current and reference configurations are linked through the deformation gradient. The components of the deformation gradient, F_{iJ}, are given by,

$$F_{iJ} = \frac{\partial x_i}{\partial X_J} \quad , \tag{4.1}$$

where x_i are the Cartesian coordinates of a material point of the aggregate in the current state defined by the spatial domain V bounded by the surface S, and X_I are Cartesian coordinates of the same material point in the reference state corresponding to the reference domain V_0 bounded by the surface S_0. Index notation will be used throughout the presentation with summation assumed over repeated indices, lowercase indices referring to the current configuration, and uppercase indices referring to the reference configuration. The relationship between surface elements in the reference and current configurations is given by Nanson's formula as $n_i dS = JF^{-1}_{Ji} N_J dS_0$, and for volume elements is $dV = JdV_0$, where n_i and N_J are components of the unit normal to the surface in the current and reference configurations respectively, J is the determinant of the deformation gradient, and F^{-1}_{Ji} is the inverse of the deformation gradient such that $F^{-1}_{Ji} = \partial X_J / \partial x_i$.

4.2.1 Mass Balances

First consider the conservation of mass for a fractured, fluid saturated, porous solid. Following the work of Coussy[112–116] the porous solid and the

fluid will together be referred to as the aggregate. In order to develop the theory within the phase-field framework we identify the total reference domain V_0, which contains both cracks and pores and is unchanging while fluid may be convected into and out of this domain.

First, the total solid mass of the system remains fixed for all time, and as such, conservation of mass for the solid can be written as,

$$\frac{D}{Dt}\int_{V_0}(1-\phi)\,\rho^s J\,dV_0 = 0 \quad , \tag{4.2}$$

where ϕ is the reference volume fraction of porosity in the aggregate, which is assumed to always be filled by fluid, and ρ^s is the mass density of the solid. The notation D/Dt represents the time derivative with respect to an observer attached to a material point of the aggregate. Given that this equation must hold for any arbitrary region of the reference domain, the integrand must be zero pointwise, i.e.

$$\frac{D}{Dt}\left[(1-\phi)\,\rho^s J\right] \equiv \left[(1-\dot{\phi})\,\rho^s J\right] = 0 \quad . \tag{4.3}$$

Equation (4.3) is the mass balance equation for the solid.

The total conservation of mass for the system is given by,

$$\frac{D}{Dt}\int_{V_0}\left[(1-\phi)\,\rho^s + \phi\rho^f\right] J\,dV_0 = -\int_{S_0}\rho^f \tilde{w}_I N_I\,dS_0 + \int_{V_0}\rho^f \tilde{m}\,dV_0 \quad , \tag{4.4}$$

where ρ^f is the mass density of the fluid, $\tilde{w}_I$ is the volume of fluid traversing a unit of reference area of the aggregate per unit of time, and $\tilde{m}$ is the fluid volume injected per unit of reference volume. Note that the nominal fluid flux

$\tilde{w}_I$ is related to the true fluid flux w_i as $w_i = \tilde{w}_K F_{iK}/J$. The right-hand side of the equation represents the mass that enters the system through its surface and volume respectively.

Combining (4.2) and (4.4), the conservation of fluid mass of the system is,

$$\frac{D}{Dt}\int_{V_0} \phi\rho^f J \, dV_0 = -\int_{S_0} \rho^f \tilde{w}_I N_I dS_0 + \int_{V_0} \rho^f \tilde{m} dV_0 \quad . \tag{4.5}$$

Applying the divergence theorem, and taking (4.5) to be valid for any arbitrary volume, the point-wise form of the fluid mass balance becomes,

$$\dot{(\phi\rho^f J)} = -\left(\rho^f \tilde{w}_I\right)_{,I} + \rho^f \tilde{m} \quad . \tag{4.6}$$

4.2.2 Momentum Balances

Anticipating how the equations of this theory will eventually be solved numerically, the focus of the momentum balance equations will be placed on the aggregate and then on the fluid. For the aggregate, the balance of linear momentum is written as,

$$\begin{aligned}\frac{D}{Dt}\int_{V_0} &\left[(1-\phi)\,\rho^s v_i + \phi\rho^f \left(v_i + v_i^{f/s}\right)\right] J\, dV_0 \\ &= \int_{S_0} \tilde{t}_i \, dS_0 + \int_{V_0} \tilde{b}_i \, dV_0 - \int_{S_0} \rho^f \tilde{w}_K N_K \left(v_i + v_i^{f/s}\right) \, dS_0 \\ &\quad + \int_{V_0} \rho^f \tilde{m} \left(v_i + v_i^{f/s}\right) \, dV_0\end{aligned} \quad . \tag{4.7}$$

The components of the traction per unit reference area and body force per reference volume are $\tilde{t}_i$ and $\tilde{b}_i$. Note that the tractions and body forces appearing here are external to the solid/fluid aggregate. Additionally, we adopt

the following ansatz that the average fluid velocity relative to the solid aggregate, $v_i^{f/s}$, is related to the true fluid flux by $w_i = \phi v_i^{f/s}$. The left-hand side of (4.9) represents the rate of change of the total momentum of the solid/fluid aggregate contained within the domain V_0. The right-hand side of the equation consists of two parts; the sum of the external forces acting on the volume, and the fluid momentum convected and injected into the volume. Note that it is assumed that the fluid injected by external sources is injected into the volume with the same velocity as the existing fluid. Next, the standard hypothesis is adopted such that the first Piola-Kirchhoff stress components, P_{Ji}, are related to the nominal surface traction by,

$$\tilde{t}_i = P_{Ji} N_J \quad \text{on} \quad S_0 \quad . \tag{4.8}$$

The Cauchy stress is related to the first Piola-Kirchhoff stress in the normal manner as, $\sigma_{ji} = F_{jK} P_{Ki}/J$.

Application of the traction-stress relation (4.8), the divergence theorem, the mass balance equations (4.3) and (4.6), and noting that the momentum balance must hold for arbitrary volumes leads to the pointwise form for Newton's second law for the aggregate,

$$\begin{aligned} &P_{Ki,K} + \tilde{b}_i \\ &\qquad = (1-\phi)\,\rho^s J \dot{v}_i + \phi \rho^f J \dot{\Big(} v_i + \dot{v}_i^{f/s} \Big) + \phi \rho^f J \Big(v_i + v_i^{f/s} \Big)_{,K} \dot{F}_{Kj}^{-1} v_j^{f/s} \end{aligned} \tag{4.9}$$

The time derivative, $\overset{\circ}{(\ )}$ for an observer moving with a fluid particle is given by,

$$\overset{\circ}{(a)} = \dot{a} + a_{,i} v_i^{f/s} = \dot{a} + a_{,K} F_{Ki}^{-1} v_i^{f/s} \quad . \tag{4.10}$$

Therefore, (4.9) can be re-written as,

$$P_{Ki,K} + \tilde{b}_i = (1-\phi)\,\rho^s J\dot{v}_i + \phi\rho^f J\left(v_i + \overset{\circ}{v_i^{f/s}}\right) \quad . \tag{4.11}$$

Next, the balance of angular momentum for the aggregate is given by,

$$\begin{aligned}
&\frac{D}{Dt}\int_{V_0} \epsilon_{ijk}\left[(1-\phi)\,\rho^s x_j v_k + \phi\rho^f x_j\left(v_k + v_k^{f/s}\right)\right] J dV_0 \\
&\quad = \int_{S_0} \epsilon_{ijk} x_j \tilde{t}_k\, dS_0 + \int_{V_0} \epsilon_{ijk} x_j \tilde{b}_k\, dV_0 \\
&\qquad - \int_{S_0} \rho^f \tilde{w}_M N_M \epsilon_{ijk} x_j \left(v_k + v_k^{f/s}\right)\, dS_0 \\
&\qquad + \int_{V_0} \rho^f \tilde{m} \epsilon_{ijk} x_j \left(v_k + v_k^{f/s}\right)\, dV_0
\end{aligned} \quad . \tag{4.12}$$

Here ϵ_{ijk} are the components of the permutation tensor, and x_i are the components of the position of a particle in the current configuration of the aggregate. Application of the previously established procedures yields the pointwise consequence of the angular momentum balance as,

$$\epsilon_{ijk}\left(P_{Lj}F_{kL} - J\rho^f w_j v_k - J\rho^f w_k v_j\right) = 0 \quad \rightarrow \quad P_{Ki}F_{jK} = P_{Kj}F_{iK} \quad . \tag{4.13}$$

The implication of (4.13) is that the aggregate Cauchy stress is symmetric.

For the fluid, the linear momentum balance is,

$$\begin{aligned}
&\frac{D}{Dt}\int_{V_0} \phi\rho^f \left(v_i + v_i^{f/s}\right)\, J dV_0 \\
&\quad = \int_{S_0} \tilde{t}_i^f dS_0 + \int_{V_0} \left(\tilde{b}_i^f + \tilde{f}_i^{sf}\right) dV_0 \\
&\qquad - \int_{S_0} \rho^f \tilde{w}_K N_K \left(v_i + v_i^{f/s}\right)\, dS_0 + \int_{V_0} \rho^f \tilde{m}\left(v_i + v_i^{f/s}\right)\, dV_0
\end{aligned} \quad . \tag{4.14}$$

Here, the components of the net traction on the fluid per unit of aggregate reference area are $\tilde{t}_i^f$, the components of the fluid body force per unit of aggregate

reference volume supplied by external sources are $\tilde{b}_i^f$, and the components of the body force per unit aggregate reference volume that the solid places upon the fluid are $\tilde{f}_i^{sf}$. Here we adopt the ansatz that the fluid traction $\tilde{t}_i^f$ is related to the fluid stress by,

$$\tilde{t}_i^f = \phi T_{Ki} N_K = \phi \left(\tau_{ji} - p\delta_{ij}\right) J F_{Kj}^{-1} N_K \quad , \tag{4.15}$$

where the components of the first Piola-Kirchhoff stress in the fluid are T_{Ji}, and the Cauchy fluid stress components have been decomposed into the hydrostatic pressure p and the deviatoric part τ_{ij}. Here we have introduced the Kronecker delta components δ_{ij}. Again, notice that fluid momentum is convected and injected into the volume of the aggregate being considered. Analysis of (4.14) using the previously discussed procedures along with (4.10) and (4.15) gives the pointwise form for Newton's second law for the fluid,

$$\left(\phi T_{Ji}\right)_{,J} + \tilde{b}_i^f + \tilde{f}_i^{sf} = \phi \rho^f J \left(\overset{\circ}{v_i + v_i^{f/s}}\right) \quad . \tag{4.16}$$

The balance of angular momentum for the fluid is,

$$\begin{aligned} &\frac{D}{Dt}\int_{V_0} \epsilon_{ijk}\phi\rho^f x_j \left(v_k + v_k^{f/s}\right) J dV_0 \\ &\quad = \int_{S_0} \epsilon_{ijk} x_j \tilde{t}_k^f \, dS_0 + \int_{V_0} \epsilon_{ijk} x_j \left(\tilde{b}_k^f + \tilde{f}_k^{sf}\right) \, dV_0 \\ &\qquad - \int_{S_0} \rho^f \tilde{w}_M N_M \epsilon_{ijk} x_j \left(v_k + v_k^{f/s}\right) \, dS_0 \\ &\qquad + \int_{V_0} \rho^f \tilde{m} \epsilon_{ijk} x_j \left(v_k + v_k^{f/s}\right) \, dV_0 \end{aligned} \quad . \tag{4.17}$$

The analysis of this integral form provides the pointwise form of angular fluid momentum,

$$\epsilon_{ijk}\left(\phi T_{Lj} F_{kL} - J\rho^f w_j v_k - J\rho^f w_k v_j\right) = 0 \quad \rightarrow \quad T_{Li} F_{jL} = T_{Lj} F_{iL} \quad . \tag{4.18}$$

We note that (4.11) and (4.16), along with the relationship for the fluid force on the solid per unit aggregate volume, $\tilde{f}_i^{fs} = -\tilde{f}_i^{sf}$, can be used to derive Newton's second law for the solid as,

$$\left(P_{Ji} - \phi T_{Ji}\right)_{,J} + \underbrace{\tilde{b}_i - \tilde{b}_i^f}_{\tilde{b}_i^s} - \tilde{f}_i^{sf} = \left(1 - \phi\right) J \rho^s \dot{v}_i \quad . \tag{4.19}$$

Here we have introduced the definition of the external body force acting on the solid per unit aggregate volume $\tilde{b}_i^s$.

4.2.3 Micro-forces and their Balance

Within this theory the material is allowed to fail or damage according to the phase-field theory of fracture for brittle solids. Using the phase-field damage parameter, following the approach of Fried, Gurtin, and others[101,102,117], we need also to introduce a set of conjugate forces associated with changes in this quantity. To this end, we define $\tilde{\iota}$ as an external surface micro-force such that $\tilde{\iota}\dot{\mu}$ is the power expended per unit area of aggregate surface by sources external to the volume under consideration, $\tilde{\gamma}$ is an external body micro-force such that $\tilde{\gamma}\dot{\mu}$ is the power expended per unit aggregate volume by external sources, and $\tilde{\pi}$ is an internal micro-force per unit aggregate volume such that $\tilde{\pi}\dot{\mu}$ is the power expended internally on the material per unit volume[96]. We also assume that on the surface there is a balance between the applied surface micro-force $\tilde{\iota}$ and the material micro-force vector $\tilde{\xi}_i$ such that,

$$\tilde{\iota} = \tilde{\xi}_J N_J \quad \text{on} \quad S_0 \quad . \tag{4.20}$$

It is then also assumed that there exists a net balance of this set of micro-forces such that,

$$\int_{S_0} \tilde{\imath}\, dS_0 + \int_{V_0} \tilde{\gamma}\, dV_0 + \int_{V_0} \tilde{\pi}\, dV_0 = 0 \quad . \tag{4.21}$$

Application of the divergence theorem, (4.20), and the argument that the micro-force balance must hold for any arbitrary volume yields the pointwise micro-force balance equation,

$$\tilde{\xi}_{I,I} + \tilde{\gamma} + \tilde{\pi} = 0 \quad . \tag{4.22}$$

4.2.4 Energy Balances

Next, consider the balance of energy in the solid/fluid aggregate. The integral form for the first law of thermodynamics for a given aggregate volume is written as,

$$\begin{aligned}
&\frac{D}{Dt}\int_{V_0} \left[\tfrac{1}{2}\left(1-\phi\right)\rho^s v_i\, v_i + \left(1-\phi\right)\rho^s e^s\right] J dV_0 \\
&+ \frac{D}{Dt}\int_{V_0} \left[\tfrac{1}{2}\phi\rho^f \left(v_i + v_i^{f/s}\right)\left(v_i + v_i^{f/s}\right) + \tfrac{1}{2}\phi\rho^f A v_i^{f/s} v_i^{f/s} + \phi\rho^f e^f\right] J dV_0 \\
&= \int_{S_0} \tilde{t}_i v_i\, dS_0 + \int_{V_0} \left[\tilde{b}_i v_i + \tilde{b}_i^f v_i^{f/s}\right] dV_0 + \int_{S_0} \tilde{t}_i^f v_i^{f/s}\, dS_0 + \int_{V_0} \tilde{m} p dV_0 \\
&+ \int_{S_0} \tilde{\imath}\dot{\mu}\, dS_0 + \int_{V_0} \tilde{\gamma}\dot{\mu} dV_0 - \int_{S_0} \tilde{q}_J N_J\, dS_0 + \int_{V_0} \tilde{r} dV_0 \\
&- \int_{S_0} \rho^f \tilde{w}_K N_K \left[\tfrac{1}{2}\left(v_i + v_i^{f/s}\right)\left(v_i + v_i^{f/s}\right) + \tfrac{1}{2} A v_i^{f/s} v_i^{f/s} + e^f\right] dS_0 \\
&+ \int_{V_0} \rho^f \tilde{m} \left[\tfrac{1}{2}\left(v_i + v_i^{f/s}\right)\left(v_i + v_i^{f/s}\right) + \tfrac{1}{2} A v_i^{f/s} v_i^{f/s} + e^f\right] dV_0
\end{aligned} \tag{4.23}$$

Again, notice that the definitions of the body forces are in terms of the forces per unit aggregate reference volume such that the total body force $\tilde{b}_i$ is simply the sum of the external body force per unit aggregate volume on the fluid $\tilde{b}_i^f$ and the external body force per unit aggregate volume on the solid $\tilde{b}_i^s$. Also appearing in the energy balances are the volumetric sources of heat $\tilde{r}$ supplied per unit reference volume of the aggregate per unit of time. Note that the total heat supply to the aggregate $\tilde{r}$ includes heat supplied both to the solid and to the fluid, which is partitioned as $\tilde{r} = \tilde{r}^s + \tilde{r}^f$. Then, $\tilde{q}_I$ are the components of the net heat flux traversing a unit reference area of the aggregate per unit of time. Likewise, the total heat flux $\tilde{q}_I$ represents contributions from the solid and the fluid such that it can be partitioned into contributions per unit aggregate reference area as $\tilde{q}_I = \tilde{q}_I^s + \tilde{q}_I^f$. The additional freshly introduced quantities are the internal energy per unit mass of solid e^s, the internal energy per unit mass of fluid e^f, and the tortuosity A.

The left-hand side of this energy balance equation contains the time rate of change of the kinetic and internal energy contained within a region of the solid/fluid aggregate. Aside from the term containing the tortuosity, each of these terms is conventional, with the kinetic and internal energies of the solid and fluid partitioned through the porosity. The additional term $\frac{1}{2}\phi\rho^f A v_i^{f/s} v_i^{f/s}$ accounts for the kinetic energy of the fluid per unit aggregate volume that is omitted by the term $\frac{1}{2}\phi\rho^f \left(v_i + v_i^{f/s}\right)\left(v_i + v_i^{f/s}\right)$. Since $\left(v_i + v_i^{f/s}\right)$ is the average velocity of the fluid, it is valid to claim that the integral of the average velocity is equivalent to the integral of the velocity, however such a

relationship does not hold for the square of the velocity and the square of the average velocity. Hence, it is common to introduce the tortuosity to account for this discrepancy. Note that the form for the kinetic energy correction $\frac{1}{2}\phi\rho^f A v_i^{f/s} v_i^{f/s}$ assumes that the fluctuation of the total fluid velocity about its average value is proportional to the average relative velocity of the fluid with respect to the solid, $v_i^{f/s}$. In general, the tortuosity A will depend upon the specific structure of the porosity, the porosity itself, and the relative fluid velocity $v_i^{f/s}$ [112].

The first line of the right-hand side of this energy balance equation includes the power expended by the total traction on the aggregate surface, the power expended by the external body forces on the solid and fluid accounted for separately, the power expended by the fluid stress on the relative velocity at the surface (the power expended by the fluid stress on the aggregate velocity v_i is included in the work done by the total traction), and the power expended by external sources to inject additional fluid volume into the aggregate. The second line of the right-hand side includes the power expended by external micro-forces on the surface and in the volume of the aggregate, and the rate of heat supplied to the aggregate volume across its surface and to the volume directly. Note that since it is an internal force, the internal micro-force $\tilde{\pi}$ does not enter the energy balance equation. This is analogous to the fact that the internal force that the solid places upon the fluid, $\tilde{f}_i^{sf}$, does not enter this energy balance equation either. Finally, the last two lines of the right-hand side represent the energy convected into the volume through its surface, and

injected into the volume directly. Note that these terms contain both kinetic and stored energy contributions from the fluid, and it is assumed that the fluid injected directly into the volume arrives with the prevailing kinetic and internal energy of the existing fluid.

The analysis of the energy balance equation requires the use of the mass balances (4.3) and (4.6), the momentum balances (4.11) and (4.16), and the micro-force balance (4.22), leading to the following pointwise form for the first law for the solid/fluid aggregate,

$$\begin{aligned}
&(1-\phi)\,J\rho^s\dot{e}^s + \phi J\rho^f\,\overset{\circ}{e}{}^f + \phi J\rho^f\left(\tfrac{1}{2}A\overset{\circ}{v}{}_i^{f/s}v_i^{f/s}\right)\\
&\quad = \left(P_{Ji}-\phi\tilde{\tau}_{Ji}\right)v_{i,J} + \phi\tilde{\tau}_{Ji}\Big(v_i+v_i^{f/s}\Big)_{,J} + \phi pJ\frac{\overset{\circ}{\rho}{}^f}{\rho^f} + p(\dot{\phi J})\\
&\qquad + \left[p\big(\phi JF_{Ji}^{-1}\big)_{,J} - \tilde{f}_i^{sf}\right]v_i^{f/s} + \tilde{\xi}_I\dot{\mu}_{,I} - \tilde{\pi}\dot{\mu} - \tilde{q}_{I,I} + \tilde{r}
\end{aligned} \quad . \tag{4.24}$$

Here we have introduced the first Piola-Kirchhoff stress in the fluid associated with the deviatoric part of the fluid stress τ_{ji}, $\tilde{\tau}_{Ji} = JF_{Jk}^{-1}\tau_{ki}$.

It is also useful to analyze the energy balances for the solid and fluid separately, noting that the sum of the solid and fluid energies must equate to the solid/fluid aggregate energy. For the solid, the first law energy balance is,

$$\begin{aligned}
&\frac{D}{Dt}\int_{V_0}\left[\tfrac{1}{2}\left(1-\phi\right)\rho^s v_i\,v_i + \left(1-\phi\right)\rho^s e^s\right]JdV_0\\
&\quad = \int_{S_0}\left(\tilde{t}_i-\tilde{t}_i^f\right)v_i\,dS_0 + \int_{V_0}\tilde{b}_i^s v_i dV_0 + \int_{S_0}\tilde{\iota}\dot{\mu}\,dS_0 + \int_{V_0}\tilde{\gamma}\dot{\mu}dV_0\\
&\qquad - \int_{S_0}\tilde{q}_J^s N_J\,dS_0 + \int_{V_0}\left(\tilde{r}^s+\tilde{r}^{fs}\right)dV_0 + \int_{V_0}\dot{\varpi}^{fs}dV_0
\end{aligned} \quad . \tag{4.25}$$

Note, that as for the body forces, the surface traction can be decomposed into its solid and fluid contributions per unit aggregate reference area. In (4.25)

the traction associated with the solid is $\tilde{t}_i^s = \tilde{t}_i - \tilde{t}_i^f$. The mechanical power density that the fluid transfers to the solid per unit of time is $\dot{\varpi}^{fs}$, and the thermal power density that the fluid transfers to the solid per unit of time is r^{fs}. The mechanical power per reference volume that the solid transfers to the fluid, $\dot{\varpi}^{sf}$, the force that the solid imparts upon the fluid, $\tilde{f}_i^{sf}$, and the heat that the solid transfers to the fluid, $\tilde{r}^{sf}$, are each the opposites of those from the fluid to the solid. The mechanical power density that the fluid transfers to the solid, $\dot{\varpi}^{fs}$, consists of the dot product of the force density of the fluid on the solid with the solid velocity and the fluid pressure working to open up additional porosity. Hence, the power term $\dot{\varpi}^{fs}$, is given by,

$$\dot{\varpi}^{fs} = \tilde{f}_i^{fs} v_i + pJ\dot{\phi} \quad . \tag{4.26}$$

The pointwise form for the first law for the solid obtained from the analysis of (4.25), (4.3), (4.19), (4.22), and (4.26) is,

$$(1-\phi)\, J\rho^s \dot{e}^s = (P_{Ji} - \phi\tilde{\tau}_{Ji})\, v_{i,J} + p(\dot{\phi J}) + \tilde{\xi}_I \dot{\mu}_{,I} - \tilde{q}^s_{I,I} + \tilde{r}^s - \tilde{r}^{sf} - \tilde{\pi}\dot{\mu} \quad . \tag{4.27}$$

Adopting the following stress partition, the solid stress P^s_{Ji} is defined as,

$$(1-\phi)\, P^s_{Ji} = P_{Ji} - \phi T_{Ji} \quad , \tag{4.28}$$

and (4.27) can be rewritten as,

$$\begin{aligned}(1-\phi)\, J\rho^s \dot{e}^s = &\left[(1-\phi)\, P^s_{Ji} - \phi J F^{-1}_{Ji} p\right] v_{i,J} + p(\dot{\phi J}) \\ &- \tilde{\pi}\dot{\mu} + \tilde{\xi}_I \dot{\mu}_{,I} - \tilde{q}^s_{I,I} + \tilde{r}^s - \tilde{r}^{sf}\end{aligned} \quad . \tag{4.29}$$

Then, the first law energy balance for the fluid is simply the difference between the aggregate energy balance and the solid energy balance,

$$\begin{aligned}
&\phi J\rho^f \overset{\circ}{e^f} + \phi J\rho^f \left(\tfrac{1}{2} A v_i^{f/s} \overset{\circ}{v_i^{f/s}}\right) \\
&\quad = \phi J p \frac{\overset{\circ}{\rho^f}}{\rho^f} + \phi \tilde{\tau}_{Ji}\Big(v_i + v_i^{f/s}\Big)_{,J} \\
&\qquad - \tilde{q}^f_{I,I} + \tilde{r}^f + \tilde{r}^{sf} + \Big[p\big(\phi J F^{-1}_{Ji}\big)_{,J} - \tilde{f}_i^{sf}\Big] v_i^{f/s}
\end{aligned} \quad . \tag{4.30}$$

4.2.5 Entropy Inequalities

In this section the entropy inequalities arising from the second law of thermodynamics for the solid, fluid, and solid/fluid aggregate are analyzed. First, consider the continuum form for the second law of thermodynamics for the solid,

$$\frac{D}{Dt}\int_{V_0} (1-\phi)\,\rho^s s^s J dV_0 \geq -\int_{S_0} \frac{\tilde{q}^s_J N_J}{\theta^s}\, dS_0 + \int_{V_0} \frac{\tilde{r}^s - \tilde{r}^{sf}}{\theta^s} dV_0 \quad . \tag{4.31}$$

Here, the left-hand side of the inequality is the rate of change of the entropy in the solid, and the right-hand side represents the entropy transfer to the solid. Next, we introduce the Helmholtz free energy per unit mass for the solid as,

$$\psi^s = e^s - s^s\theta^s \quad . \tag{4.32}$$

Application of (4.3), (4.27), and (4.32) yields the pointwise form for the entropy inequality for the solid as,

$$\begin{aligned}
(1-\phi)\, J\rho^s \dot{\psi}^s \leq &\left[(1-\phi)\, P^s_{Ji} - \phi J F^{-1}_{Ji} p\right] v_{i,J} + p(\dot{\phi J}) \\
&- \tilde{\pi}\dot{\mu} + \tilde{\xi}_I \dot{\mu}_{,I} - (1-\phi)\, J\rho^s s^s \dot{\theta}^s - \frac{1}{\theta^s}\tilde{q}^s_I \theta^s_{,I}
\end{aligned} \quad . \tag{4.33}$$

We now assume that the Helmholtz free energy of the solid ψ^s, the solid stress P^s_{Ji}, the internal micro-force vector $\tilde{\xi}_I$, the internal micro force $\tilde{\pi}$, the solid entropy density s^s, and the heat flux in the solid $\tilde{q}^s_I$, each can depend upon the temperature in the solid θ^s, its gradient $\theta^s_{,I}$, the true porosity ϕJ, the phase-field variable μ, its gradient $\mu_{,I}$, its rate $\dot{\mu}$, and the deformation gradient F_{iJ}. The velocity gradient is related to the material time derivative of the deformation gradient as $\dot{F}_{iK} = F_{jK} v_{i,j}$. Equation (4.33) becomes,

$$\begin{aligned} 0 \geq & \left[(1-\phi)\, J\rho^s \frac{\partial \psi^s}{\partial F_{iJ}} - (1-\phi)\, P^s_{Ji} + \phi J F^{-1}_{Ji} p \right] v_{i,J} \\ & + \left[(1-\phi)\, J\rho^s \frac{\partial \psi^s}{\partial \mu_{,I}} - \tilde{\xi}_I \right] \dot{\mu}_{,I} + \left[(1-\phi)\, J\rho^s \frac{\partial \psi^s}{\partial \mu} + \tilde{\pi} \right] \dot{\mu} \\ & + \left[(1-\phi)\, J\rho^s \frac{\partial \psi^s}{\partial \dot{\mu}} \right] \ddot{\mu} + \left[(1-\phi)\, J\rho^s \frac{\partial \psi^s}{\partial (\phi J)} - p \right] \dot{(\phi J)} \\ & + (1-\phi)\, J\rho^s \left[\frac{\partial \psi^s}{\partial \theta^s} + s^s \right] \dot{\theta}^s + \left[(1-\phi)\, J\rho^s \frac{\partial \psi^s}{\partial \theta^s_{,I}} \right] \dot{\theta}^s_{,I} + \frac{1}{\theta^s} \tilde{q}^s_I \theta^s_{,I} \end{aligned} \quad . \tag{4.34}$$

Following the procedures of Coleman and Noll[103], Equation (4.34) must hold for all admissible processes associated with arbitrary variations of $v_{i,j}$, $\dot{\mu}_{,I}$, $\dot{\mu}$, $\ddot{\mu}$, $\dot{(\phi J)}$, $\dot{\theta}^s$, and $\dot{\theta}^s_{,I}$. The inequality is linear in $v_{i,j}$, $\dot{\mu}_{,I}$, $\ddot{\mu}$, $\dot{(\phi J)}$, $\dot{\theta}^s$, and $\dot{\theta}^s_{,I}$, which implies that the coefficients contracted with these terms must be zero in order for the inequality to hold for all admissible processes, leading to the

following constitutive equations for the solid,

$$\begin{aligned}
(1-\phi)\, P^s_{Ji} &= (1-\phi_0)\, J_0 \rho^s_0 \frac{\partial \psi^s}{\partial F_{iJ}} + \phi J F^{-1}_{Ji} p \\
\tilde{\xi}_I &= (1-\phi_0)\, J_0 \rho^s_0 \frac{\partial \psi^s}{\partial \mu_{,I}} \\
p &= (1-\phi_0)\, J_0 \rho^s_0 \frac{\partial \psi^s}{\partial (\phi J)} \\
s^s &= -\frac{\partial \psi^s}{\partial \theta^s} \\
\frac{\partial \psi^s}{\partial \dot{\mu}} &= \frac{\partial \psi^s}{\partial \theta^s_{,I}} = 0
\end{aligned} \quad . \tag{4.35}$$

Notice that for the reference configuration relationships we have used the fact that $(1-\phi)\rho^s J = (1-\phi_0)\rho^s_0 J_0$ from (4.3), where the subscript "0" refers to the values of the quantities in the reference state. The reduced form of the dissipation inequality for the solid is then,

$$\left[(1-\phi)\, J \rho^s \frac{\partial \psi^s}{\partial \mu} + \tilde{\pi}\right] \dot{\mu} + \frac{1}{\theta^s} \tilde{q}^s_I \theta^s_{,I} \leq 0 \quad . \tag{4.36}$$

This reduced dissipation inequality is satisfied if,

$$\begin{aligned}
\tilde{\pi} &= -\,(1-\phi_0)\, J_0 \rho^s_0 \frac{\partial \psi^s}{\partial \mu} - \beta \dot{\mu} - \eta_I \theta^s_{,I} \\
\tilde{q}^s_I &= -\bar{\eta}_I \dot{\mu} - \kappa^s_{IJ} \theta^s_{,J}
\end{aligned} \quad , \tag{4.37}$$

with the positivity condition,

$$\beta \dot{\mu}^2 + \dot{\mu} \eta_I \theta^s_{,I} + \theta^s_{,I} \bar{\eta}_I \dot{\mu} + \theta^s_{,I} \kappa^s_{IJ} \theta^s_{,J} \geq 0 \quad \forall\ \dot{\mu}, \theta^s_{,I} \quad . \tag{4.38}$$

Each of the newly introduced material properties, β, η_I, $\bar{\eta}_I$, and κ^s_{IJ} are allowed to depend upon $\mu_{,I}$, μ, $\dot{\mu}$, (ϕJ), θ^s, $\theta^s_{,I}$, and F_{iJ}. Note that κ^s_{IJ} is the thermal conductivity tensor for the solid skeleton.

We now consider the fluid. For the fluid, the second law inequality is,

$$\begin{aligned}\frac{D}{Dt}\int_{V_0}\phi\rho^f s^f J dV_0 \geq &-\int_{S_0}\frac{\tilde{q}^f_J N_J}{\theta^f}\,dS_0+\int_{V_0}\frac{\tilde{r}^f+\tilde{r}^{sf}}{\theta^f}dV_0\\ &-\int_{S_0}\rho^f\tilde{w}_J N_J s^f\,dS_0+\int_{V_0}\rho^f\tilde{m}s^f dV_0\end{aligned}\quad . \tag{4.39}$$

Here, the left-hand side of the inequality is the rate of change of the entropy in the fluid, and the right-hand side represents the entropy transfer to the fluid including the entropy of the convected and injected fluid. The Helmholtz free energy for the fluid is,

$$\psi^f = e^f - s^f\theta^f \quad . \tag{4.40}$$

Application of (4.6), (4.30), and (4.40) leads to the pointwise form for the second law inequality for the fluid as,

$$\begin{aligned}\phi J\rho^f\,\overset{\circ}{\psi}{}^f \leq &\phi Jp\frac{\overset{\circ}{\rho}{}^f}{\rho^f}-\phi J\rho^f s^f\,\overset{\circ}{\theta}{}^f+\phi\tilde{\tau}_{Ji}\Big(v_i+v_i^{f/s}\Big)_{,J}\\ &-\phi J\rho^f\left[\tfrac{1}{2}\overset{\circ}{A}\,v_i^{f/s}+A\left(\overset{\circ}{v}{}_i^{f/s}\right)\right]v_i^{f/s}\\ &+\left[p\big(\phi JF^{-1}_{Ji}\big)_{,J}-\tilde{f}_i^{sf}\right]v_i^{f/s}-\frac{1}{\theta^f}\tilde{q}^f_I\theta^f_{,I}\end{aligned}\quad . \tag{4.41}$$

In contrast to the analysis of the second law for the solid, here we do not invoke the principle of equipresence, i.e. that each dependent quantity depends upon each of the independent quantities. Instead, we take a slightly more restrictive set of assumptions for the analysis of (4.41). We assume that the Helmholtz free energy of the fluid ψ^f, the fluid pressure p, and the entropy density of the fluid s^f are dependent only on the density of the fluid ρ^f, the fluid velocity gradient $v^f_{i,J}=v_{i,J}+v^{f/s}_{i,J}$, the temperature of the fluid θ^f, and the temperature

gradient in the fluid $\theta^f_{,I}$. The remaining dependent quantities include the fluid stress $\tilde{\tau}_{Ji}$, the heat flux in the fluid $\tilde{q}^f_I$, and the interaction force between the solid and fluid $\tilde{f}^{sf}_i$, each of which can depend upon ρ^f, θ^f, $\theta^f_{,I}$, ϕ, $v^f_{i,J}$, as well as the relative fluid velocity $v^{f/s}_i$, its rate with respect to the fluid $\left(\overset{\circ}{v}{}^{f/s}_i\right)$, the deformation gradient F_{iJ}, and the phase-field parameter μ. Equation (4.41) then becomes,

$$\begin{aligned} 0 \geq & \phi J \left[\rho^f \frac{\partial \psi^f}{\partial \rho^f} - \frac{p}{\rho^f}\right] \overset{\circ}{\rho}{}^f + \phi J \rho^f \left[\frac{\partial \psi^f}{\partial \theta^f} + s^f\right] \overset{\circ}{\theta}{}^f + \phi J \rho^f \frac{\partial \psi^f}{\partial \theta^f_{,I}} \overset{\circ}{\theta}{}^f_{,I} \\ & + \phi J \rho^f \frac{\partial \psi^f}{\partial v^f_{i,J}} \left(\overset{\circ}{v}{}^f_{i,J}\right) + \phi J \rho^f \left[\tfrac{1}{2} \overset{\circ}{A}\, v^{f/s}_i + A\left(\overset{\circ}{v}{}^{f/s}_i\right)\right] v^{f/s}_i \\ & - \left[p\left(\phi J F^{-1}_{Ji}\right)_{,J} - \tilde{f}^{sf}_i\right] v^{f/s}_i + \frac{1}{\theta^f} \tilde{q}^f_I \theta^f_{,I} - \phi \tilde{\tau}_{Ji} v^f_{i,J} \end{aligned} \quad . \tag{4.42}$$

Equation (4.42) must hold for all admissible processes associated with arbitrary variations of $\overset{\circ}{\rho}{}^f$, $\overset{\circ}{\theta}{}^f$, $\overset{\circ}{\theta}{}^f_{,I}$, $v^f_{i,J}$, $\left(\overset{\circ}{v}{}^f_{i,J}\right)$, $v^{f/s}_i$, and $\left(\overset{\circ}{v}{}^{f/s}_i\right)$. The inequality is linear in $\overset{\circ}{\rho}{}^f$, $\overset{\circ}{\theta}{}^f$, $\left(\overset{\circ}{v}{}^f_{i,J}\right)$, and $\overset{\circ}{\theta}{}^f_{,I}$, which implies that the coefficients contracted with these terms must be zero in order for the inequality to hold for all admissible processes, leading to the constitutive equations for the fluid,

$$\begin{aligned} p &= \left(\rho^f\right)^2 \frac{\partial \psi^f}{\partial \rho^f} \\ s^f &= -\frac{\partial \psi^f}{\partial \theta^s} \\ \frac{\partial \psi^f}{\partial \theta^f_{,I}} &= 0, \quad \frac{\partial \psi^f}{\partial v^f_{i,J}} = 0 \end{aligned} \quad . \tag{4.43}$$

and the reduced dissipation inequality for the fluid,

$$0 \geq \left[\phi J \rho^f \left(\tfrac{1}{2} \overset{\circ}{A} v_i^{f/s} + A \left(\overset{\circ}{v_i^{f/s}} \right) \right) - p\big(\phi J F^{-1}_{Ji}\big)_{,J} + \phi_{,J} \tilde{\tau}_{Ji} + \tilde{f}_i^{sf} \right] v_i^{f/s} \\ - \tilde{\tau}_{Ji} \left(w_{i,J} + \phi v_{i,J} \right) + \frac{1}{\theta^f} \tilde{q}_I^f \theta^f_{,I} \qquad . \tag{4.44}$$

This reduced dissipation inequality for the fluid is satisfied if,

$$\begin{aligned} \tilde{\tau}_{Ji} &= \nu_{iJkL} \left(w_{k,L} + \phi v_{k,L} \right) + \hat{\tau}_{Ji} \\ \tilde{q}_I^f &= -\kappa^f_{IJ} \theta^f_{,J} + \hat{q}_I \\ \tilde{f}_i^{sf} &= p\big(\phi J F^{-1}_{Ji}\big)_{,J} - \phi_{,J} \tilde{\tau}_{Ji} - \chi_{ij} v_i^{f/s} - \phi J \rho^f \left(\tfrac{1}{2} \overset{\circ}{A} v_i^{f/s} - A \left(\overset{\circ}{v_i^{f/s}} \right) \right) + \hat{f}_i^{sf} \end{aligned} \qquad . \tag{4.45}$$

Here we have focused on the direct terms for the deviatoric fluid stress, the fluid heat flux, and the solid/fluid interaction force introducing the positive definite material tensors of the fluid viscosity ν_{iJkL}, the thermal conductivity of the fluid κ^f_{IJ}, and the fluid impermeability of the porous solid χ_{ij}. Each of these material tensors is allowed to depend upon ρ^f, θ^f, $\theta^f_{,I}$, ϕ, $v^f_{i,J}$, $v_i^{f/s}$, $\left(\overset{\circ}{v_i^{f/s}} \right)$, F_{iJ}, and μ. The additional functions $\hat{\tau}_{Ji}$, $\hat{q}_I$, and $\hat{f}_i^{sf}$ are not written out explicitly for the sake of brevity, but their general construction and positivity constraint is analogous to that spelled out for the solid in (4.37) and (4.38). In practice, each of these functions will usually be taken to vanish, as will the cross terms in (4.37).

At this point there remains one quantity that has not been constrained, the heat transferred from the solid to the fluid, $\tilde{r}^{sf} = -\tilde{r}^{fs}$. For this we consider

the second law inequality for the solid/fluid aggregate as a whole,

$$\begin{aligned}
&\frac{D}{Dt}\int_{V_0}\left[(1-\phi)\,\rho^s s^s+\phi\rho^f s^f\right]JdV_0\\
&\quad\geq-\int_{S_0}\left(\frac{\tilde{q}^s_J N_J}{\theta^s}+\frac{\tilde{q}^f_J N_J}{\theta^f}\right)dS_0+\int_{V_0}\left(\frac{\tilde{r}^s+\tilde{r}^{fs}}{\theta^s}+\frac{\tilde{r}^f+\tilde{r}^{sf}}{\theta^f}\right)dV_0\\
&\qquad-\int_{S_0}\rho^f\tilde{w}_J N_J s^f\,dS_0+\int_{V_0}\rho^f\tilde{m}s^f dV_0
\end{aligned}\quad . \tag{4.46}$$

Here, the left-hand side of the inequality is the rate of change of the entropy in the aggregate, and the right-hand side represents the entropy transfer to the aggregate including entropy convected and injected into the aggregate by the fluid. Applying the previously derived constitutive equations, the pointwise form is,

$$\begin{aligned}
0\leq&\frac{1}{\theta^f}\left\{\phi\tilde{\tau}_{Ji}v^f_{i,J}-\phi J\rho^f\left[\tfrac{1}{2}\overset{\circ}{A}\,v_i^{f/s}+A\left(\overset{\circ}{v_i^{f/s}}\right)\right]v_i^{f/s}\right.\\
&\qquad\left.+\left[p\left(J\phi F^{-1}_{Ji}\right)_{,J}-\tilde{f}_i^{sf}\right]v_i^{f/s}-\frac{1}{\theta^f}\tilde{q}^f_I\theta^f_{,I}\right\}\\
&+\frac{1}{\theta^s}\left\{\left[(1-\phi)\,J\rho^s\frac{\partial\psi^s}{\partial\mu}+\tilde{\pi}\right]\dot{\mu}-\frac{1}{\theta^s}\tilde{q}^s_I\theta^s_{,I}\right\}+\frac{\tilde{r}^{sf}\left(\theta^s-\theta^f\right)}{\theta^s\theta^f}
\end{aligned}\quad . \tag{4.47}$$

The two terms in brackets have already appeared in the dissipation inequalities for the fluid (4.44) and solid (4.36) and each is already constrained to be non-negative. Hence, (4.47) still does not offer a clear constraint upon the heat transferred between the solid and fluid. However, a reasonable approach is to take the interpretation that each of the components of (4.47) must satisfy the inequality independently of the others. Then, the third term will satisfy the

inequality if,

$$\tilde{r}^{sf} = \tilde{h}^{sf}\left(\theta^s - \theta^f\right) \quad . \tag{4.48}$$

Here, $\tilde{h}^{sf}$ is an effective heat transfer coefficient for the porous solid/fluid system, which must be positive and can depend upon each of the independent variables associated with the fluid and the solid.

4.2.6 The Solid Free Energy

At this point the model is relatively general and has many material properties that must be specified. In this section a free energy potential is devised that simultaneously models the linear poroelasticity of Biot-type models and the onset and propagation of fluid filled fractures within the medium. Toward this end a "poro-enthalpy" potential Ω^s is proposed that can be derived from the Hemholtz free energy by the following Legendre transformation,

$$\left(1-\phi_0\right) J_0 \rho_0^s \Omega^s = \left(1-\phi_0\right) J_0 \rho_0^s \psi^s - Jp\phi \quad . \tag{4.49}$$

Then, the entropy inequality for the solid (4.33) can be rewritten as,

$$\begin{aligned} \left(1-\phi\right) J\rho^s \dot{\Omega}^s \leq & \left[\left(1-\phi\right) P^s_{Ji} - \phi p J F^{-1}_{Ji}\right] v_{i,J} - \phi J \dot{p} \\ & - \tilde{\pi}\dot{\mu} + \tilde{\xi}_I \dot{\mu}_{,I} - \left(1-\phi\right) J\rho^s s^s \dot{\theta}^s - \frac{1}{\theta^s}\tilde{q}^s_I \theta^s_{,I} \end{aligned} \quad , \tag{4.50}$$

and the constitutive relations outlined by (4.35) and (4.37) can be written in terms of Ω^s as,

$$\begin{aligned}
&(1-\phi)\, P^s_{Ji} = (1-\phi_0)\, J_0 \rho^s_0 \frac{\partial \Omega^s}{\partial F_{iJ}} + \phi p J F^{-1}_{Ji} \\
&\tilde{\xi}_I = (1-\phi_0)\, J_0 \rho^s_0 \frac{\partial \Omega^s}{\partial \mu_{,I}} \\
&\phi J = -\,(1-\phi_0)\, J_0 \rho^s_0 \frac{\partial \Omega^s}{\partial p} \\
&s^s = -\frac{\partial \Omega^s}{\partial \theta^s} \\
&\frac{\partial \Omega^s}{\partial \dot{\mu}} = \frac{\partial \Omega^s}{\partial \theta^s_{,I}} = 0 \\
&\tilde{\pi} = -\,(1-\phi_0)\, J_0 \rho^s_0 \frac{\partial \Omega^s}{\partial \mu} - \beta \dot{\mu} - \eta_I \theta^s_{,I} \\
&\tilde{q}^s_I = -\bar{\eta}_I \dot{\mu} - \kappa^s_{IJ} \theta^s_{,J}
\end{aligned} \quad . \tag{4.51}$$

Consider the following simple poro-enthalpy for reversible, hyperelastic, isothermal behavior,

$$\begin{aligned}
(1-\phi_0)\, J_0 \rho^s_0 \Omega^s =& g_d(\mu)\Omega^+(F_{iJ}) + \Omega^-(F_{iJ}) - \left[\alpha + (1-\alpha)\, g_m(\mu)\right](J-1)\, p \\
&- \left[1 - g_m(\mu)\right] \frac{p^2}{2N} - \phi_0 p + \frac{G_c}{4\ell_0}\left[(1-\mu)^2 + 4\ell_0^2 \mu_{,I}\mu_{,I}\right]
\end{aligned} \quad . \tag{4.52}$$

Here an additive decomposition of the elastic strain-energy $\Omega^{\text{el}} = \Omega^+ + \ \Omega^-$ has been employed so degradation is driven by the presence of tensile deformations. The material constants α, N, and G_c are a coupling coefficient commonly referred to as the Biot coefficient, the Biot tangent modulus, and Griffith's critical energy release rate, respectively, and ϕ_0 is the intrinsic porosity. Note that we invoke the compatibility relations described in Coussy [95] (pp. 79) to relate the Biot coefficient, the intrinsic porosity ϕ_0, and Biot's tangent modulus

such that,

$$\frac{1}{N} = \frac{(\alpha - \phi_0)(1-\alpha)}{K} \quad . \tag{4.53}$$

where K is the bulk modulus of the aggregate.

The last term in (4.52) is ubiquitous to the second order theory for phase-field fracture theories as originally proposed by Francfort and Marigo [6] in their pioneering work on the variational approach to fracture, where ℓ_0 is a nonlinear process zone length scale. The degradation function $g_d(\mu)$ is left in general terms for the sake of simplicity. In practice, the cubic formulation [99] described in Chapter 2 will be used,

$$g_d(\mu) = f_d^c(\mu) = \mu^2 \left[s(\mu - 1) - 2\mu + 3 \right] \quad , \tag{4.54}$$

with $s \ll 1$.

Finally, the form of the function $g_m(\mu)$ in (4.52) is chosen such that $g_m(0) = 1$, $g_m'(0) = 0$, $g_m(1) = 0$, $g_m'(1) = 0$, and $0 \leq g_m(\mu) \leq 1$ in order to cause the porosity to approach unity within open cracks, as will be discussed in more detail shortly. A simple function that satisfies these requirements is,

$$g_m(\mu) \equiv \begin{cases} 1 & ; \quad \mu < 0 \\ 1 - 3\mu^2 + 2\mu^3 & ; \quad 0 \leq \mu \leq 1 \\ 0 & ; \quad \mu > 1 \end{cases} \quad , \tag{4.55}$$

and is adopted in this work. In fact, g_m is simply $1 - g_d(\mu)$ when $s = 0$.

For additional clarity, the constitutive relations of (4.51) can be written

explicitly using the poro-enthalpy potential (4.52), $\beta = 0$, and $\eta_I = 0$ as,

$$\begin{aligned}
&(1-\phi)\, P^s_{Ji} = g_d(\mu)\frac{\partial \Omega^+}{\partial F_{iJ}} + \frac{\partial \Omega^-}{\partial F_{iJ}} + \left[\phi - \alpha - g_m(\mu)\,(1-\alpha)\right] J F^{-1}_{Ji} p \\
&\phi J = \phi_0 + \left[\alpha + g_m(\mu)\,(1-\alpha)\right](J-1) + \left[1 - g_m(\mu)\right]\frac{p}{N} \\
&\tilde{\pi} = -g_d{}'(\mu)\Omega^+(F_{iJ}) + \frac{G_c}{2\ell_0}(1-\mu) + g_m{}'(\mu)\left[(1-\alpha)\,(J-1)\,p - \frac{1}{2N}p^2\right] \\
&\tilde{\xi}_I = 2G_c\ell_0\mu_{,I}
\end{aligned} \quad . \tag{4.56}$$

Using (4.28) the total aggregate stress is,

$$P_{Ji} = g_d(\mu)\frac{\partial \Omega^+}{\partial F_{iJ}} + \frac{\partial \Omega^-}{\partial F_{iJ}} - \left[\alpha + g_m(\mu)\,(1-\alpha)\right] J F^{-1}_{Ji} p + \phi \tilde{\tau}_{Ji} \quad . \tag{4.57}$$

Additionally, the spectral decomposition of the stored strain energy for an isotopic solid as described in the work of Miehe et al.[89] is adopted. The strain energy takes the form,

$$\begin{aligned}
&\Omega^+(\varepsilon_{IJ}) = \frac{\lambda^s}{2}\langle \varepsilon_{KK}\rangle^2 + \mu^s\left(\langle\varepsilon_1\rangle^2 + \langle\varepsilon_2\rangle^2 + \langle\varepsilon_3\rangle^2\right) \\
&\Omega^-(\varepsilon_{IJ}) = -\frac{\lambda^s}{2}\langle -\varepsilon_{KK}\rangle^2 - \mu^s\left(\langle-\varepsilon_1\rangle^2 + \langle-\varepsilon_2\rangle^2 + \langle-\varepsilon_3\rangle^2\right) \quad , \\
&\varepsilon_{IJ} = \frac{1}{2}\left(F_{kI}F_{kJ} - \delta_{IJ}\right)
\end{aligned} \tag{4.58}$$

where λ^s and μ^s are the Lamé material constants, ε_{IJ} is the Green-Lagrangian finite strain measure, and $\varepsilon_{(1,2,3)}$ are the principal strains. If we neglect the (typically small) effects of fluid shear stress and adopt the assumptions of infinitesimal deformations such that $(J-1) \approx \varepsilon_{KK}$ and products of displacement gradients are neglected, the theory recovers linear poroelasticity when the phase-field parameter $\mu = 1$ (and $g_m(\mu = 1) = 0$)[112,118].

On the contrary, if $\mu = 0$ then $g_m(\mu = 0) = 1$ and there are two important features of the model to note. First, in the presence of an opening

strain state, the aggregate stress is $P_{Ji} = -JF^{-1}_{Ji}p$ which corresponds to a Cauchy stress of $\sigma_{ji} = -p\delta_{ij}$. Second, the porosity ϕ satisfies $\phi J = \phi_0 + (J-1)$, which implies that $\phi = \phi_0$ in the absence of deformation (i.e. $J = 1$), and $\phi \to 1$ for large opening deformations as $J \to \infty$. It is tempting here to expect that the porosity ϕ should be equal to 1 where ever a crack exists, or $\mu = 0$, regardless of the deformation. In fact, initial attempts were made to develop the theory on the basis that $\phi = \phi_0 + (1-\mu)(1-\phi_0)$. Due to the diffuse nature of the phase-field, however, cracks required too much fluid mass influx to grow. The nuance lies in the fact that the phase-field μ is actually representing a zero thickness surface in the undeformed configuration. This surface has a finite energy associated with it, which is "smeared" out over the length scale ℓ_0 but should have no volume when undeformed. The volume created by a change in opening of the crack, though, should be identically equal to the deformation at that point, or $\dot{(\phi J)} = \dot{J}$, which is exactly what is recovered in the present theory when $\mu = 0$.

Lastly, the rationale for the constraints on the derivative of $g_m(\mu)$ at the endpoints can be understood by considering the micro-force balance in the absence of phase-field gradients and micro-body forces, i.e. when $\tilde{\pi} = 0$. For such homogeneous cases, if $g'_m(\mu) \neq 0$ at $\mu = 0$ and $\mu = 1$, then the third term in (4.56) can drive the phase-field parameter outside of the range of $0 \leq \mu \leq 1$.

4.2.7 The Fluid Momentum Equation and Free Energy

Generally, as a result of small crack openings, hydraulic fractures are characterized by low Reynolds number flows. In this section the fluid momentum equation (4.16) is reduced under the assumptions of isothermal, creeping Newtonian flow. The goal is to simultaneously describe the Darcy-type flow regimes that occur in fully intact regions of the porous aggregate while also properly representing the laminar flow that is present in crack interiors. To this end, the following constitutive relationships are proposed,

$$\begin{aligned} \tau_{ij} &= g_S(\mu)\nu^f \left[w_{i,j} + w_{j,i} - \tfrac{1}{3}w_{k,k}\delta_{ij} + \phi\left(v_{i,j} + v_{j,i} - \tfrac{1}{3}v_{k,k}\delta_{ij}\right)\right] \\ \tilde{f}_i^{sf} &= p\big(\phi J F_{Ji}^{-1}\big)_{,J} - \phi_{,J}\tilde{\tau}_{Ji} - g_D(\mu)\phi J\frac{\nu^f}{\kappa}w_i \end{aligned} \quad . \tag{4.59}$$

Here ν^f is the fluid viscosity, κ is the isotropic intrinsic permeability for the aggregate, and $g_S(\mu)$ and $g_D(\mu)$ are indicator functions of the phase-field for the Stokes and Darcy flow regimes. The indicator functions are chosen such that,

$$\begin{aligned} g_S(\mu) \to 1 \;\text{ and }\; g_D(\mu) \to 0 \;\text{ as }\; \mu \to 0 \\ g_S(\mu) \to 0 \;\text{ and }\; g_D(\mu) \to 1 \;\text{ as }\; \mu \to 1 \end{aligned} \quad . \tag{4.60}$$

The specific forms chosen are,

$$\begin{aligned} g_S(\mu) &= (1-\mu)^2 \\ g_D(\mu) &= \mu^n \end{aligned} \quad , \tag{4.61}$$

where the Stokes function has been chosen based on its simplicity and ease of implementation and the Darcy function is chosen such that the impermeability (which is typically quite high) is degraded more rapidly in the presence of cracks. The choices made for the indicator functions in (4.61) will be shown

to reproduce the desired behaviors for the numerical experiments conducted, which will be described in the following sections. For the Darcy indicator function $n = 4, 6, 8$ will be compared. Applying (4.59) and (4.61) within (4.16) and neglecting inertial terms based upon the assumption of low Reynolds number creeping flows, the fluid momentum equation becomes,

$$\begin{aligned}\left[g_S(\mu)\nu^f \left(w_{i,j} + w_{j,i} - \tfrac{1}{3}w_{k,k} + \phi\left(v_{i,j} + v_{j,i} - \tfrac{1}{3}v_{k,k}\right)\right) JF^{-1}_{Jj}\right]_{,J} \\ - JF^{-1}_{Ji}p_{,J} - Jg_D(\mu)\frac{\nu^f}{\kappa}w_i = 0\end{aligned} \quad . \tag{4.62}$$

Equation (4.62) is analogous to the Brinkman equation [119] where the material coefficients depend directly on the phase-field parameter μ. When $\mu = 1$ Darcy flow laws are recovered, and when $\mu = 0$ the equations for Stokes flow are recovered.

Additionally, we allow for a compressible fluid and use a linearized relationship between fluid pressure and fluid density to approximate small changes in the fluid density. To this end the following free-energy density for the fluid is proposed,

$$\psi^f = \frac{1}{c^f}\left(\frac{\rho^f_0}{\rho^f} + \ln\left(\rho^f\right)\right) \quad . \tag{4.63}$$

From (4.63) the density pressure relationship becomes,

$$\rho^f = \rho^f_0 + c^f p \quad . \tag{4.64}$$

In the absence of the phase-field micro-force balance laws, and the Stokes flow characterization for fluid flow in cracks, the equations presented above

reduce to the nonlinear poroelastic theories developed by Coussy and co-workers[112–116], which have been shown to be in agreement with Biot's classical theory[118,120,121].

4.3 Numerical Implementation

The numerical experiments presented in the following sections will be for isothermal, isotropic, quasi-static material behavior with steady-state fluid flows. To summarize, the following balance and kinematic equations will enter

into the numerical model:

$$
\begin{aligned}
&P_{Ji,J} + \tilde{b}_i = 0 \quad \text{in } V_0 \\
&P_{Ji} N_J = \tilde{t}_i \quad \text{on } S_t \\
&u_i = \hat{u}_i \quad \text{on } S_u \\
&\\
&F_{iJ} = \delta_{iJ} + u_{i,J} \\
&\\
&\tilde{\xi}_{I,I} + \tilde{\gamma} + \tilde{\pi} = 0 \quad \text{in } V_0 \\
&\tilde{\xi}_I N_I = \tilde{\iota} \quad \text{on } S_\iota \\
&\mu = \hat{\mu} \quad \text{on } S_\mu \\
&\\
&\left(\tau_{ji} J F^{-1}_{Jj}\right)_{,J} - J F^{-1}_{Ji} p_{,J} - J g_D(\mu) \frac{\nu^f}{\kappa} w_i = 0 \quad \text{in } V_0 \\
&\frac{1}{\rho^f}(\phi \dot{\rho^f} J) + \left(J F^{-1}_{Ji} w_i\right)_{,J} + \frac{\rho^f_{,J}}{\rho^f} J F^{-1}_{Ji} w_i - \tilde{m} = 0 \quad \text{in } V_0 \\
&\left(\tau_{ji} - p\delta_{ij}\right) J F^{-1}_{Jj} N_J = \tilde{t}^f_i \quad \text{on } S_f \\
&w_i = \hat{w}_i \quad \text{on } S_w \\
&p = \hat{p} \quad \text{on } S_p
\end{aligned}
\qquad . \qquad (4.65)
$$

Then, the corresponding virtual work statement that will serve as the weak form of these equations for the finite element analysis is,

$$\begin{aligned}
&\int_{V_0} \left[P_{Ji}\delta F_{iJ} + \tilde{\xi}_I \delta\mu_{,I} - \tilde{\pi}\delta\mu \right] dV_0 \\
&\int_{V_0} \left[\left(\tilde{\tau}_{Ji} - pJF^{-1}_{Ji} \right) \delta w_{i,J} + g_D(\mu)\frac{\nu^f}{\kappa} J w_i \delta w_i \right] dV_0 \\
&\int_{V_0} \left[-\left(\frac{1}{\rho^f}(\phi\dot{\rho^f}J) + JF^{-1}_{Ji} w_{i,J} + \frac{\rho^f_{,J}}{\rho^f} JF^{-1}_{Ji} w_i \right) \delta p \right] dV_0 \quad . \qquad (4.66)
\end{aligned}$$

$$\begin{aligned}
&= \int_{V_0} \left(\tilde{b}_i \delta u_i + \tilde{\gamma}\delta\mu - \tilde{m}\delta p \right) dV_0 \\
&\quad + \int_{S_0} \tilde{t}_i \delta u_i dS_0 + \int_{S_0} \tilde{\iota}\delta\mu dS_0 + \int_{S_0} \tilde{t}^f_i \delta w_i dS_0
\end{aligned}$$

For the numerical method the unknown nodal quantities include the displacements of the aggregate u_i, which is simply the difference between the material point positions in the current and reference configurations, the relative flux of the fluid with respect to the solid w_i, the fluid pressure p, and the phase-field parameter μ. The stresses, P_{Ji} and $\tilde{\tau}_{Ji}$, internal micro-forces $\tilde{\xi}_I$ and $\tilde{\pi}$, porosity ϕ, and fluid density ρ^f are determined constitutively from (4.56)-(4.59) and (4.64). We note that the derivations of the governing equations constructed in the previous sections were done so in the reference configuration, which is the domain on which the numerical calculations are performed. The importance in distinguishing between the reference configuration and the current configuration lies in a proper representation of the fluid mass and momentum balances, particularly in regions with degradation. However, for the brittle, linearly elastic materials addressed in this work there is no real advantage in distinguishing

the Green-Lagrange strain and its linearized small strain measure. This is due to the fact that the geologically relevant structures investigated in this work undergo relatively small displacements and deformations. In order to simplify the implementation, we believe it is suitable to adopt this small deformation approximation within the stress and micro-force constitutive equations.

In terms of the numerical discretization, standard continuous Galerkin finite element methods are sufficient for the solution of the aggregate equilibrium and micro-force balance equations. Hence, bilinear quadrilateral elements are used to solve these equations. However, for the fluid flow equations it is well-known that the elements must satisfy the LBB conditions[122–124]. For the two-dimensional numerical investigations described here we have used Taylor-Hood elements[125] with biquadratic interpolations for the relative flux w_i, and bilinear interpolations for the fluid pressure p. The evolution equation that appears in the fluid mass balance is solved using an implicit backward Euler approximation. The fully coupled equations are nonlinear and standard Newton-Raphson procedures are implemented to solve for all quantities of interests simultaneously. This is in contrast with many other phase-field approaches where staggered schemes are used to solve for specific quantities while all other fields are held fixed[95]. For matrix inversion, a parallel, sparse, direct solver from the MUMPS package for the PETSc library is used to solve the problems that are discussed in the next section[126–129].

4.4 Results and Discussion

This section presents a series of benchmark solutions that the theory must, at a minimum, recover in order to properly model the hydraulic fracture process. Many of these simple solutions are readily recovered if the crack surfaces are identified explicitly by a discrete crack method, but are not trivial for diffuse crack descriptions like the phase-field approach to fracture. The comparison of the model with these foundational problems for which analytical solutions have been developed serves to establish confidence in the theory for when more complex problems are investigated. The three most fundamental problems that are addressed in this paper are the steady, laminar flow through parallel crack faces, the fluid-loading of a free surface as in Terzaghi's consolidation problem, and the uniform pressurization of a plane-strain center crack in an isotropic, impermeable, elastic, infinite solid. After agreement is established for these three fundamental problems, an investigation of the Kristianovic-Geerstma-de Klerk problem (a plane strain center crack in an impermeable, elastic, infinite domain subject to a constant point injection at the center of the crack) is carried out. Finally, a problem that includes multiple cracks interacting and merging is presented to demonstrate the advantageous features of the phase-field method.

4.4.1 Laminar Flow between Fixed Parallel Plates

A proper representation of the fluid flow field through the system is needed to produce the correct pressure field. This pressure then drives the

solution for the deformation of the aggregate and the evolution of the phase-field within the system. We note that there are also shear stresses within the fluid, but that the influence of fluid shear stress on the aggregate is small. Without a correct representation of the fluid flow, particularly within cracks, an accurate description of crack evolution would be hopeless. Sub-surface cracks are characterized by two long length scales, the crack height and crack length, and one small length scale, the width/opening or crack aperture. Thus, the fluid flow inside the crack is well approximated by the flow between two fixed parallel plates such that the crack walls make up the two plates. Because of the relatively small openings of cracks in these sub-surface materials, the flow is laminar. Assuming the fluid is a Newtonian fluid, the solution to the Navier-Stokes equations for this simplified geometry yields a parabolic flow profile where the total fluid flux through a cross-section per unit crack height is

$$q_y = -\frac{(W_n)^3}{12\ \nu^f} p_{,y} \quad . \tag{4.67}$$

The result is proportional to the pressure gradient, $p_{,y}$ along the length direction of the crack y (see the inset of Figure 4.2), and dependent on the cube of the crack opening aperture $W_n = \Delta u_n$. Thus, it is crucial that the crack opening displacement is properly incorporated into the theory. Due to the fact that the cracks are represented by a diffuse field, Δu_n is not a readily available local quantity for phase-field methods. In order to address this issue, the present theory utilizes a finite deformation framework such that the effects of the crack opening are accounted for in the solution of the fluid flow balances,

which are naturally dependent on the deformation within cracks.

There is, however, an additional issue that arises for the present theory when numerical discretizations are implemented. As shown in Figure 4.1 and discussed in Chapter 2 the analytic solution to the phase-field theory for fracture has a jump discontinuity in displacement. As previously mentioned, standard Galerkin methods are used to discretize the displacement field u_i, which forces the resulting field to be C^0 continuous. Thus, the opening in the discretized setting occurs over some discretization length scale associated with the element size, as shown in the figure.

For the discretized case the crack opening width can be estimated as,

$$W_n^h \approx h^e \left(1 + e_n\right) \quad , \tag{4.68}$$

where e_n is the nominal strain of a line element perpendicular to the crack plane and h^e is the length scale associated with the discretization. It can be shown that the total crack opening displacement is approximated properly by the discretized method[93] (i.e. $h^e e_n^h = \Delta u_n^h \approx \Delta u_n$), but, according to (4.68), the actual crack opening width will be over estimated. In order to account for this discrepancy our approach is to use a scaled viscosity defined as,

$$\nu_s^f = \nu^f \left(\frac{1 + e_n}{e_n}\right)^3 = \nu^f \left(\frac{\lambda_n}{\lambda_n - 1}\right)^3 \quad , \tag{4.69}$$

where λ_n is the stretch ratio of a line element perpendicular to the crack plane and can be determined using the deformation gradient F_{iJ} with gradients of

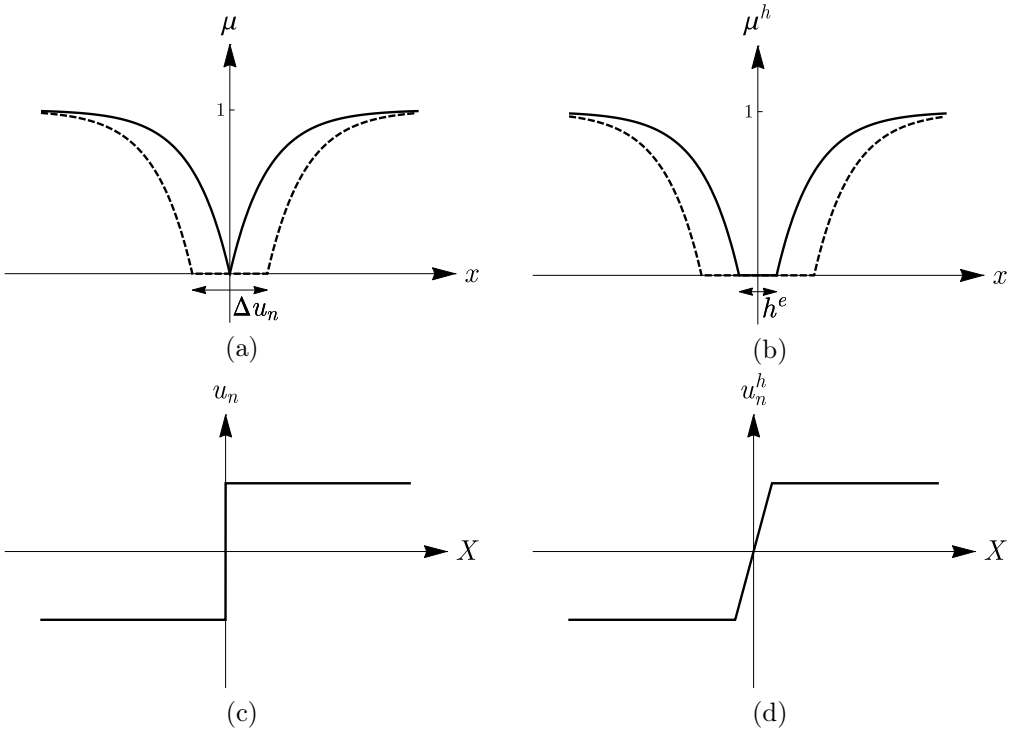

Figure 4.1: These plots illustrate the difference between the analytical and discretized representations of the material stretch normal to a phase-field crack. (a) shows the phase-field profile before deformation (solid line) and after opening (dotted line) in the deformed configuration for the analytical case. (b) shows the phase-field profile before deformation (solid line) and after opening (dotted line) in the deformed configuration for the discretized case. (c) and (d) show the crack opening displacement as a function of location in the reference configuration for the analytical and discretized cases respectively. h^e is a characteristic length scale associated with the discretization (i.e. element size).

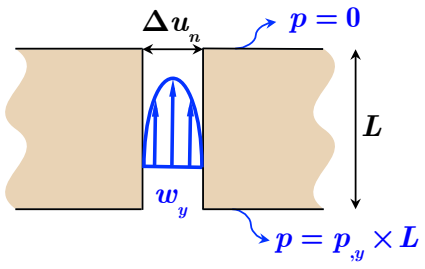

(a)

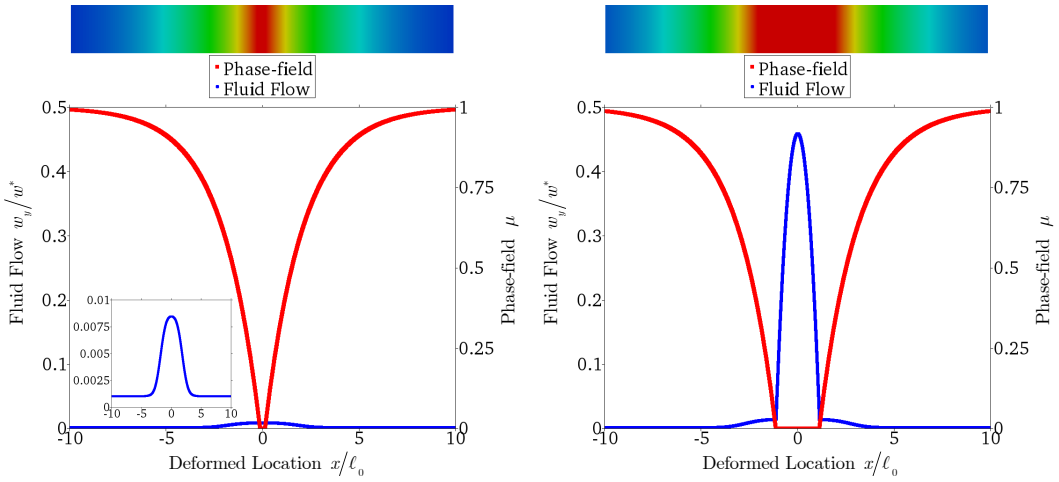

(b) (c)

Figure 4.2: These simulations demonstrate the ability of the theory to accurately represent the flow through cracks of different openings. A pressure differential is applied between the top and bottom surfaces. The contour plot above shows the phase-field damage profile, which in the undeformed configuration (not shown) is identical for both the open and closed crack. The solutions for the fluid flow in the vertical direction w_y are shown with blue lines for the case of a closed (a) and open (b) diffuse crack. The color contours and red lines indicate the phase-field parameter in the deformed configuration. When the crack is nearly closed (a) there is only enhanced Darcy-like flow (blue line) in the damaged region, as can be seen in the included insert. However, when the crack opens (b) the proper channel flow (blue line) within the crack is recovered such that the net fluid flux is in agreement with laminar flow through fixed parallel plates. The fluid flows (blue line) are normalized by $w^* = -\frac{p_{,y}\ell_0^2}{\nu^f}$.

the phase-field as,

$$\lambda_n = F_{iJ} n_i N_J = F_{iJ} \frac{\mu_{,i}\mu_{,J}}{\sqrt{\mu_{,k}\mu_{,k}}\sqrt{\mu_{,L}\mu_{,L}}} = \sqrt{\frac{\mu_{,K}\mu_{,K}}{F^{-1}_{Ik} F^{-1}_{Jk} \mu_{,I}\mu_{,J}}} \quad . \tag{4.70}$$

Equation (4.68) is derived based on the objective to obtain equality in flux for two channels of different initial widths, $h^{(1)}$ and $h^{(2)}$, each subjected to the same opening displacement, $\Delta u_n^{h(1)} = \Delta u_n^{h(2)}$, and the same gradient of pressure. Then using (4.67), this implies that,

$$q_y^{(1)} = -\frac{\left(W_n^{h(1)}\right)^3}{12\ \nu^f_{(1)}} p_{,y} = -\frac{\left(W_n^{h(2)}\right)^3}{12\ \nu^f_{(2)}} p_{,y} = q_y^{(2)} \quad , \tag{4.71}$$

where $W_n^{h(1,2)} = h^{(1,2)}\left(1 + e_n^{(1,2)}\right)$ as described above. The average nominal strains over the width of each channel are $e_n^{(1)}$ and $e_n^{(2)}$. Since the crack opening displacement for each channel is taken to be equivalent then,

$$\Delta u_n^{h(1)} = \Delta u_n^{h(2)} \quad \Rightarrow \quad e_n^{(1)} h^{(1)} = e_n^{(2)} h^{(2)} \quad . \tag{4.72}$$

Substituting this into (4.71) and algebraic manipulation gives,

$$\frac{\left(\frac{h^{(1)}}{h^{(2)}} + e_n^{(2)}\right)^3 \left(h^{(2)}\right)^3}{\nu^f_{(1)}} = \frac{\left(1 + e_n^{(2)}\right)^3 \left(h^{(2)}\right)^3}{\nu^f_{(2)}} \quad . \tag{4.73}$$

Then, if $h^{(1)}$ is taken to represent the idealized case where the initial crack width is zero and $h^{(2)}$ is taken to be the element size in the finite element mesh equation (4.69) is recovered.

Equation (4.70) is the same measure as that described in Miehe[94]. A simpler approach that does not require the determination of the direction

normal to the crack is to utilize the Jacobian of the deformation gradient, which is a reasonable approximation for the normal stretch in highly damaged elements, i.e. $\lambda_n \approx J$. Another potential issue with the scaling (4.68) is that if the stretch is equal to unity or less, the scaled viscosity will approach infinity or become negative. If the phase-field parameter μ is not equal to one in these regions, or the Stokes indicator function $g_S(\mu) > 0$, the scaling as presently proposed will cause issues in the solution of the fluid momentum balance (4.62). For instance, as seen in Figure 4.1 the stretch is localized to the region of maximum damage, and regions just outside the localization of deformation where the phase-field is still transitioning but the stretch may be unity or less are be subject to the issues described. To address this we restrict the scaling at a value as to not overwhelm Darcy's law. Effectively, a critical stretch λ_c is chosen such that if $\lambda_n < \lambda_c$ the scaling acts as if the crack did not exist and Darcy-like behavior is approximately recovered. The critical stretch is chosen to be $\lambda_c = 1 + 2\sqrt{G_c/E\ell_0}$ which corresponds to roughly 5 times the strain level[8] associated with the material peak stress during homogeneous uniaxial straining. Thus, the scaling is chosen such that,

$$\nu_s^f = \nu^f \times \min\left(\left(\frac{\lambda_n}{\langle \lambda_n - 1\rangle}\right)^3,\ \left(\frac{\lambda_c}{\lambda_c - 1}\right)^3\right) \quad . \tag{4.74}$$

Note that it is advantageous to numerical computations based on Newton-Raphson type schemes to have smooth tangent stiffness components. Thus, convergence results for the coupled N-R scheme can be improved by adopting a smooth rendition of the viscosity scaling outlined by (4.74). A smooth piece-

wise scaling function based on λ_c can be defined as,

$$F_\nu(\lambda_n) \equiv \begin{cases} \left(\dfrac{\lambda_c}{\lambda_c - 1}\right)^3 & ; \quad \lambda_n \leq 1 \\ \left(\dfrac{\lambda_n(\lambda_n - 2) + (1 - 2\lambda_c)^2}{5 + \lambda_n(\lambda_n - 2) + 4\lambda_c(\lambda_c - 2)}\right)^3 & ; \quad 1 \leq \lambda_n \leq 2\lambda_c - 1 \\ \left(\dfrac{\lambda_n}{\lambda_n - 1}\right)^3 & ; \quad \lambda_n \geq 2\lambda_c - 1 \end{cases} \tag{4.75}$$

such that a smooth rendition of (4.74) is $\nu_s^f = \nu^f F_\nu(\lambda_n)$.

Figure 4.2 demonstrates how the flow profile evolves for a given pressure gradient with a large versus a small crack opening. A crack is imposed by setting $\mu = 0$ for a line of elements through the thickness of a thin strip of material. A pressure drop is imposed in the vertical direction and fluid flows through the strip. The flow evolves according to the opening imposed on the crack, starting as an enhanced Darcy-type flow in the region of damage and transitioning to a full Stokes-type flow.

Figure 4.3 illustrates how well the dependence on crack opening is captured with and without the viscosity scaling for various element sizes. The total flux through a strip of length $200\ell_0$ is calculated. The volumetric flow rate is normalized by $q* = -p_{,y}\ell_0^3/\nu^f$ in the plot. The results clearly demonstrate that if the scaling is not used, accuracy cannot be expected unless the crack opening displacement divided by the mesh size, $\Delta u_n^h/h^e$, is well above unity. The solutions for the scaled viscosity deviate slightly from the result for strictly Darcy flow as a result of the enhanced Darcy zone that can be observed in Figure 4.2. This is a result of the damage in the neighborhood of

the crack and the Darcy degradation function (4.61).

A remarkable feature of the viscosity scaling is that there is no explicit dependence on a length scale associated with the discretization. This is in stark contrast with other approaches that utilize the phase-field method to model the hydraulic fracture problem, see [94,95]. The approach adopted in these other models is to use Reynolds lubrication theory directly, i.e. (4.67), by solving the Darcy equation but modifying the permeability based on the crack opening displacement. For instance in Miehe et al. (2015) [94] the approach requires that the stretch normal to the crack plane be multiplied by the square of a length scale associated with the numerical discretization. A similar approach is also used in Mikelic et al. (2015) [95].

4.4.2 Performance of the Viscosity Scaling for Arbitrarily Oriented Cracks

The Brinkman type equation (4.62), is capable of reproducing Reynold's lubrication theory as described in the previous section. This result is critical for the proper modeling of the flow within the crack. The studies conducted in Section 4.4.1 utilized a uniform mesh with the major axis of the fracture aligned with the structured grid. The results shown in Figures 4.2 and 4.3 are characterized by two features of the numerical solution: 1) The deformation within the crack localizes at the element level as discussed earlier and portrayed in Figure 4.1. Since quadrilateral bi-linear (Q1) elements were utilized for the displacements the resulting Jacobian of deformation in the cracked elements

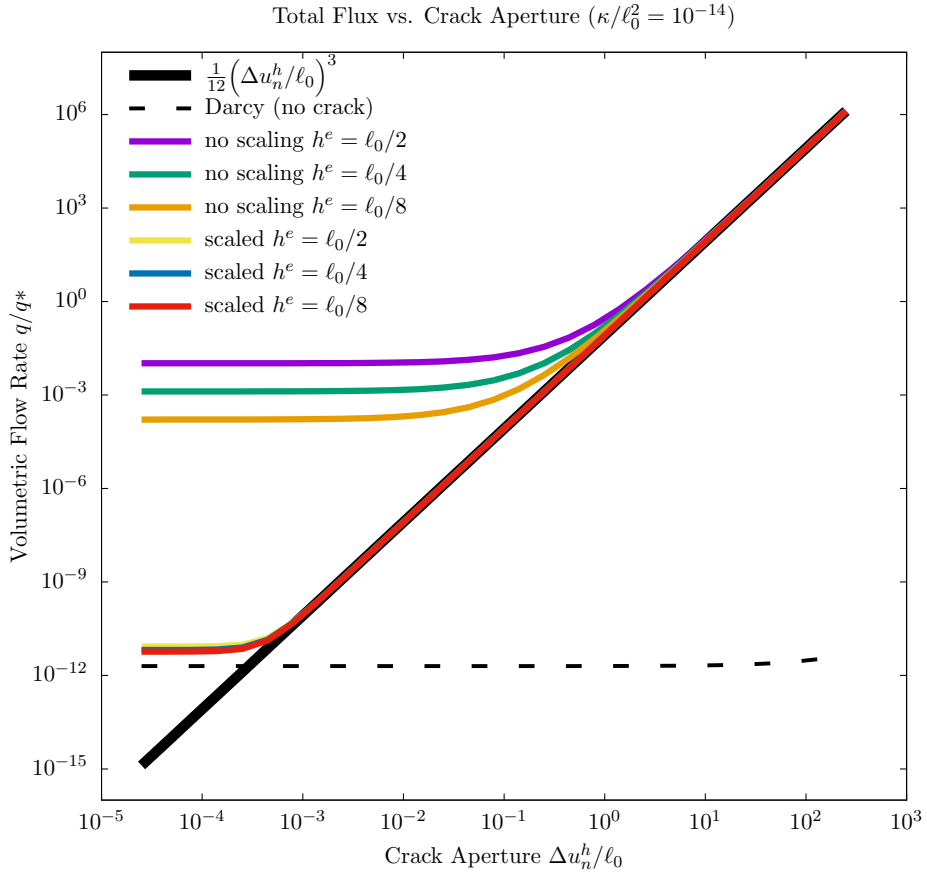

Figure 4.3: This plot shows the dependence of the fluid flux on crack opening for the flow through a cracked strip of permeable material. The initial length of the strip is $200\ell_0$ and the middle-most element is completely degraded as in Figure 4.1b. The solid black line corresponds to the analytical solution of flow between two fixed, discrete parallel plates (4.67). The purple, green, and orange lines correspond to cases where the fluid viscosity is not scaled for different element sizes. The red, yellow and blue lines correspond to the scaling (4.74) for various element sizes. The scaling results in excellent agreement with the analytical calculation for crack apertures of practical interest. The damage zone about the crack leads to an enhanced Darcy-type behavior for situations where the crack is essentially closed. This explains the slight discrepancy between the scaled solutions and the Darcy solution (dotted line) where no crack (i.e. no damage) is present. Without the scaling, accurate solutions cannot be expected until the normalized crack aperture is on the order of the mesh size.

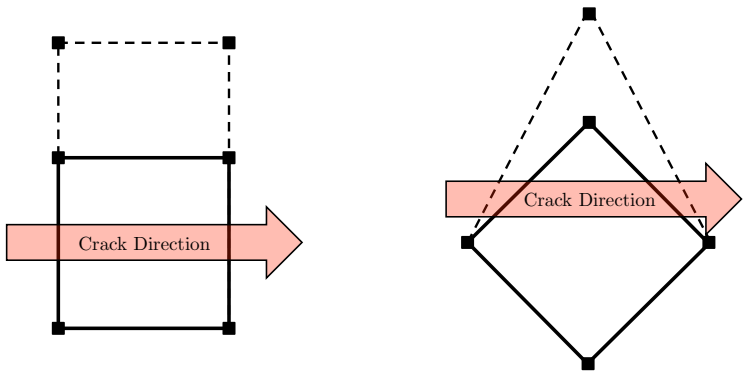

(a) (b)

Figure 4.4: Representative elements and element deformations. (a) Crack direction is aligned with element orientation. The Jacobian of the deformation gradient is constant. (b) Crack direction is not aligned with element orientation. The Jacobian of the deformation gradient is not uniform for this element.

is constant. 2) The average fluid velocity w_i is discretized using 9-noded biquadratic quadrilateral elements (Q2) and, hence the parabolic profile of flow within an element can be represented exactly.

In contrast, when the orientation of the crack does not align with the underlying mesh, the characteristics listed above are not true in general. The deformation within the crack still localizes at the element level; however, the resulting Jacobian is not necessarily constant for the Q1 element. In addition, the parabolic flow profile is not attainable for an element with an arbitrary orientation with respect to the direction along the crack length. Figure 4.4 illustrates two distinct types of element-wise deformation for the Q1 element.

The consequence of these responses is that the lubrication theory result

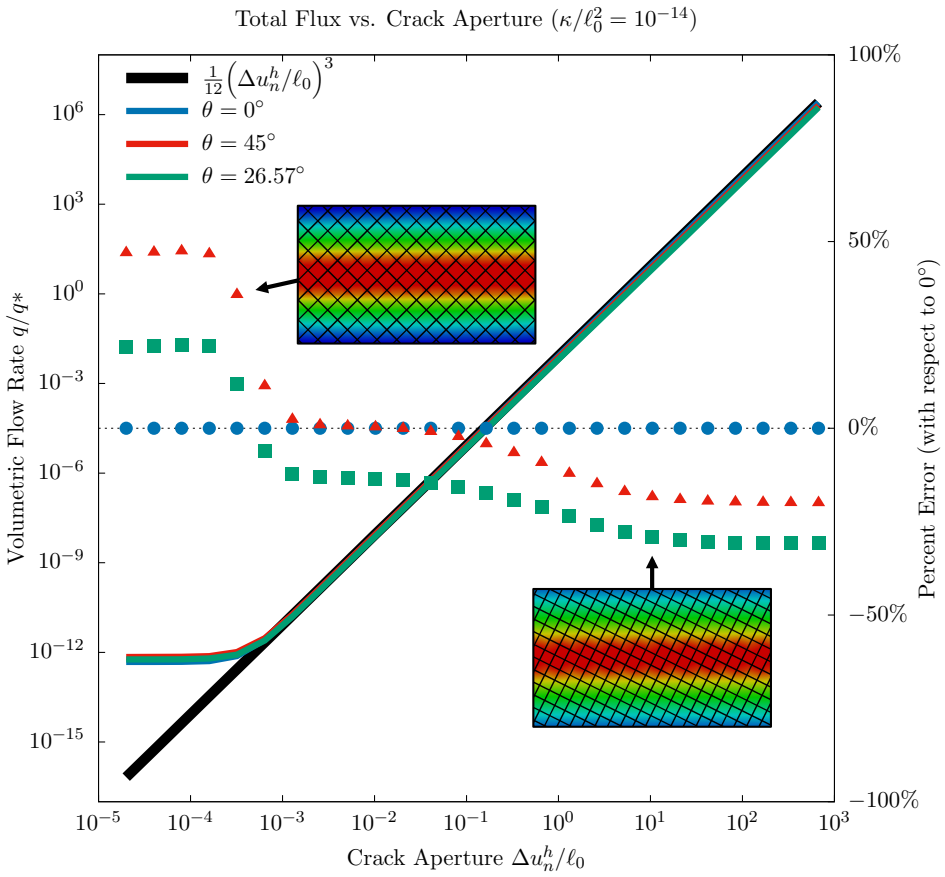

Figure 4.5: This figure shows the revisited results of Figure 3 for cases where the underlying numerical mesh is not oriented in the direction of the crack. The red lines show the results where the element is rotated 45° clock-wise with respect to the crack. The green lines show the results where the element is rotated 26.57° clock-wise with respect to the crack. The blue lines represent a mesh that is oriented in the same direction as the crack. The coefficients in (4.76) were chosen to minimizes the error for the 45° case for reasonable deformations. In both cases, the error is significantly larger for stretches approaching unity and higher. This is a consequence of element distortion. It is important to note that even though some error is introduced by the rotated elements, the overall cubic dependence on crack aperture is maintained.

of Stokes' equation is not exactly reproduced in these cases and this leads to some solution inaccuracy associated with the mesh orientation dependence. The resulting error may be reduced if an effective element-wise Jacobian is chosen and used in the viscosity scaling equation (4.74). It may be chosen as follows,

$$J^{ele} = 0.7 \times \text{avg}[J]_{ele} + 0.3 \times \max[J]_{ele} \quad , \tag{4.76}$$

where the first term indicates the average Jacobian in a given element and the second term indicates the maximum Jacobian in the element, which will always occur at an element corner for the Q1 element. The coefficients were determined empirically based on an element oriented at 45° with respect to the direction of the crack. Clearly the exact point-wise Jacobian is recovered for deformations where the Jacobian is uniform. The calculations performed in Section 4.4.1, specifically those illustrated in Figure 4.3, were performed again for 2 different meshes where the majority of elements were oriented at 45° and 26.57° respectively. The results of those calculations and the meshes themselves are shown in Figure 4.5. As can be clearly seen, the presence of elements that are not aligned with the crack gives rise to some error, especially when the deformations are large and the elements become distorted. That being said, the problems studied in this work undergo openings in the range of $\Delta u_n^h/\ell_0 \approx 10^{-3} - 10^{-1}$ corresponding to errors with respect to Reynolds lubrication theory of nearly zero for the 0° orientation, 4% for the 45° orientation, and 15% for the 26.57° orientation within this range of relative openings. Note that even though error is introduced for these discretizations, the cubic

dependence of flux on crack aperture is generally maintained.

4.4.3 Fluid Loading of a Surface and Consolidation

Perhaps the most classical problem in poromechanics is Terzaghi's consolidation problem[118]. A rock or soil layer of thickness L rests on a rigid impermeable base and is subject to a constant applied traction $t_y = -p_0$ on the top surface. The more relevant case for pressurized fractures is the case when the applied load is the consequence of the surface being in contact with a fluid at pressure p_0. For this class of uniaxial strain problems the governing equations for displacement and fluid pressure according to Biot theory can be decoupled. For constant loading, Biot theory reduces to Terzaghi's consolidation theory, which gives a homogenous diffusion equation with constant coefficients for the evolution of the fluid pressure field. Thus, the one-dimensional initial-boundary value problem for fluid pressure can be written as,

$$\begin{aligned}
&\frac{\partial p}{\partial t} - c\frac{\partial^2 p}{\partial x^2} = 0 && x \in [0, L],\ t \geq 0 \\
&p = p_0 && x = 0\ ,\ t \geq 0 \\
&\frac{\partial p}{\partial x} = 0 && x = L\ ,\ t \geq 0 \\
&p = \frac{(\nu_u - \nu)}{\alpha\,(1-2\nu)\,(1-\nu_u)} p_0 && x \in (0, L],\ t = 0^+
\end{aligned} \quad . \tag{4.77}$$

$$c = \frac{2\kappa\mu^s\,(1-\nu)\,(\nu_u - \nu)}{\nu^f \alpha^2 (1-2\nu)^2\,(1-\nu_u)}$$

Here no distinction is made between the current and reference configurations. The resulting pressure field can be integrated to yield the displacement u_x (see

Detournay[118]). The diffusivity coefficient, c, is dependent on the intrinsic permeability, κ, the fluid viscosity, ν^f, the shear modulus of the aggregate, μ^s, the Biot coefficient, α, and the Poisson's ratio of the drained and undrained aggregate, ν and ν_u. Following Detournay[118] and Coussy[95] the undrained Poisson ratio ν_u may be determined in terms of the our model parameters as,

$$\nu_u = \frac{3\nu\phi_0\left(c^f K - 1\right) + \alpha^2\left(1-2\nu\right) + 3\alpha\nu\left(1+\phi_0\right)}{3\phi_0\left(c^f K - 1\right) - \alpha^2\left(1-2\nu\right) + 3\alpha\left(1+\phi_0\right)} \quad , \tag{4.78}$$

where we use $c^f = 1/K^f$ and K^f is the bulk modulus of the fluid.

Note that the use of the symbol ν for Poisson's ratios and for viscosity is unfortunate, but is pointed out here to emphasize the distinction. The pore pressure field at the instant of loading corresponds to the homogeneous undrained response (i.e. if the material were loaded but fluid was not allowed to enter or leave the system). The reason that this problem is relevant to the phase-field fracture model is that the diffuse phase-field crack surface should act as a permeable boundary. In other words, the solution to (4.65) subject to the following boundary conditions,

$$\begin{aligned} \mu &= 0 \quad X \leq 0\,, t \geq 0 \\ p &= p_0 \quad X \leq 0\,, t \geq 0 \\ w_x &= 0 \quad X = L\,, t \geq 0 \\ u_x &= 0 \quad X = L\,, t \geq 0 \end{aligned} \quad , \tag{4.79}$$

should approximate the solution to (4.77) for $0 \leq X \leq L$ and $t \leq 0$. Note that in (4.79) the tractions on the crack surface are not specified. Figure 4.6 shows the results of calculations when the surface is identified explicitly and

when the surface is modeled with the phase-field and compares them with the exact solution provided by Detournay[118]. The bulk modulus and fluid compressibility are chosen such that the undrained Poisson ratio is $\nu_u = 0.26$. The other relevant material parameters are taken as $\alpha = 0.45$, $\nu = 0.22$, and $L = 200\ell_0$. On the left plot is the displacement u_x of the surface at $X = 0$ normalized by the initial instantaneous settlement for $t = 0^+$,

$$u^* = \frac{p_0 L\,(1+\nu)\,(1-2\nu_u)}{3K\,(1-2\nu)\,(1-\nu_u)} \quad , \tag{4.80}$$

and on the right plot is the fluid pressure p/p_0 at the impermeable boundary at $X = L$ as each quantity varies over the dimensionless time $\tau = (ct/4L^2)$.

The results demonstrate excellent agreement between Biot theory, mixture theory, and the phase-field method developed herein. The only slight discrepancy that can be noticed is that the settlement of the layer at early times is slightly greater for the phase-field formulation. This is due to the fact that the permeability of the aggregate is increased in regions of degradation, and thus, fluid diffusion happens more quickly near the boundary. This behavior only affects the fields in a boundary layer on the order of the fracture surface length scale ℓ_0. In other words, the pressure response far away from the surface is unchanged.

4.4.4 Pressurized Cracks

The third verification of the model acts to demonstrate that the theory is capable of properly describing the critical pressure loading levels at which

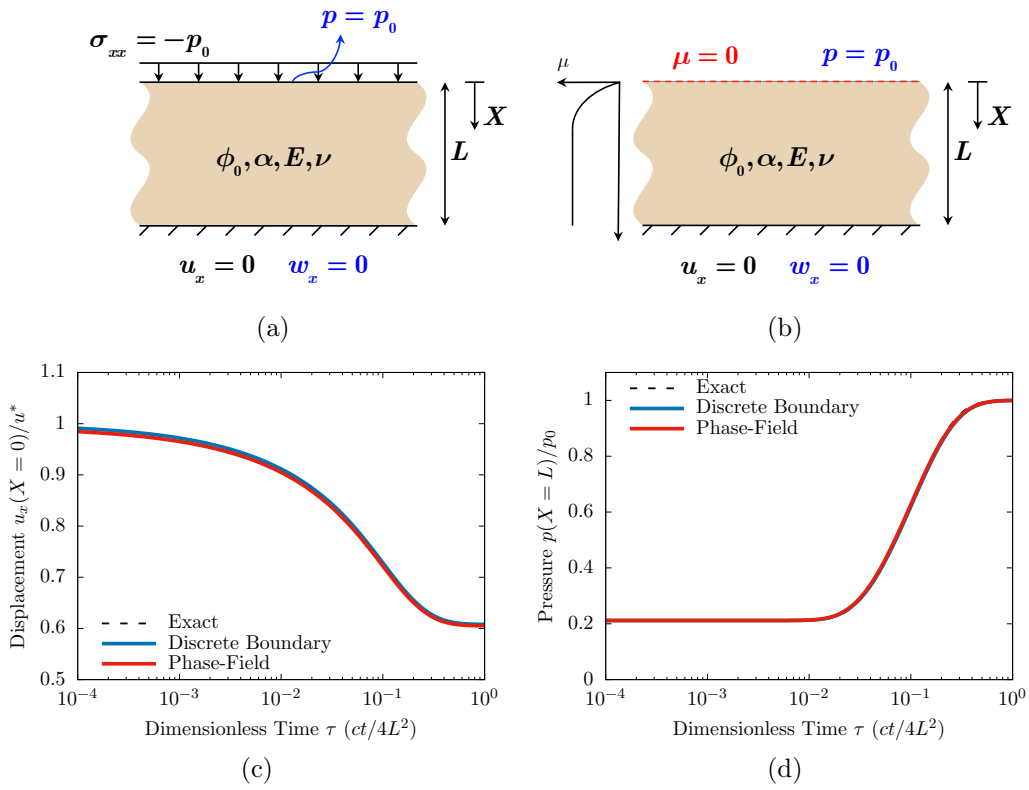

Figure 4.6: These plots show the comparison of the phase-field approach(b) to analytical solutions(a) for the time-dependent poroelastic consolidation process. The pore fluid is incompressible. A normal traction is applied to the left boundary or surface ($X = 0$) at time $t = 0^+$ and the surface displacement(c) and pore pressure at the right boundary ($X = L$)(d) are plotted as functions of time. Note that for the phase-field description the left boundary is not a true boundary, but rather is represented by a damaged phase-field. In other words, this can be thought of as the right half of a symmetric pressurized crack. The plots demonstrate excellent agreement with the discrete and analytical solutions to the problem. For these simulations the mesh size is $h^e = \ell_0/4$.

cracks within the system should grow. As seen in the previous section, pressurized fluid induces tractions on the crack faces and acts to open up the fractures. The cracks should experience the proper deformation and must propagate at the appropriate critical conditions. To demonstrate that the theory does indeed recover the aforementioned phenomena, a plane-strain center crack in an infinite, isotropic, impermeable, elastic medium is analyzed. If the crack is subject to a uniform pressure then this problem lends itself to a simple linear elastic fracture mechanics solution with which comparisons can be made. The propagation of the crack for fixed pressure conditions is unstable, so the modeling approach is to set a crack at a desired length by imposing that the phase-field be zero along the desired length of elements. Then, the entire system is subject to a uniform pressure that is increased until the crack begins to propagate. The infinite domain is represented with high fidelity by using a Dirichlet-to-Neumann map[130,131] on the outermost boundary of the circular finite element mesh. By conducting the study for various imposed crack lengths, the theory can be verified against the linear elastic fracture mechanics solution. According to linear elastic fracture mechanics, the relationship between the critical pressure and the crack length is,

$$\frac{p_c}{\sigma_0} = \sqrt{\frac{\ell_0}{\pi a}} \quad , \tag{4.81}$$

where a is the crack half-length and $\sigma_0 = \sqrt{E' G_c / \ell_0}$.

Figure 4.7 shows the results of these calculations. As expected, the phase-field theory reproduces the LEFM result with remarkable accuracy with

the exception of when the crack length is short with respect to the length scale ℓ_0. This is to be expected given that the assumption of a small-scale process zone is no longer valid. The length scale ℓ_0 can be shown to be directly analogous to the process zone size from cohesive zone descriptions of cracks like the Dugdale-Barenblatt model as described in Chapter 2. As such, discrepancies arise for short cracks where the process zone length scale becomes significant in relation to the crack length a and this represents a deviation from a regime where linear elastic fracture mechanics is applicable.

4.4.5 The Kristianovic-Geerstma-de Klerk Problem

Now we discuss the apparently simple problem of a plane strain hydraulic fracture in an impermeable, elastic, infinite domain subject to the constant rate injection of an incompressible, Newtonian fluid. This geometry is typically termed the KGD fracture geometry after Kristianovic, Geerstma, and de Klerk[53,132]. In the last two decades, a group of researchers lead by E. Detournay has revisited this problem, as well as a few other simple geometries like the penny-shaped crack, and conducted state-of-the-art analytical and numerical studies[57–59,133]. A concise summary of their results for impermeable rocks can be found in Detournay[57]. A particularly notable result in these works is the introduction of a dimensionless parameter comparing the material fracture toughness to the fluid viscosity,

$$\mathcal{K} = 4K_{\mathrm{Ic}}\Big(3\pi^2 E'^3 Q\nu^f\Big)^{-1/4} \quad . \tag{4.82}$$

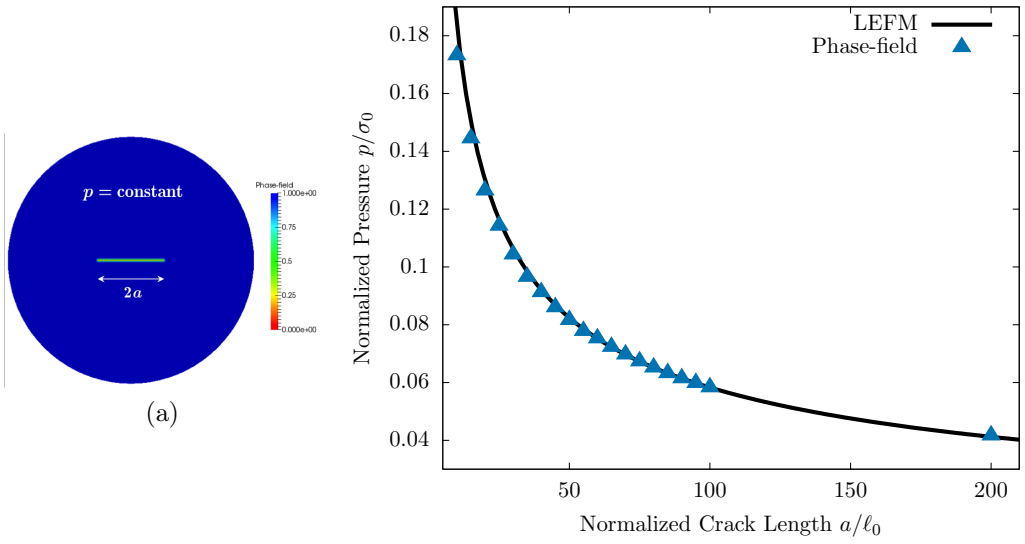

Figure 4.7: This plot is a comparison of the phase-field method to the linear elastic fracture mechanics solution for the critical pressure values for propagation of a plane-strain center crack embedded in an infinite medium. For the phase-field method a crack of given length is designated with Dirichlet boundary conditions and the pressure is increased for the entire mesh until the crack begins to grow unstably. The infinite medium is modeled with a Dirichlet-to-Neumann mapping on the boundary elements of a circular mesh. The phase-field method proposed in this work is in excellent agreement with classical linear elastic fracture mechanics predictions. For these simulations a graded mesh is used with the mesh size in the vicinity of the crack being $h^e = \ell_0/5$, Poisson ratio $\nu = 0.25$ and $\sqrt{G_c/E\ell_0} = 0.001$.

This dimensionless toughness can be used to delineate the dominating regime of fracture propagation for the KGD crack, toughness versus viscosity-dominated propagation. Based on the assumption that the crack aperture is very small in the systems of interest and inertial terms may be neglected, the hydraulic fracture problem involves two mechanisms of dissipation that drive the fracture propagation process. In the toughness-dominated regime, where $\mathcal{K} \to \infty$, the energy dissipated by the flow of viscous fluid is small compared to the energy that is dissipated at the crack tip through the creation of new fracture surfaces. In the viscosity-dominated regime, where $\mathcal{K} \to 0$, the energy dissipated by the flow of viscous fluid is far greater than the dissipation due to the creation of new fracture surfaces. In fact, a primary conclusion of Detournay (2004)[57] is that when $\mathcal{K} < 1$ the solution can be accurately approximated by a limit solution constructed on the assumption that the rock has zero toughness, and when $\mathcal{K} > 4$ the solution may be approximated by a limit solution constructed on the assumption that the injected fluid has zero viscosity.

Since no assumptions related to the viscosity or toughness have been made in the construction of this phase-field theory, the model should be able to capture both limiting regimes, as well as the transition between them. Figure 4.8 contains plots of the injection pressure, crack opening at the injection site, and crack length results for a plane-strain crack subjected to a constant injection rate for $\mathcal{K} = 54.63$ (toughness-dominated (a)-(c)) and $\mathcal{K} = 0.9714$ (viscosity-dominated (d)-(f)). A small initial crack of half-length $a = 5\ell_0$ is embedded in an infinite domain (again using a Dirichlet-to-Neumann map on

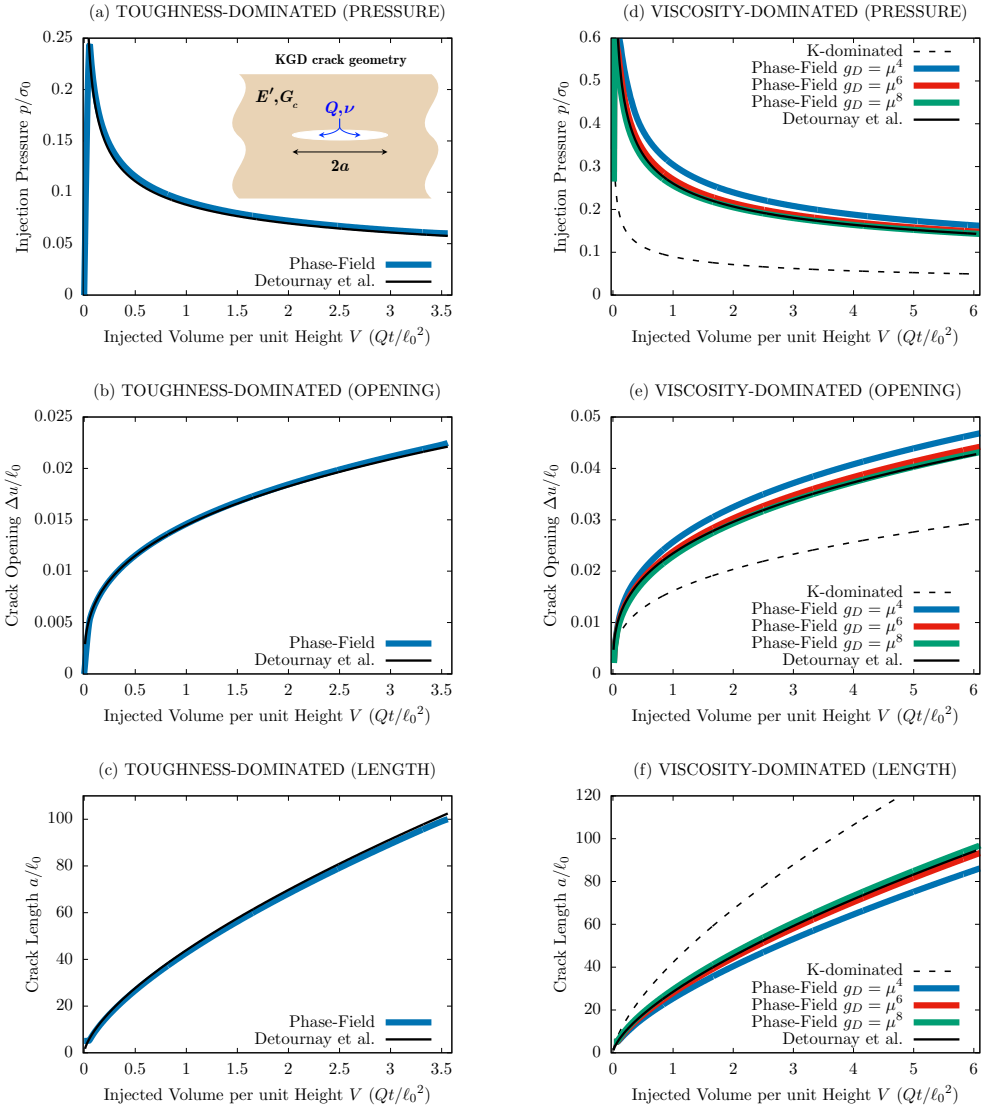

Figure 4.8: Phase-field simulation comparisons to the solutions from Ref.[57] for the 2D KGD crack configuration. (a-c) show results for the toughness-dominated regime $\mathcal{K} = 54.63$, and (d-f) for the viscosity-dominated regime $\mathcal{K} = 0.9714$ for various choices of the Darcy degradation function g_D. Note that models assuming inviscid fluid behavior cannot capture the viscosity dominated regime and would predict behaviors associated with the dashed lines in (d-f). A graded mesh is used with $h^e = \ell_0/5$ in the vicinity of the crack, Poisson's ratio $\nu = 0.25$, $\sqrt{G_c/E\ell_0} = 0.001$, $\ell_0^2/\kappa = 10^{12}$, $(\nu^f Q)/(\sigma_0 \ell_0^3) = 8 \times 10^{-16}$ for (a-c), and $(\nu^f Q)/(\sigma_0 \ell_0^3) = 8 \times 10^{-9}$ for (d-f).

the outer boundary to model the infinite domain) and the crack is subjected to a constant injection rate $\tilde{m}$ at its center. The normal flux of fluid on the outer boundary of the phase-field modeled region is enforced to be zero. For slow enough injection rates, the process resides in the toughness-dominated regime and for high rates of injection, the crack propagates in the viscosity-dominated regime. In each case the functional forms for $g_D(\mu) = \mu^4$, μ^6, and μ^8 were studied. For the toughness-dominated regime the results are effectively independent of $g_D(\mu)$ and the curves for each case are indiscernible. The function $g_D(\mu)$ does play a role in the viscosity-dominated regime as illustrated in Figure 4.8. In general, the results are in very good agreement with the limit solutions developed and outlined by Detournay[57]. The slight discrepancies may be explained by the fact that the location of the crack tip is "blurred" since there is a Dugdale-Barrenblatt type of process zone that exists near the tip region in the phase-field model.

The toughness-dominated regime is characterized by uniform pressure in the crack, and thus, the results in this regime correlate to the results where a uniform pressure is imposed for the whole domain. On the other hand, the viscosity-dominated regime is characterized by a non-uniform pressure distribution along the length of the crack. Dotted lines on the viscosity-dominated regime plot illustrate how the crack would behave for the prescribed injection rate if the assumption of uniform pressure were adopted. The difference highlights the necessity of properly modeling the flow within the crack and, in particular, its dependence on crack opening.

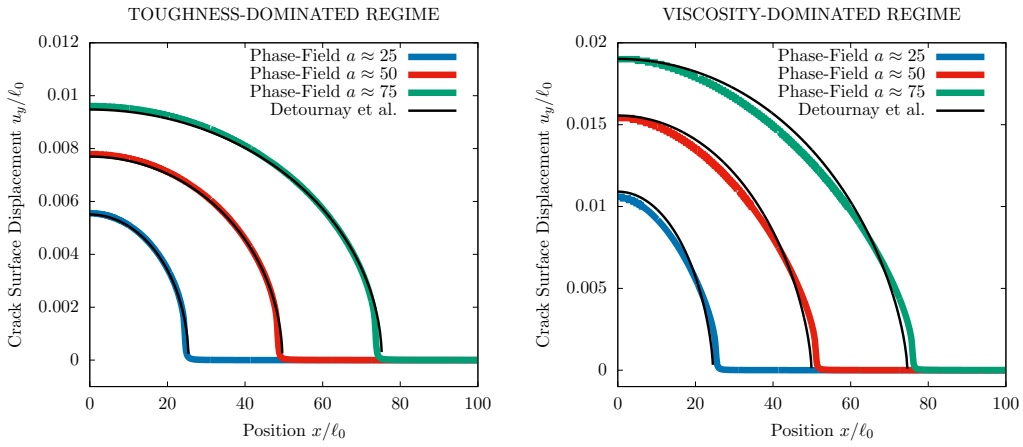

(a) (b)

Figure 4.9: These plots show comparisons of the phase-field simulation to the solutions from Ref.[57] for the crack opening profile of the 2D KGD crack configuration. (a) Shows results for three different time steps for a case when fracture toughness is the dominant dissipative mechanism $\mathcal{K} = 54.63$. (b) Shows results for three different time steps for a case when fluid viscosity is the dominant dissipative mechanism $\mathcal{K} = 0.9714$. The Darcy degradation function $g_D(\mu) = \mu^8$ was used for these calculations.

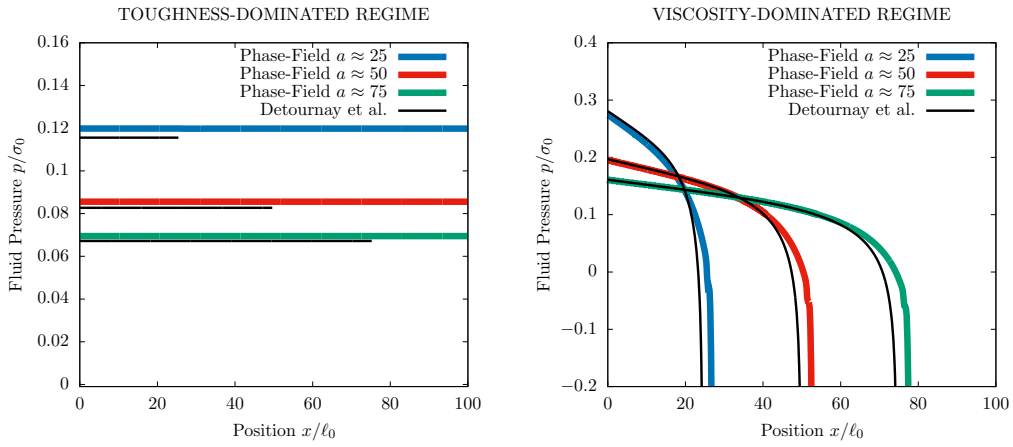

(a) (b)

Figure 4.10: These plots show comparisons of the phase-field simulation to the solutions from Ref.[57] for the crack pressure profile of the 2D KGD crack configuration. (a) Shows results for three different time steps for a case when fracture toughness is the dominant dissipative mechanism $\mathcal{K} = 54.63$. (b) Shows results for three different time steps for a case when fluid viscosity is the dominant dissipative mechanism $\mathcal{K} = 0.9714$. The Darcy degradation function $g_D(\mu) = \mu^8$ was used for these calculations.

Figures 4.9 and 4.10 illustrate the comparison between the phase-field calculations and the analytical solution for crack opening and fluid pressure respectively. As with the other quantities characterizing the process in Figure 4.8, these plots demonstrate reasonable agreement between the phase-field model and the analytical solutions for the crack opening profiles as a function of time. As previously mentioned, the analytic solutions used for comparison correspond to the limit solutions which contain a singularity in pressure for the viscosity dominated case. Much like the K-field solution discussed in Chapter 2 the phase-field model is not capable of reproducing the singularity.

4.4.6 Multiple Crack Interaction

Here, for illustrative purposes, we show results of a calculation where fluid is injected into a small center crack (half-length $a = 10\ell_0$) that then propagates and merges with two "natural" outer cracks. The overall domain is a rectangle with dimensions of $160\ell_0 \times 80\ell_0$. The surface normal displacements and surface normal fluid flux on the outer boundaries are zero. After merging, fluid fills the natural cracks and they begin to propagate from each end in a deflected direction. Contour plots describing the fluid pressure and crack geometry are shown for four different time steps in Figure 4.11. For this simulation the Biot coefficient is $\alpha = 0.45$, and the initial porosity is $\phi_0 = 0.1$. As in the consolidation solution, an increase in pore pressure is observed in the undamaged material surrounding the crack. Figure 4.12 shows the injection pressure as a function of fluid volume injected into the middle crack.

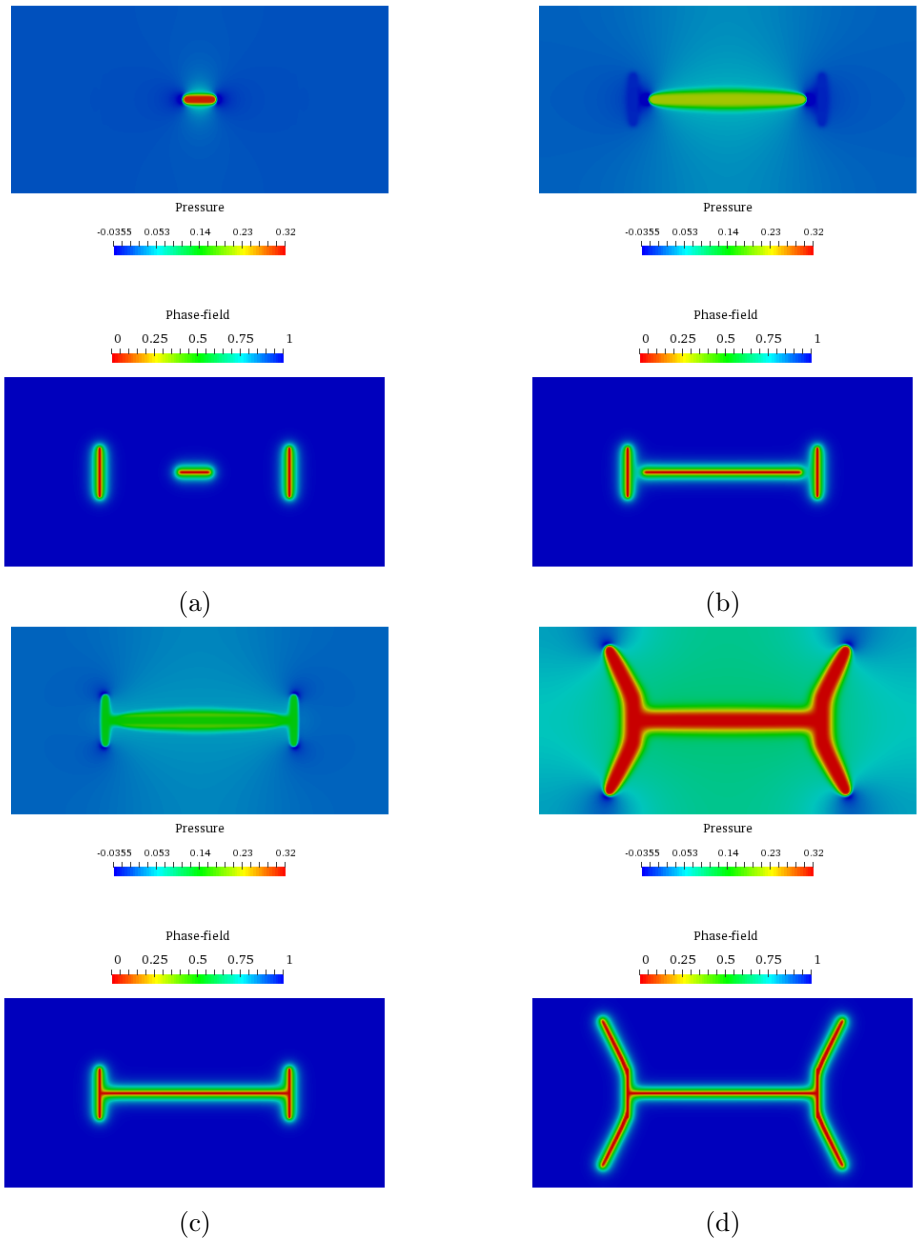

Figure 4.11: A merging crack simulation with injection of fluid into the middle crack at a constant rate. Solutions for the fluid pressure and phase-field fracture parameter are shown for four different time steps, (a)$V/\ell_0^3 = 0.1$, (b)$V/\ell_0^3 = 0.85$, (c)$V/\ell_0^3 = 0.9$, and (d)$V/\ell_0^3 = 3.5$. A uniform mesh with $h^e = \ell_0/2$ is used, Poisson's ratio $\nu = 0.25$, $\sqrt{G_c/E\ell_0} = 0.001$, $\ell_0^2/\kappa = 10^{14}$, $\alpha = 0.45$, $\phi_0 = 0.1$, $c^f/\rho_0^f = 0.01364$, and $(\nu^f Q)/(\sigma_0 \ell_0^3) = 5 \times 10^{-12}$.

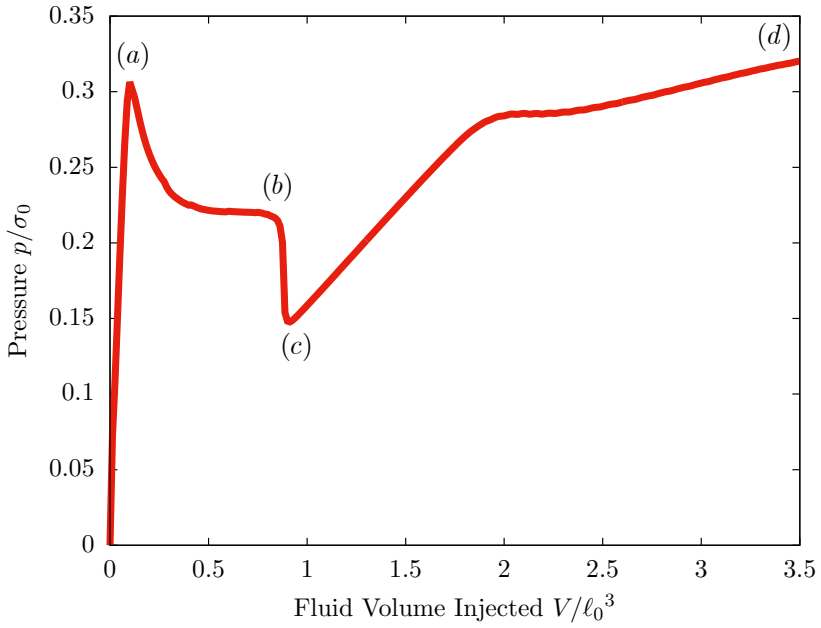

Figure 4.12: A plot of the injection pressure versus the volume of fluid injected into the middle crack. The dip in pressure corresponds to the moment that the middle crack merges with the outer cracks. Labels are included that correspond to the snap shots in Figure 4.11.

The merging of the three cracks corresponds with a drop in the injection pressure as it takes time for the natural cracks to completely open and fill with fluid. Although it is not necessarily geologically relevant in its simplicity, this simulation provides an example of the capabilities of the modeling approach to capture complex behaviors such as crack merging and non-planar propagation.

Another interesting calculation that exhibits the model capabilities is the simultaneous propagation of several parallel cracks. In the simulation shown in Figure 4.13 two or three cracks of initial length $10\ell_0$ are generated

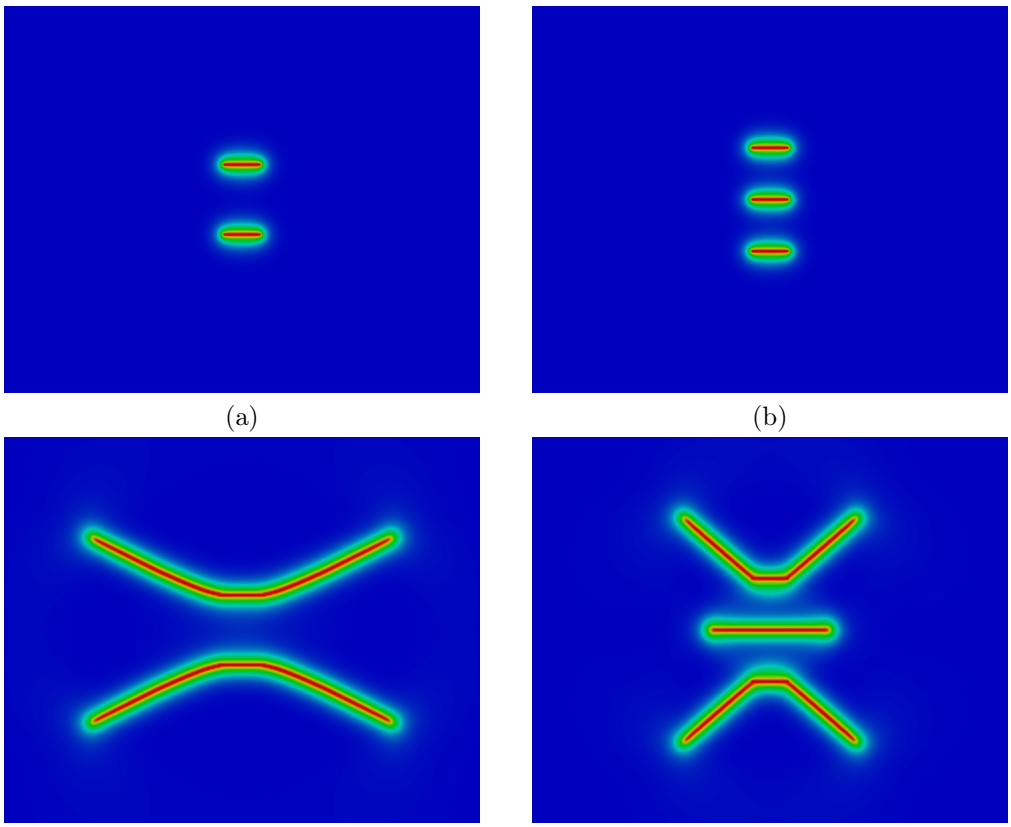

Figure 4.13: Simultaneous injection of multiple parallel cracks. (a,c) Two cracks with an initial spacing of $20\ell_0$. (b,d) Three cracks with an initial spacing of $15\ell_0$. The initial length of each crack is $10\ell_0$.

in a large block of material ($2000\ell_0 \times 2000\ell_0$). The spacing between the cracks is $20\ell_0$ for the two cracks and $15\ell_0$ for the three cracks. Then, each crack is subjected to an equal constant rate of fluid injection. The presence of the multiple cracks have a "stress shadow" effect on one another and, as a result, the cracks tend to propagate in a direction away each other. In the case where three cracks are present the propagation of the middle crack is stunted by the presence of the cracks on the outside. A good understanding of these interactions is important as simultaneous injection of multiple fractures from horizontal wells is becoming common practice in the petroleum industry. The propagation of these cracks is also heavily influenced by the insitu stress state in the rock, which could easily be implemented in the model as force boundary conditions. A clear advantage of the approach is that no additional degrees of freedom are needed as the number of initial fractures is increased, as long as there is sufficient mesh resolution in the vicinity of the added fractures.

Chapter 5

Summary and Future Directions

The advantages of the variational approach to modeling fracture have been well established in the decades since the inception of the approach. The main contribution of this work is the extension of the model to the fracture of piezoelectric ceramics and the fluid driven fracture of poroelastic solids. The general construction of the phase-field approach to fracture was reviewed and a framework that utilizes fundamental balance laws and thermodynamic analyses was introduced. This framework allows for the systematic development of constitutive relationships from a single free energy functional governing all the physics in the solid. All that is left is to choose the form of the free energy such that the appropriate crack face boundary conditions are reproduced.

An analysis of the crack tip behavior of the phase-field model was conducted for the purely mechanical case. The results suggest that the model behaves in a similar fashion to a cohesive zone model, where the process zone is proportional to the phase-field regularization parameter ℓ_0. The model was compared to the somewhat simplistic Dugdale-Bareblatt model which assumes constant cohesive tractions at the crack tip. Potential future investigations could include comparisons of the model with more sophisticated cohesive zone

laws. Also, direct extraction the traction separation relationship from the phase-field solution could be possible, but is not trivial due to the non-locality of the crack opening displacement.

Next, a phase-field model was introduced to capture the quasi-static propagation of cracks in piezoelectric ceramics for four distinct crack-face boundary condition approaches. Both a small deformation linear kinematics framework and a finite deformation framework were developed to describe linear piezoelectric response. Another degradation function was introduced to address undesired consequences of the classic quadratic function when extended to include electro-mechanical coupling. A number of numerical simulations were presented that detail, separately, the onset of crack-closing tractions in the presence of electrical field when the energetically consistent crack-face boundary conditions are adopted, the contrasting influence of applied electric fields when each of the different crack-face boundary conditions are implemented, and the influence of applied electric field on resulting fracture geometries.

As mentioned above, a strength of this phase-field approach is that all of the physics, including the evolution of new surfaces created by fracture, are contained within a single free-energy functional. Thus, all fracture phenomena, including growth, turning, and branching naturally result from the solution of the governing balance laws with the constitutive relations at hand. This is particularly useful in a piezoelectric setting, where the behaviors of a crack are highly dependent on the electro-mechanical coupling within the material

and the boundary conditions that are assumed to exist on the crack faces. As illustrated by[41], the formulation can be extended to ferroelastic materials in which the electro-mechanical coupling becomes even more complex. In contrast, approaches that identify explicit fracture surfaces require constitutive rules for crack growth, turning, branching, and initiation. Additionally, numerical procedures (element splitting, basis enrichment, etc.) are required to administer each of these rules, which can become unwieldy especially in three dimensions. The phase-field approach obviates the need for any such rules or special numerical procedures other than perhaps adaptive mesh refinement, which can also be of use for these other approaches. It should be recognized that the phase-field approach implicitly enforces a crack growth criterion based upon a critical total energy release rate. For piezoelectric and ferroelectric materials such a condition is necessary for crack growth, but it is not necessarily sufficient. A decisive set of experiments that is able to account for the effects of ferroelectric switching and electrical discharge or drift across the crack gap that can clearly identify a fundamental crack growth criterion has yet to be devised and performed for such materials. Hence, the predictive capabilities of the present form of the phase-field approach is limited by the physical veracity of the mode-independent critical energy release rate crack growth criterion. If a valid mode-dependent crack growth criterion is established then such behavior can be included within the phase-field modeling approach via either a mode-dependent degradation function, or a mode-dependent fracture energy.

Lastly, this work has outlined the development of a phase-field model

for describing the fracturing of a fluid-saturated porous continuum. The governing equations were again derived in a general framework through the means of fundamental balance laws and Coleman-Noll thermodynamic analysis type procedures. In addition, specific constitutive equations were provided to recover Biot theory in the bulk and incompressible Stokes flow inside cracks. The numerical implementation of these equations was briefly described and several simple solutions were analyzed to verify the expected behavior of the model. With the help of a finite-deformation framework for the governing equations and a mesh-independent viscosity scaling approach, the theory was shown to recover the proper dependence of fluid flow on crack opening displacement when aligned with the underlying mesh.

One short coming of the current model, however, is that some error is induced in the flow calculations when cracks propagate at angles oblique to the mesh. Some tentative investigations have been conducted on implementing more sophisticated discretization schemes to mitigate the error. An attractive option is the divergence-free B-spline discretizations developed by Evans and Hughes[134]. These basis functions possess the added advantage that mass balance for the Darcy-Brinkman-Stokes equations is satisfied exactly, as opposed to the satisfaction in the weak sense in the current approach. It's anticipated that the smoothness of the basis will diminish the ill-effects associated with oblique crack propagation. The difficulty here lies in the fact that the Jacobian of the deformation is not constant in the crack if higher-order basis function are used. The scaling developed in Chapter 4 utilizes the fact that the Jaco-

bian is constant, and the derivation of a scaling for more general cases proves to be cumbersome (see Appendix C).

The current model was also verified against simple problems in consolidation theory and linear elastic fracture mechanics. Then, the significantly more complex problem of a plane-strain crack subject to uniform fluid injection was investigated. The model was shown to compare favorably to the asymptotic solutions developed by Detournay et al.[57] for both situations where fracture toughness is the dominant dissipation mechanism and where fluid viscous drag is the dominant dissipation mechanism. Successfully representing both regimes without introducing any regime-dependent constitutive relationships demonstrates the robustness of the modeling approach. Lastly, a couple of model problems that demonstrate the true advantages of a phase-field approach to fracture were described. Crack interactions that resulted in crack path deflection and merging were observed. These phenomena were shown to have a significant impact on fluid injection pressure response. With the confidence established by the favorable comparison to simple analytical solutions, it has been shown that the phase-field model for fracture can be a powerful tool in understanding many of the more complex behaviors that occur in multi-physics problems.

Appendices

Appendix A

Energy Transformations

Here we demonstrate the transformations between energy functions for piezoelectricity. Consider a Helmholtz free energy for conducting crack-face boundary conditions of the form,

$$\psi = \bar{\psi}(\underbrace{f\varepsilon_{ij}}_{\bar{\varepsilon}_{ij}}, \underbrace{fD_i}_{\bar{D}_i}) + \psi^{\mu}(\mu, \mu_{,i}) \tag{A.1}$$

$$\sigma_{ij} = f\frac{\partial\bar{\psi}}{\partial(f\varepsilon_{ij})}, \quad E_i = f\frac{\partial\bar{\psi}}{\partial(fD_i)},$$
$$\eta = f'\varepsilon_{ij}\frac{\partial\bar{\psi}}{\partial(f\varepsilon_{ij})} + f'D_i\frac{\partial\bar{\psi}}{\partial(fD_i)} + \frac{\partial\psi^{\mu}}{\partial\mu}, \quad \xi_i = \frac{\partial\psi^{\mu}}{\partial\mu_{,i}}$$

Next, consider a full Legendre transformation on the electrical and mechanical terms to define the Gibbs free energy as,

$$g = \psi - \sigma_{ij}\varepsilon_{ij} - E_iD_i \tag{A.2}$$

The variation of the Gibbs free energy is,

$$\begin{aligned}
\delta g &= \delta\psi - \sigma_{ij}\delta\varepsilon_{ij} - \varepsilon_{ij}\delta\sigma_{ij} - E_i\delta D_i - D_i\delta E_i \\
&= \frac{\partial\bar{\psi}}{\partial(f\varepsilon_{ij})}\left(f'\varepsilon_{ij}\delta\mu + f\delta\varepsilon_{ij}\right) \\
&\quad + \frac{\partial\bar{\psi}}{\partial(fD_i)}\left(f'D_i\delta\mu + f\delta D_i\right) + \frac{\partial\psi^\mu}{\partial\mu}\delta\mu + \frac{\partial\psi^\mu}{\partial\mu_{,i}}\delta\mu_{,i} \\
&\quad - \sigma_{ij}\delta\varepsilon_{ij} - \varepsilon_{ij}\delta\sigma_{ij} - E_i\delta D_i - D_i\delta E_i \\
&= -\varepsilon_{ij}\delta\sigma_{ij} - D_i\delta E_i + \frac{\partial\psi^\mu}{\partial\mu_{,i}}\delta\mu_{,i} + \left[f'\varepsilon_{ij}\frac{\partial\bar{\psi}}{\partial(f\varepsilon_{ij})} + f'D_i\frac{\partial\bar{\psi}}{\partial(fD_i)} + \frac{\partial\psi^\mu}{\partial\mu}\right]\delta\mu \\
&= -\varepsilon_{ij}\delta\sigma_{ij} - D_i\delta E_i + \frac{\partial\psi^\mu}{\partial\mu_{,i}}\delta\mu_{,i} + \left[\frac{f'}{f}\varepsilon_{ij}\sigma_{ij} + \frac{f'}{f}D_iE_i + \frac{\partial\psi^\mu}{\partial\mu}\right]\delta\mu
\end{aligned} \tag{A.3}$$

Next, assume the Gibbs free energy can be written in the form,

$$g = \bar{g}(\underbrace{\sigma_{ij}/f}_{\bar{\sigma}_{ij}}, \underbrace{E_i/f}_{\bar{E}_i}) + g^\mu(\mu, \mu_{,i}) \tag{A.4}$$

Now, the variation of the Gibbs free energy is written as,

$$\begin{aligned}
\delta g &= \frac{\partial\bar{g}}{\partial(\sigma_{ij}/f)}(\delta\sigma_{ij}/f - \delta\mu f'\sigma_{ij}/f^2) \\
&\quad + \frac{\partial\bar{g}}{\partial(E_i/f)}(\delta E_i/f - \delta\mu f'E_i/f^2) + \frac{\partial g^\mu}{\partial\mu}\delta\mu + \frac{\partial g^\mu}{\partial\mu_{,i}}\delta\mu_{,i} \\
&= \frac{1}{f}\frac{\partial\bar{g}}{\partial(\sigma_{ij}/f)}\delta\sigma_{ij} + \frac{1}{f}\frac{\partial\bar{g}}{\partial(E_i/f)}\delta E_i + \frac{\partial g^\mu}{\partial\mu_{,i}}\delta\mu_{,i} \\
&\quad - \left[\frac{f'}{f^2}\frac{\partial\bar{g}}{\partial(\sigma_{ij}/f)}\sigma_{ij} + \frac{f'}{f^2}\frac{\partial\bar{g}}{\partial(E_i/f)}E_i - \frac{\partial g^\mu}{\partial\mu}\right]\delta\mu
\end{aligned} \tag{A.5}$$

However, enforcing the equality of the two forms of δg for arbitrary variations of the stress and electric field yields,

$$\begin{aligned}
\delta\sigma_{ij}, \delta E_i \text{ arbitrary} \rightarrow \varepsilon_{ij} &= -\frac{1}{f}\frac{\partial\bar{g}}{\partial(\sigma_{ij}/f)} \\
D_i &= -\frac{1}{f}\frac{\partial\bar{g}}{\partial(E_i/f)}
\end{aligned} \tag{A.6}$$

This allows us to write a reduced form for δg as,

$$\begin{aligned}\delta g &= -\varepsilon_{ij}\delta\sigma_{ij} - D_i\delta E_i + \left[\frac{f'}{f}\varepsilon_{ij}\sigma_{ij} + \frac{f'}{f}D_iE_i + \frac{\partial\psi^\mu}{\partial\mu}\right]\delta\mu + \frac{\partial\psi^\mu}{\partial\mu_{,i}}\delta\mu_{,i} \\ &= \frac{\partial g^\mu}{\partial\mu}\delta\mu + \frac{\partial g^\mu}{\partial\mu_{,i}}\delta\mu_{,i}\end{aligned} \tag{A.7}$$

Finally, this reduced equality must hold for arbitrary variations of $\delta\mu$ and $\delta\mu_{,i}$ yielding,

$$\delta\mu, \delta\mu_{,i} \text{ arbitrary} \rightarrow \frac{\partial\psi^\mu}{\partial\mu} = \frac{\partial g^\mu}{\partial\mu}, \quad \frac{\partial\psi^\mu}{\partial\mu_{,i}} = \frac{\partial g^\mu}{\partial\mu_{,i}} \tag{A.8}$$

The final set of relationships can be collected in the following forms.

$$\begin{aligned}&\frac{\partial\psi^\mu}{\partial\mu} = \frac{\partial g^\mu}{\partial\mu}, \quad \frac{\partial\psi^\mu}{\partial\mu_{,i}} = \frac{\partial g^\mu}{\partial\mu_{,i}} \\ &\sigma_{ij}/f = \frac{\partial\bar{\psi}}{\partial(f\varepsilon_{ij})} = \bar{\sigma}_{ij}(\bar{\varepsilon}_{ij}, \bar{D}_i) \\ &E_i/f = \frac{\partial\bar{\psi}}{\partial(fD_i)} = \bar{E}_i(\bar{\varepsilon}_{ij}, \bar{D}_i) \\ &f\varepsilon_{ij} = -\frac{\partial\bar{g}}{\partial(\sigma_{ij}/f)} = \bar{\varepsilon}_{ij}(\bar{\sigma}_{ij}, \bar{E}_i) \\ &fD_i = -\frac{\partial\bar{g}}{\partial(E_i/f)} = \bar{D}_{ij}(\bar{\sigma}_{ij}, \bar{E}_i)\end{aligned} \tag{A.9}$$

The first set of equations implies that, without any effect on the derived micro-force quantities, we can take $\psi^\mu = g^\mu$. The next sets of equations imply that the $\bar{\varepsilon}_{ij}(\bar{\sigma}_{ij}, \bar{E}_i)$ and $\bar{D}_{ij}(\bar{\sigma}_{ij}, \bar{E}_i)$ constitutive relationships are the inverse of the $\bar{\sigma}_{ij}(\bar{\varepsilon}_{ij}, \bar{D}_i)$ and $\bar{E}_i(\bar{\varepsilon}_{ij}, \bar{D}_i)$ form. For a general nonlinear constitutive relationship, such an inverse may not be possible to obtain. However, for linear piezoelectric materials the inversion is well-known. Hence, the Helmholtz and Gibbs free energies for a material with conducting cracks are written as,

$$\begin{aligned}\bar{\psi} &= \tfrac{1}{2}f^2 c^D_{ijkl}\varepsilon_{ij}\varepsilon_{kl} - f^2 h_{kij}D_k\varepsilon_{ij} + \tfrac{1}{2}f^2\beta^\varepsilon_{ij}D_iD_j \\ \bar{g} &= -\tfrac{1}{2}s^E_{ijkl}\sigma_{ij}\sigma_{kl}/f^2 - d_{kij}E_k\sigma_{ij}/f^2 - \tfrac{1}{2}\kappa^\sigma_{ij}E_iE_j/f^2\end{aligned} \tag{A.10}$$

The electrical enthalpy, is then just a partial Legendre transformation on the electrical terms, and a partial inversion of the constitutive relationships, and is written as,

$$\begin{aligned} \bar{h} &= \bar{h}(f\varepsilon_{ij}, E_i/f) \\ &= \tfrac{1}{2} f^2 c^E_{ijkl} \varepsilon_{ij} \varepsilon_{kl} - e_{kij} E_k \varepsilon_{ij} - \tfrac{1}{2} \kappa^{\varepsilon}_{ij} E_i E_j / f^2 \end{aligned} \tag{A.11}$$

Note that the relationships between the various forms of the elastic, piezoelectric, and dielectric coefficients are well-known, and once one set has been determined the others can be computed via simple linear algebraic manipulations.

Appendix B

Comparison of the Implementation of Electro-mechanical Boundary Conditions with Other Purposed Methods

Here we compare our approach for the construction of the phase-field electrical enthalpy for permeable crack face boundary conditions to another appearing in the literature. To greatly simplify the demonstration we resort to a simple one-dimensional model with homogeneous fields. For this case, the electrical enthalpy, h, of a linear piezoelectric material is given as,

$$h = \tfrac{1}{2}c^E\varepsilon^2 - e\varepsilon E - \tfrac{1}{2}\kappa^\varepsilon E^2 \tag{B.1}$$

Here c^E is the elastic stiffness at constant electric field, E, e is the piezoelectric coefficient, and κ^ε is the dielectric permittivity at constant strain, ε. For the construction of the phase-field free energy we will use the degradation function $f(\mu) = \mu$, which leads to the phase-field free energy,

$$h = \tfrac{1}{2}\mu^2 c^E\varepsilon^2 - \mu e\varepsilon E - \tfrac{1}{2}\kappa^\varepsilon E^2 + \frac{G_c}{4l_0}(\mu - 1)^2 \tag{B.2}$$

This is in contrast to that used by Abdollahi and Arias [41] (AA) who proposed to degrade all energy terms including strain in with the same functional form,

$$h^{AA} = \tfrac{1}{2}\mu^2 c^E\varepsilon^2 - \mu^2 e\varepsilon E - \tfrac{1}{2}\kappa^\varepsilon E^2 + \frac{G_c}{4l_0}(\mu - 1)^2 \tag{B.3}$$

The solutions to the phase-field order parameter for each of these cases is,

$$\begin{aligned} &\frac{\partial h}{\partial \mu} = \mu c^E \varepsilon^2 - e\varepsilon E + \frac{G_c}{2l_0}(\mu - 1) = 0 \\ &\rightarrow \mu = \frac{G_c/2l_0 + e\varepsilon E}{G_c/2l_0 + c^E \varepsilon^2} \end{aligned} \tag{B.4}$$

and

$$\begin{aligned} &\frac{\partial h^{AA}}{\partial \mu} = \mu c^E \varepsilon^2 - \mu e\varepsilon E + \frac{G_c}{2l_0}(\mu - 1) = 0 \\ &\rightarrow \mu^{AA} = \frac{G_c/2l_0}{G_c/2l_0 + c^E \varepsilon^2 - e\varepsilon E} \end{aligned} \tag{B.5}$$

Within the regions identified as cracks the strain becomes singular and the limiting forms for the order parameters become,

$$\mu \approx \frac{eE}{c^E \varepsilon} \quad \text{and} \quad \mu^{AA} \approx \frac{1}{c^E \varepsilon^2} \quad \text{for large } \varepsilon \tag{B.6}$$

These results can now be applied within the stress and electric displacement relationships as,

$$\left.\begin{aligned} \sigma &= \frac{\partial h}{\partial \varepsilon} = \mu^2 c^E \varepsilon - \mu e E = 0 \\ D &= -\frac{\partial h}{\partial \varepsilon} = \mu e \varepsilon + \kappa^\varepsilon E = \left(\kappa^\varepsilon + \frac{e^2}{c^E}\right) E \end{aligned}\right\} \text{ as } \varepsilon \rightarrow \infty \tag{B.7}$$

Notice that the electric displacement is now related to the electric field by the dielectric permittivity at constant stress σ, $\kappa^\sigma = \kappa^\varepsilon + e^2/c^E$, which is exactly the behavior that should be recovered near a permeable crack. In contrast, the stress and electric displacement from the enthalpy form used by AA are,

$$\left.\begin{aligned} \sigma &= \frac{\partial h}{\partial \varepsilon} = \mu^2 c^E \varepsilon - \mu^2 e E = 0 \\ D &= -\frac{\partial h}{\partial \varepsilon} = \mu^2 e \varepsilon + \kappa^\varepsilon E = \kappa^\varepsilon E \end{aligned}\right\} \text{ as } \varepsilon \rightarrow \infty \tag{B.8}$$

which does not recover the desired behavior near permeable cracks. This may be viewed as a small correction, but the question persists for nonlinear material models. The approach described herein offers a concrete procedure for transforming any electromechanical energy functional into one suitable for applications within the phase-field fracture framework.

Appendix C

Alternative Derivation of the Equivalent Flux Viscosity Scaling

Here we described an alternative form of the derivation for scaling the viscosity inside a phase-field crack. This derivation is more general than that presented in Chapter 4 and will be shown to recover the result (4.69). We will restrict our analysis to one-dimension and will define the y direction as the direction normal to the crack surface such that,

$$u_y = f(y), \quad w_x = g(y), \quad u_x = u_z = w_y = w_z = 0 \tag{C.1}$$

Let u_y^h be the discretization of the crack opening displacement such that $u_y^h(-h/2) = -\Delta u_n/2$ and $u_y^h(h/2) = \Delta u_n/2$ which means that all the crack opening displacement occurs over $-h/2 \leq y \leq h/2$. The material stretch can then be written as,

$$\lambda_y = \lambda_n = 1 + \frac{\partial u_y^h}{\partial y} \quad , \tag{C.2}$$

and clearly satisfies,

$$\int_{-h/2}^{h/2} (\lambda_n - 1)\, dy = \Delta u_n \quad . \tag{C.3}$$

The derivation will take advantage of a few idealizations. First, the phase-field μ is taken to be zero everywhere within the crack (i.e. $-h/2 \leq$

$y \leq h/2$). Thus, only terms governing Stoke's flow will appear in the fluid momentum balance equation (4.62) over the domain of interest. Next, the flow w_x^h will be taken to be zero at the crack walls ($w_x^h(\pm h/2) = 0$), effectively simulating a crack in an impermeable surrounding medium. With $w_{k,k}^h = 0$, the simplified one-dimensional form of the fluid momentum balance (4.62) is,

$$0 = \left(\frac{1}{\lambda_n} \nu^f F_\nu(\lambda_n) w_{x,y}^h \right)_{,y} - \lambda_n p_{,x} \quad , \tag{C.4}$$

where $F_\nu(\lambda_n)$ is the yet unknown viscosity scaling function. We need only to solve this equation in the weak sense, or,

$$\int_{-h/2}^{h/2} \left(\frac{1}{\lambda_n} \nu^f F_\nu(\lambda_n) w_{x,y}^h \delta w_{x,y}^h + \lambda_n p_{,x} \delta w_x^h \right) dy \quad , \tag{C.5}$$

where we have applied the divergence theorem and used the fact that $\delta w_x^h(\pm h/2) = 0$. Also, the total flux in the crack is,

$$\int_{-h/2}^{h/2} \lambda_n w_x^h dy = q \quad . \tag{C.6}$$

The goal of the scaling is to reproduce the lubrication theory result, i.e.,

$$q = \frac{-p_{,x} (\Delta u_n)^3}{12 \nu^f} \quad . \tag{C.7}$$

We now make the assumption that the individual forms of the fluid flow and stretch are known a priori,

$$w_x^h = w_0 N_w(y) \quad \text{and} \quad \lambda_n = 1 + \varepsilon_0 N_\lambda(y) \quad . \tag{C.8}$$

From (C.3),

$$\varepsilon_0 = \frac{\Delta u_n}{\int_{-h/2}^{h/2} N_\varepsilon(y) dy} \quad , \tag{C.9}$$

and from (C.6) and (C.7),

$$w_0 = \frac{-p_{,x}(\Delta u_n)^3}{12\nu^f \left[\int_{-h/2}^{h/2} N_w(y)dy + \Delta u_n \frac{\int_{-h/2}^{h/2} N_\varepsilon(y) N_w(y) dy}{\int_{-h/2}^{h/2} N_\varepsilon(y) dy}\right]} \tag{C.10}$$

Combining with (C.5) gives,

$$\begin{aligned} &\frac{(\Delta u_n)^3}{12} \int_{-h/2}^{h/2} \left[\frac{F_\nu(\lambda_n)}{1 + \frac{\Delta u_n N_\varepsilon(y)}{\int_{-h/2}^{h/2} N_\varepsilon(y')dy'}} \left(\frac{dN_w}{dy}\right)^2 \right] dy \\ &\qquad = \left(\int_{-h/2}^{h/2} N_w(y)dy + \Delta u_n \frac{\int_{-h/2}^{h/2} N_\varepsilon(y) N_w(y) dy}{\int_{-h/2}^{h/2} N_\varepsilon(y) dy} \right)^2 \end{aligned} \tag{C.11}$$

Hence, the scaling function F_ν should be chosen such that (C.11) is satisfied. Unfortunately, to date no general solution strategy had been developed for (C.11). The equation is significantly reduced when the stretch is chosen to be constant, or $N_\varepsilon(y) = 1$,

$$F_\nu(\lambda_n) = 12 \left(\frac{1 + \Delta u_n/h}{\Delta u_n} \right)^3 \frac{\left(\int_{-h/2}^{h/2} N_w(y)dy \right)^2}{\int_{-h/2}^{h/2} \left(\frac{dN_w}{dy}\right)^2 dy} \quad . \tag{C.12}$$

Now, if a quadratic polynomial is chosen for fluid flow as in Chapter 4,

$$N_w(y) = \left(1 - \left(\frac{2y}{h} \right)^2 \right) \quad , \tag{C.13}$$

then the scaling function is,

$$F_\nu(\lambda_n) = \left(\frac{1 + \Delta u_n/h}{\Delta u_n/h} \right)^3 = \left(\frac{\lambda_n}{\lambda_n - 1} \right)^3 \tag{C.14}$$

which is the same result as derived in Chapter 4.

Appendix D

Dimensionless Form of the Model Equations

First we define the following dimensionless strain scaling parameter,

$$\varepsilon_0 \equiv \sqrt{\frac{G_c}{E\ell_0}} \quad , \tag{D.1}$$

and define a dimensionless coordinate system such that,

$$\bar{x}_i \equiv \frac{x_i}{\ell_0} \quad , \quad \bar{u}_i \equiv \frac{u_i}{\varepsilon_0 \ell_0} \quad . \tag{D.2}$$

The normalized small strain tensor is,

$$\bar{\varepsilon}_{ij} = \frac{1}{2}\left(\frac{\partial \bar{u}_i}{\partial \bar{x}_j} + \frac{\partial \bar{u}_j}{\partial \bar{x}_i}\right) = \frac{\varepsilon_{ij}}{\varepsilon_0} \tag{D.3}$$

The Hemhotlz free energy (2.23) can be normalized as,

$$\bar{\psi} \equiv \frac{\psi}{E\varepsilon_0^2} = \frac{1}{2} f_d(\mu) \frac{c_{ijkl}}{E} \left(\frac{\varepsilon_{ij}}{\varepsilon_0}\right)\left(\frac{\varepsilon_{kl}}{\varepsilon_0}\right) + \frac{1}{4}(1-\mu)^2 + (\ell_0 \mu_{,i})(\ell_0 \mu_{,i}) \quad , \tag{D.4}$$

where E is some characteristic material modulus. For the isotropic case E is Young's modulus. We now define the following stiffness tensor,

$$\bar{c}_{ijkl} \equiv \frac{c_{ijkl}}{E} \quad , \tag{D.5}$$

and rewrite the normalized Hemholtz free energy as,

$$\bar{\psi} = \frac{1}{2} f_d(\mu) \bar{c}_{ijkl} \bar{\varepsilon}_{ij} \bar{\varepsilon}_{kl} + \frac{1}{4}(1-\mu)^2 + \frac{\partial \mu}{\partial \bar{x}_i} \frac{\partial \mu}{\partial \bar{x}_i} \quad . \tag{D.6}$$

New constitutive relationships can be developed in a similar fashion as,

$$\begin{aligned} \frac{\partial \bar{\psi}}{\partial \bar{\varepsilon}_{ij}} &= \frac{\sigma_{ji}}{E\varepsilon_0} \equiv \bar{\sigma}_{ji} \\ \frac{\partial \bar{\psi}}{\partial \left(\frac{\partial \mu}{\partial \bar{x}_i}\right)} &= \frac{\xi_i}{E\varepsilon_0^2 \ell_0} \equiv \bar{\xi}_i \quad . \\ -\frac{\partial \bar{\psi}}{\partial \mu} - \frac{\beta}{E\varepsilon_0^2}\dot{\mu} &= \frac{\pi}{E\varepsilon_0^2} \equiv \bar{\pi} \end{aligned} \tag{D.7}$$

Thus, the normalized weak form statement:

Find $\bar{u}_i \in \mathcal{S}_i^{\bar{u}}$ and $\mu \in \mathcal{S}^{\mu}$ such that for all $\delta\bar{u}_i \in \mathcal{V}_i^{\bar{u}}$ and $\delta\mu \in \mathcal{V}^{\mu}$,

$$\int_V \left(\bar{\sigma}_{ji}\delta\bar{\varepsilon}_{ij} - \bar{\pi}\delta\mu + \bar{\xi}_i \frac{\partial \delta\mu}{\partial \bar{x}_i} \right) dV = \int_V \left(\bar{b}_i \delta\bar{u}_i + \bar{\gamma}\delta\mu \right) dV + \int_S \bar{t}_i \delta\bar{u}_i dS \quad . \tag{D.8}$$

where,

$$\bar{b}_i \equiv \frac{b_i \ell_0}{E\varepsilon_0} \quad , \quad \bar{t}_i \equiv \frac{t_i \ell_0}{E\varepsilon_0} \quad \text{and} \quad \bar{\gamma} \equiv \frac{\gamma}{E\varepsilon_0^2} \quad . \tag{D.9}$$

A nice advantage of the normalized formulation is that in the absence of body forces and under boundary conditions that are traction free or displacement controlled, only the material parameters ν, ε_0 and ℓ_0 are needed to construct a solution for u_i and μ.

Normalization of the piezoelectric model equations proceeds in basically the same fashion as above. For the poroelasticity model equations, the flow equations require extra consideration. First, we simply extend the above normalizations to the finite deformation theory,

$$F_{iJ} = \frac{\partial x_i}{\partial X_J} = \frac{\partial u_i}{\partial X_J} + \frac{\partial X_i}{\partial X_J} = \varepsilon_0 \frac{\partial \bar{u}_i}{\partial \bar{X}_J} + \frac{\partial \bar{X}_i}{\partial \bar{X}_J} \quad . \tag{D.10}$$

Next we adopt the following normalizations,

$$\bar{p} \equiv \frac{p}{E\varepsilon_0} \quad , \quad \bar{\kappa} \equiv \frac{\kappa}{\ell_0^2} \quad , \quad \bar{\rho}^f = \frac{\rho^f}{\rho_0^f} \quad , \quad \bar{w}_i \equiv \frac{w_i t_0}{\ell_0} \quad \text{and} \quad \bar{\nu}^f \equiv \frac{\nu^f}{t_0 E\varepsilon_0} \quad . \tag{D.11}$$

Here we have introduced a characteristic time scale t_0 and a reference fluid density ρ_0^f. Also, the normalized deviatoric fluid stress is,

$$\bar{\tau}_{ji} \equiv \frac{t_0 \tau_{ji}}{E\varepsilon_0} \quad . \tag{D.12}$$

and normalized external sources are defined as,

$$\bar{m} \equiv \tilde{m}\, t_0 \quad \text{and} \quad \bar{t}_i^f \equiv \frac{\tilde{t}_i^f \ell_0}{E\varepsilon_0} \quad . \tag{D.13}$$

With these definitions in hand, we can now write the normalized weak form of the fluid momentum balance and fluid mass balance by dividing the corresponding terms in (4.66) by $E\varepsilon_0/t_0$. This gives,

$$\begin{aligned} &\int_{V_0} \left[\left(\bar{\tau}_{ji} J F^{-1}_{Jj} - \bar{p} J F^{-1}_{Ji} \right) \frac{\partial \delta \bar{w}_i}{\partial \bar{X}_J} + g_D(\mu) \frac{\bar{\nu}^f}{\bar{\kappa}} J \bar{w}_i \delta \bar{w}_i \right] dV_0 \\ &\int_{V_0} \left[- \left(\frac{1}{\bar{\rho}^f} \left(\phi \dot{\bar{\rho}}^f J \right) + J F^{-1}_{Ji} \frac{\partial \bar{w}_i}{\partial \bar{X}_J} + \frac{1}{\bar{\rho}^f} \frac{\partial \bar{\rho}^f}{\partial \bar{X}_J} J F^{-1}_{Ji} \bar{w}_i \right) \delta \bar{p} \right] dV_0 \quad . \\ &= \int_{V_0} \left(-\bar{m} \delta \bar{p} \right) dV_0 + \int_{S_0} \bar{t}_i^f \delta \bar{w}_i dS_0 \end{aligned} \tag{D.14}$$

Appendix E

Tension/Compression Asymmetry for Biot Theory

Consider the poro-enthalpy (4.50) defined in Chapter 4 meant to recover linear Biot poroelastic theory. Specifically, consider the Biot coefficient cross term, namely,

$$(1-\phi_0)\, J_0 \rho_0^s \Omega^s = \ldots - \left[\alpha + (1-\alpha)\, g_m(\mu)\right](J-1)\, p + \ldots \tag{E.1}$$

Typical materials involved in hydraulic fracturing are deep within the earth's crust and are subject to very large compressive stress states. Due to the phase-field coupling in the above expression, large but geologically realistic compressive strains and pore-pressures act to significantly perturb the phase-field response in the material. We propose a tension/compression asymmetry that is similar in spirit to the tension/compression decomposition of the strain energy,

$$(1-\phi_0)\, J_0 \rho_0^s \Omega^s = \ldots - \alpha\,(J-1)\, p - F_B(\alpha, \phi_0, J, \mu) p + \ldots \quad , \tag{E.2}$$

where,

$$F_B = \begin{cases} (1-\alpha)\,(J-1)\, g_m(\mu) & ; \quad J \geq 1 \\ -C_B \phi_0 \left(1 - e^{(1-\alpha)(J-1) g_m(\mu)/(C_B \phi_0)}\right) & ; \quad J < 0 \end{cases} \tag{E.3}$$

The positive constant C_B should be chosen to be small compared to 1 and controls the sharpness of the transition between tensile response and compressive response. A smaller C_B corresponds to a sharper transition. The corresponding terms in the stress, porosity, and micro-force in (4.56) and (4.57) are unchanged when $J \geq 1$. However, for $J < 1$ they take the form,

$$\begin{aligned}
\phi J &= \ldots + \alpha\,(J-1) - C_B\phi_0\left(1 - e^{(1-\alpha)(J-1)g_m(\mu)/(C_B\phi_0)}\right) + \ldots \\
P_{Ji} &= \ldots - \alpha J F_{Ji}^{-1} p - (1-\alpha)\, g_m(\mu) e^{(1-\alpha)(J-1)g_m(\mu)/(C_B\phi_0)} J F_{Ji}^{-1} p + \ldots \\
\tilde{\pi} &= \ldots + g_m{}'(\mu)\,(1-\alpha)\,(J-1)\, e^{(1-\alpha)(J-1)g_m(\mu)/(C_B\phi_0)} p + \ldots
\end{aligned} \tag{E.4}$$

Furthermore, the term involving the Biot tangent modulus can be linearized about a reference pressure such that,

$$(1-\phi_0)\, J_0 \rho_0^s \Omega^s = \ldots - [1 - g_m(\mu)]\,\frac{p^2}{2N} + \ldots \quad \rightarrow \quad \left\{ - [1 - g_m(\mu)]\,\frac{(p-p_0)^2}{2N} \right\} \tag{E.5}$$

Bibliography

[1] N. Provotas, N. Goldenfeld, and J. Dantzig. Efficient computation of dendritic microstructures using adaptive mesh refinement. *Phys. Rev. Lett.*, 80:3308–3311, 1998.

[2] L.Q. Chen. Phase-field models for microstructural evolution. *Annu. Rev. Mater. Res.*, 32:113–140, 2002.

[3] M. Koslowski, A.M. Cuitino, and M. Ortiz. A phase-field theory of dislocation dynamics, strain hardening and hysteresis in ductile single crystals. *J. Mech. Phys. Solids*, 50:2597–2635, 2002.

[4] W. Zhang and K. Bhattacharya. A computational model of ferroelectric domains. part i: Model formulation and domain switching. *Acta Mater.*, 53:185–198, 2005.

[5] Y. Su and C.M. Landis. Continuum thermodynamics of ferroelectric domain evolution: Theory, finite element implementation, and application to domain wall pinning. *J. Mech. Phys. Solids*, 55:280–305, 2007.

[6] G.A. Francfort and J.-J. Marigo. Revisiting brittle fracture as an energy minimization problem. *Journal of the Mechanics and Physics of Solids*, 46(8):1319–1342, 1998.

[7] B. Bourdin, G. A. Francfort, and J-J. Marigo. Numerical experiments in revisited brittle fracture. *Journal of the Mechanics and Physics of Solids*, 48(4):797–826, 2000.

[8] Michael J. Borden, Clemens V. Verhoosel, Michael A. Scott, Thomas J.R. Hughes, and Chad M. Landis. A phase-field description of dynamic brittle fracture. *Computer Methods in Applied Mechanics and Engineering*, 217(0):77–95, 2012.

[9] Z. Suo, C.-M. Kuo, D.M. Barnett, and J.R. Willis. Fracture mechanics for piezoelectric ceramics. *Journal of the Mechanics and Physics of Solids*, 40(4):739–765, 1992.

[10] Horacio A. Sosa and Y.Eugene Pak. Three-dimensional eigenfunction analysis of a crack in a piezoelectric material. *International Journal of Solids and Structures*, 26(1):1–15, 1990.

[11] V.Z. Parton. A fracture mechanics of piezoelectric materials. *Acta Astronautica*, 3:671–683, 1976.

[12] G.P. Cherepanov. *Mechanics of Brittle Fracture*. McGraw-Hill, New York, 1979.

[13] W.F.J. Deeg. *The Analysis of Dislocation, Crack, and Inclusion Problems in Piezoelectric Solids*. PhD thesis, Stanford University, 1980.

[14] A.A. Griffith. The phenomena of rupture and flow in solids. *Philos. Trans. R. Soc. London Ser.*, A(221):163–198, 1921.

[15] Susmit Kumar and Raj N. Singh. Crack propagation in piezoelectric materials under combined mechanical and electrical loadings. *Acta Materialia*, 44(1):173–200, 1996.

[16] S. Kumar and R.N. Singh. Energy release rate and crack propagation in piezoelectric materials. Part I: Mechanical/electrical load. *Acta Materialia*, 45(2):849–857, 1997.

[17] S. Kumar and R.N. Singh. Energy release rate and crack propagation in piezoelectric materials. Part II: Combined mechanical and electrical loads. *Acta Materialia*, 45(2):859–868, 1997.

[18] Robert M McMeeking. Towards a fracture mechanics for brittle piezoelectric and dielectric materials. *International Journal of Fracture*, 108(1):25–41, 3 2001.

[19] Y.E. Pak. Linear electro–elastic fracture mechanics of piezoelectric materials. *International Journal of Fracture*, 54:79–100, 1992.

[20] S.B. Park and C.T. Sun. Effect of electric field on fracture of piezoelectric ceramics. *International Journal of Fracture*, 70:203–216, 1995.

[21] Y. Shindo, H. Murakami, K. Horiguchi, and F. Narita. Evaluation of electric fracture properties of piezoelectric ceramics using the finite element and single-edge precracked-beam methods. *J. Am. Ceram. Soc.*, 85:1243–1248, 2002.

[22] J. Wang and M. Kamlah. Crack propagation in piezoelectric ceramics: Effects of applied electric fields. *J. Appl. Phys.*, 81:7471–7479, 1997.

[23] T.Y. Zhang and C.F. Gao. Fracture behaviors of piezoelectric materials. *Theoretical and Applied Fracture Mechanics*, 41(1–3):339–379, 2004. Mesofracture Mechanics: Current Approaches to Material Damage at Different Size and Time Scales.

[24] Tong-Yi Zhang, Cai-Fu Qian, and Pin Tong. Linear electro-elastic analysis of a cavity or a crack in a piezoelectric material. *International Journal of Solids and Structures*, 35(17):2121–2149, 1998.

[25] T.H. Hao and Z.Y. Shen. A new electric boundary condition of electric fracture mechanics and its applications. *Engineering Fracture Mechanics*, 47:793–802, 1994.

[26] Robert M. McMeeking. The energy release rate for a griffith crack in a piezoelectric material. *Engineering Fracture Mechanics*, 71(7–8):1149–1163, 2004.

[27] Robert M. McMeeking. Crack tip energy release rate for a piezoelectric compact tension specimen. *Engineering Fracture Mechanics*, 64(2):217–244, 9 1999.

[28] Chad M. Landis. Energetically consistent boundary conditions for electromechanical fracture. *International Journal of Solids and Structures*, 41(22-23):6291–6315, 2004.

[29] Wenyuan Li, Robert M. McMeeking, and Chad M. Landis. On the crack face boundary conditions in electromechanical fracture and an experimental protocol for determining energy release rates. *European Journal of Mechanics - A/Solids*, 27(3):285–301, 2008.

[30] Martin L. Dunn. The effects of crack face boundary conditions on the fracture mechanics of piezoelectric solids. *Engineering Fracture Mechanics*, 48(1):25–39, 1994.

[31] Huajian Gao, Tong-Yi Zhang, and Pin Tong. Local and global energy release rates for an electrically yielded crack in a piezoelectric ceramic. *Journal of the Mechanics and Physics of Solids*, 45(4):491–510, 1997.

[32] V. Heyer, G.A. Schneider, H. Balke, J. Drescher, and H.-A. Bahr. A fracture criterion for conducting cracks in homogeneously poled piezoelectric PZT-PIC 151 ceramics. *Acta Materialia*, 46(18):6615–6622, 1998.

[33] G.A. Schneider, F. Felten, and R.M. McMeeking. The electrical potential difference across cracks in pzt measured by kelvin probe microscopy and the implications for fracture. *Acta Materialia*, 51(8):2235–2241, 2003.

[34] W.S. Kreher. Influence of domain switching zones on the fracture toughness of ferroelectrics. *Journal of the Mechanics and Physics of Solids*, 50:1029–1050, 2002.

[35] Meinhard Kuna. Fracture mechanics of piezoelectric materials – where are we right now? *Engineering Fracture Mechanics*, 77(2):309–326, 2010.

[36] D. Carka and C. M. Landis. The analysis of crack tip fields in ferroelastic materials. *Smart Materials and Structures*, 20(9):094005, 2011.

[37] J. Sheng and C. M. Landis. Toughening due to domain switching in single crystal ferroelastic materials. *International Journal of Fracture*, 143:161–175, 2007.

[38] I. Arias, S. Serebrinsky, and M. Ortiz. A phenomenological cohesive model of ferroelectric fatigue. *Acta Materialia*, 54:975–984, 2006.

[39] C.V. Verhoosel, M.A. Scott, R. de Borst, and T.J.R. Hughes. An isogeometric approach to cohesive zone modeling. *Int. J. Numer. Meth. Engng*, 87:336–360, Jul 2011.

[40] C. Linder, D. Rosato, and C. Miehe. New finite elements with embedded strong discontinuities for the modeling of failure in electromechanical coupled solids. *Computer Methods in Applied Mechanics and Engineering*, 200(1–4):141–161, 2011.

[41] Amir Abdollahi and Irene Arias. Phase-field modeling of crack propagation in piezoelectric and ferroelectric materials with different electromechanical crack conditions. *Journal of the Mechanics and Physics of Solids*, 60(12):2100–2126, 2012.

[42] C. Miehe, F. Welschinger, and M. Hofacker. A phase field model of electromechanical fracture. *Journal of the Mechanics and Physics of Solids*, 58(10):1716–1740, 2010.

[43] B.X. Xu, D. Schrade, D. Gross, and R. Müller. Fracture simulation of ferroelectrics based on the phase field continuum and a damage variable. *International Journal of Fracture*, 166:163–172, 2010.

[44] F. G. Bell. *Engineering geology and construction.* CRC Press, New York, 2004.

[45] L. Aamodt and M. Kuriyagawa. Measurement of instantaneous shut-in pressure in crystalline rock. In *Presented at the Workshop on Hydraulic Fracturing Stress Meas.*, volume 1 of *1-5*, Monterey, Calif., December 1981.

[46] D. Banks, N. E. Odling, H. Skarphagen, and E. Rohr-Torp. Permeability and stress in crystalline rocks. *Terra Nova*, 8:223–235, 1996.

[47] C. Less and N. Andersen. Hydrofracture: state of the art in south africa. *Applied Hydrogeology*, 2:59–63, 1994.

[48] A. Ghassemi. A review of some rock mechanics issues in geothermal reservoir development. *Geotechnology and Geological Engineering*, 30:647–664, 2012.

[49] R. Bertani. Geothermal power generation in the world 2005–2010 update report. *Geothermics*, 41:1–19, 2012.

[50] B. Matek. 2015 annual u.s. & global geothermal power production report. Technical Report 1-21, Geothermal Energy Association, 2015.

[51] T. K. Perkins and L. R. Kern. Widths of hydraulic fractures. *Journal of Petroleum Technology*, 13(09):937–949, 1961.

[52] R. P. Nordgren. Propagation of a vertical hydraulic fracture. *Society of Petroleum Engineers Journal*, 12:306–314, 1972.

[53] J. Geertsma and F. De Klerk. A rapid method of predicting width and extent of hydraulically induced fractures. *Journal of Petroleum Technology*, 21(12):1571–1581, 1969.

[54] A. A. Daneshy. On the design of vertical hydraulic fractures. *Journal of Petroleum Technology*, 25:83–97, 1973.

[55] A. Settari and M.P. Cleary. Development and testing of a pseudo-three-dimensional model of hydraulic fracture geometry. *Society of Petroleum Engineers*, 1, 1986.

[56] J. Adachi, E. Siebrits, A. Peirce, and J. Desroches. Computer simulation of hydraulic fractures. *International Journal of Rock Mechanics & Mining Sciences*, 44:739–757, 2007.

[57] E. Detournay. Propagation regimes of fluid-driven fractures in impermeable rocks. *International Journal of Geomechanics*, 4:35–45, 2004.

[58] E. Detournay and A. Peirce. On the moving boundary conditions for a hydraulic fracture. *International Journal of Engineering Science*, 84:147–155, 2014.

[59] J. Desroches, E. Detournay, B. Lenoach, P. Papanastasiou, J. Pearson, M. Thiercelin, and A. Cheng. The crack tip region in hydraulic fracturing. *Proceedings of the Royal Society of London. Series A: Mathematical and Physical Sciences*, 447:39–48, 1994.

[60] C. Cipolla, X. Weng, M. Mack, U. Ganguly, H. Gu, O. Kresse, and C. Cohen. Integrating microseismic mapping and complex fracture modeling to characterize fracture complexity. In *SPE/EAGE European Unconventional Resources Conference & Exhibition-From Potential to Production*, 2012.

[61] M. J. Mayerhofer, E. Lolon, N. R. Warpinski, C. L. Cipolla, D. W. Walser, and C. M. Rightmire. What is stimulated reservoir volume? *SPE Production & Operations*, 25:89–98, 2010.

[62] N. P. Roussel and M. M. Sharma. Optimizing fracture spacing and sequencing in horizontal-well fracturing. *SPE Journal*, 16:575–581, 2011.

[63] J. E. Olson and K. Wu. Sequential vs. simultaneous multizone fracturing in horizontal wells: Insights from a non-planar multifrac numerical model. In *SPE Hydraulic Fracturing Technology Conference*. Society of Petroleum Engineers, 2012.

[64] X. Zhang, R.G. Jeffrey, and M. Thiercelin. Escape of fluid-driven fractures from frictional bedding interfaces: A numerical study. *Journal of Structural Geology*, 30:478–490, 2008.

[65] X. Zhang and R.G. Jeffrey. Reinitiation or termination of fluid-driven fractures at frictional bedding interfaces. *Journal of Geophysical Research*, 113:B08416, 2008.

[66] X. Zhang, R.G. Jeffrey, and M. Thiercelin. Deflection and propagation of fluid-driven fractures at frictional bedding interfaces: A numerical investigation. *Journal of Structural Geology*, 29:396–410, 2007.

[67] P. Fu, S.M. Johnson, and C.R. Carrigan. An explicitly coupled hydro-geomechanical model for simulating hydraulic fracturing in arbitrary discrete fracture networks. *International Journal for Numerical and Analytical Methods in Geomechanics*, 37:2278–2300, 2013.

[68] N.R. Warpinski, M.J. Mayerhofer, Vincent, M.C., C.L. Cipolla, and E.P. Lolon. Stimulating unconventional reservoirs: Maximizing network growth while optimizing fracture conductivity. *Journal of Canadian Petroleum Technology*, 48:39–51, 2009.

[69] B.R. Meyer and L.W. Bazan. A discrete fracture network model for hydraulically induced fractures: Theory, parametric and case studies. In *SPE Hydraulic Fracturing Technology Conference and Exhibition*. Society of Petroleum Engineers, 2011.

[70] X. Weng, O. Kresse, C.-E. Cohen, R. Wu, and H. Gu. Modeling of hydraulic-fracture-network propagation in a naturally fractured formation. *SPE Production & Operations*, 26:368–380, 2011.

[71] J. Rungamornrat, M. F. Wheeler, and M. E. Mear. Coupling of fracture/non-newtonian flow for simulating nonplanar evolution of hydraulic fractures. In *SPE Annual Technical Conference and Exhibition*. Society of Petroleum Engineers, 2005.

[72] A. Dahi-Taleghani and J. E. Olson. Numerical modeling of multistranded-hydraulic-fracture propagation: Accounting for the interaction between induced and natural fractures. *SPE Production & Operations*, 26:173–184, 2011.

[73] H. Gu, X. Weng, J. B. Lund, M. G. Mack, U. Ganguly, and R. Suarez-Rivera. Hydraulic fracture crossing natural fracture at non-orthogonal angles a criterion its validation and applications. In *SPE Hydraulic Fracturing Technology Conference*. Society of Petroleum Engineers, 2011.

[74] A.R. Khoei and E. Haghighat. Extended finite element modeling of deformable porous media with arbitrary interfaces. *Appl. Math. Model.*, 35:5426–5441, 2001.

[75] A.R. Khoei, M. Vahab, and E. Haghighat. A mesh-independent finite element formulation for modeling crack growth in saturated porous media based on an enriched-fem technique. *Int. J. Fract.*, 188:79–108, 2014.

[76] R. Rangarajan and A. Lew. Universal meshes: A method for triangulating planar curved domains immersed in nonconforming meshes. *Int. J. Numer. Meth. Engng*, 98:236–264, 2014.

[77] R. Rangarajan, M.M. Chiaramonte, M.J. Hunsweck, Y. Shen, and A. Lew. Simulating curvilinear crack propagation in two dimentsions with universal meshes. *Int. J. Numer. Meth. Engng*, 102:632–670, 2014.

[78] J.P. Pereira, C.A. Duarte, and X. Jiao. Three-dimensional crack growth with hp-generalized finite element and face offsetting methods. *Computational Mechanics*, 46:431–453, 2010.

[79] Y.D. Ha and F. Bobaru. Studies of dynamic crack propagation and crack branching with peridynamics. *International Journal of Fracture*, 162:229–244, 2010.

[80] H. Ouchi, A. Katiyar, J. York, J.T. Foster, and M.M. Sharma. A fully coupled porous flow and geomechanics model for fluid driven cracks: a peridynamics approach. *Computational Mechanics*, 55:561–576, 2015.

[81] E. Lorentz, S. Cuvilliez, and K. Kazymyrenko. Modelling large crack propagation: from gradient damage to cohesive zone models. *International Journal of Fracture*, 178:85–95, 2012.

[82] A. Shojaei, A.D. Taleghani, and Guoqiang Li. A continuum damage failure model for hydraulic fracturing of porous rocks. *International Journal of Plasticity*, 59:199–212, 2014.

[83] H. Amor, J.J. Marigo, and C. Maurini. Regularized formulation of the variational brittle fracture with unilateral contact: numerical experiments. *J. Mech. Phys. Solids*, 57:1209–1229, 2009.

[84] B. Bourdin. Numerical implementation of the variational formulation for quasi-static brittle fracture. *Interfaces Free Bound.*, 9:411–430, 2007.

[85] B. Bourdin, G.A. Francfort, and J-J. Marigo. The variational approach to fracture. *J. Elast*, 91:5–148, 2008.

[86] B. Bourdin, C. Larsen, and C. Richardson. A time-discrete model for dynamic fracture based on crack regularization. *Int. J. Fract.*, 168:133–143, 2011.

[87] G. Del Piero, G. Lancioni, and R. March. A variational model for fracture mechanics: numerical experiments. *J. Mech. Phys. Solids*, 55:2513–2537, 2007.

[88] M. Hofacker and C. Miehe. A phase field model of dynamic fracture: robust field updates for the analysis of complex crack patterns. *Int. J. Numer. Methods Eng.*, 93:276–301, 2013.

[89] C. Miehe, F. Welschinger, and M. Hofacker. Thermodynamically consistent phase-field models of fracture: variational principles and multi-field fe implementations. *Int. J. Numer. Methods Eng.*, 83:1273–1311, 2010.

[90] M.J. Borden, T.J.R. Hughes, C.M. Landis, and Verhoosel C.V. A higher-order phase-field model for brittle fracture: formulation and analysis within the isogeometric analysis framework. *Comput. Methods Appl. Mech. Engrg.*, 273:100–118, 2014.

[91] A. Karma, D.A. Kessler, and H. Levine. Phase-field model of mode iii dynamic fracture. *Phys. Rev. Lett.*, 87:045501, 2001.

[92] H. Henry and H. Levine. Dynamic instabilities of fracture under biaxial strain using a phase field model. *Phys. Rev. Lett.*, 93:105504, 2004.

[93] B. Bourdin, C. Chukwudozie, and K. Yoshioka. A variational approach to the numerical simulation of hydraulic fracturing. In *SPE Annual Technical Conference and Exhibitio*. Society of Petroleum Engineers, 2012.

[94] C. Miehe, S. Mauthe, and S. Teichtmeister. Minimization principles for the coupled problem of darcy-biot-type fluid transport in porous media linked to phase field modeling of fracture. *J. Mech. Phys. Solids*, 82:186–217, 2015.

[95] A. Mikelic, M.F. Wheeler, and T. Wick. A phase-field method for propagating fluid-filled fractures coupled to a surrounding porous medium. *SIAM: Multiscale Modeling and Simulation*, 13:367–398, 2015.

[96] M.E. Gurtin. Generalized ginzburg–landau and cahn–hilliard equations based on a microforce balance. *Physica*, D(92):178–192, 1996.

[97] L. Ambrosio and V.M. Tortorelli. Approximation of functionals depending on jumps by elliptic functionals via γ-convergence. *Comm. Pure Appl. Math.*, 43(8):999–1036, 1990.

[98] L. Ambrosio and V.M. Tortorelli. On the approximation of free discontinuity problems. *Boll. Un. Mat. Ital. B (7)*, 6(1):105–123, 1992.

[99] M.J. Borden. *Isogeometric Analysis of Phase-Field Models for Dynamic Brittle and Ductile Fracture*. PhD thesis, The University of Texas at Austin, August 2012.

[100] A. Chambolle. An approximation result for special functions with bounded variations. *J. Math Pures Appl.*, 83:929–954, 2004.

[101] E. Fried and M.E. Gurtin. Continuum theory of thermally induced phase transitions based on an order parameter. *Physica D*, 68:326–343, 1993.

[102] E. Fried and M.E. Gurtin. Dynamic solid-solid transitions with phase characterized by an order parameter. *Physica D*, 72:287–308, 1994.

[103] B.D. Coleman and W. Noll. The thermodynamics of elastic materials with heat conduction and viscosity. *Arch. Rat. Mech. Anal.*, 13:245–261, 1963.

[104] G. Irwin. Analysis of stresses and strains near the end of a crack traversing a plate. *Journal of Applied Mechanics*, 24:361–364, 1957.

[105] G.I. Barenblatt. The mathematical theory of equilibrium cracks in brittle fracture. *Advances in Applied Mechanics*, 7:55–129, 1962.

[106] D.S. Dugdale. Yielding of steel sheets containing slits. *Journal of the Mechanics and Physics of Solids*, 8(2):100–104, 1960.

[107] Michael J. Borden, Thomas J.R. Hughes, Chad M. Landis, and Clemens V. Verhoosel. A higher-order phase-field model for brittle

fracture: Formulation and analysis within the isogeometric analysis framework. *Computer Methods in Applied Mechanics and Engineering*, 273:100–118, 2014.

[108] Clemens V. Verhoosel and René de Borst. A phase-field model for cohesive fracture. *International Journal for Numerical Methods in Engineering*, 96(1):43–62, 2013.

[109] C. M. Landis. A new finite-element formulation for electromechanical boundary value problems. *Int. J. Numer. Meth. Engng*, 55:613–628, 2002.

[110] A.S. Semenova, H. Kessler, A.C. Liskowsky, and H. Balke. On a vector potential formulation for 3d electromechanical finite element analysis. *Comm. Numer. Methods Eng.*, 22:357–375, 2006.

[111] Seungbae Park and Chin Teh Sun. Fracture criteria for piezoelectric ceramics. *Journal of the American Ceramic Society*, 78(6):1475–1480, 1995.

[112] O. Coussy. *Poromechanics*. John Wiley & Sons, Chichester, 1994.

[113] O. Coussy. *Mechanics of Porous Continua*. John Wiley & Sons, Chichester, 1995.

[114] O. Coussy. *The Mechanics and Physics of Porous Solids*. John Wiley & Sons, Chichester, 2010.

[115] O. Coussy. Thermodynamics of saturated porous solids in finite deformation. *European Journal of Mechanics and Solids*, 8:1–14, 1989.

[116] O. Coussy. A general theory of thermoporoelastoplasticity for saturated materials. *Transport in Porous Media*, 4:281–293, 1989.

[117] Zachary A. Wilson, Michael J. Borden, and Chad M. Landis. A phase-field model for fracture in piezoelectric ceramics. *International Journal of Fracture*, 183(2):135–153, 2013.

[118] E. Detournay and A.H.-D. Cheng. Fundamentals of poroelasticity. In *Comprehensive Rock Engineering: Principles, Practice and Projects Vol. II, Analysis and Design Method*, pages 113–171. Pergamon Press, 1993.

[119] H. C. Brinkman. A calculation of the viscous force exerted by a flowing fluid on a dense swarm of particles. *Applied Scientific Research*, 1:27–34, 1949.

[120] O. Coussy, E. Detournay, and L. Dormieux. From mixture theories to biot's theory. *International Journal of Solids and Structures*, 35:4619–4635, 1998.

[121] M.A. Biot. The theory of propagation of elastic waves in a fluid saturated porous solid, i. lower frequency range. *Journal of the Acoustical Society of America*, 28:168–178, 1956.

[122] OA. Ladyshenskaya. *The Mathematical Theory of Viscous Incompressible Flow*. Gordon and Breach, New York, 1969.

[123] I. Babuska. The finite element method with lagrangian multipliers. *Numerische Mathematik*, 20(3):179–192, 1973.

[124] F. Brezzi. On the existence, uniqueness and approximation of saddle-point problems arising from lagrangian multipliers. *ESAIM: Mathematical Modeling and Numerical Analysis*, 8(R2):129–151, 1974.

[125] Taylor C. and P. Hood. A numerical solution of the navier-stokes equations using the finite element technique. *Computers & Fluids*, 1:73–100, 1973.

[126] S. Balay, S. Abhyankar, M.F. Adams, J. Brown, P. Brune, K. Buschelman, L. Dalcin, V. Eijkhout, W.D. Gropp, D. Kaushik, M.G. Knepley, L.C. McInnes, K. Rupp, B.F. Smith, S. Zampini, and H. Zhang. *PETSc Users Manual*. Argonne National Laboratory, anl-95/11 – revision 3.6 edition, 2015.

[127] Gropp Balay, S., L.C. McInnes, and B.F. Smith. Efficient management of parallelism in object oriented numerical software libraries. *Modern Software Tools in Scientific Computing*, pages 163–202, 1997.

[128] P.R. Amestoy, I.S. Duff, J.Y. L'Excellent, and J. Koster. A fully asynchronous multifrontal solver using distributed dynamic scheduling. *SIAM Journal on Matrix Analysis and Applications*, 23(1):15–41, 2001.

[129] P.R. Amestoy, A. Guermouche, J.Y. L'Excellent, and S. Pralet. Hybrid

scheduling for the parallel solution of linear systems. *Parallel Computing*, 32(2):136–156, 2006.

[130] D. Givoli. Numerical methods for problems in infinite domains. *Studies in Applied Mechanics*, 33, 1992.

[131] D. Carka, M.E. Mear, and C.M. Landis. The dirichlet-to-neumann map for two-dimensional crack problems. *Computer Methods in Applied Mechanics and Engineering*, 200:1263–1271, 2011.

[132] S.A. Khristianovic and Zheltov Y.P. Formation of vertical fractures by means of highly viscous liquid. In *Proceedings of the fourth world petroleum congress*, pages 579–586, Rome, 1995.

[133] A.P. Bunger, E. Detournay, and D.I. Garagash. Toughness-dominated hydraulic fracture with leak-off. *International Journal of Fracture*, 134:175–190, 2005.

[134] John A. Evans and Thomas J. R. Hughes. Isogeometric divergence-conforming b-splines for the darcy–stokes–brinkman equations. *Mathematical Models and Methods in Applied Sciences*, 23(04):671–741, 2013.

Vita

Zachary Adam Wilson was born in Alexandria, Virginia on 22 December 1987, the son of Edwin B. Wilson II and Elizabeth G. Wilson. He received the Bachelor of Science degree in Engineering Science and Mechanics from Virginia Polytechnic Institute and State University in May of 2010. He applied to the University of Texas at Austin for enrollment in their engineering mechanics program. He was accepted and started graduate studies in August, 2010. After his studies, he will begin work for the PETTT program at Engility Corp in Aberdeen, MD.

Permanent email address: zils25@gmail.com

This dissertation was typeset with LaTeX[†] by the author.

[†]LaTeX is a document preparation system developed by Leslie Lamport as a special version of Donald Knuth's TeX Program.